TECHNISCHE UNIVERSITÄT WIEN
Vienna University of Technology
Technische Universität Wien

Final cooling scheme for muon colliders: A door opener for future discovery machines

Diplomarbeit

Ausgeführt am Atominstitut
der Fakultät für Physik
an der Technischen Universität Wien,
in Zusammenarbeit mit der
Europäischen Organisation für Kernphysik.

Durchgefürt von
Bernd Stechauner

Unter der Anleitung von

Univ.Prof. Dipl.-Phys. Dr.rer.nat. Jochen Schieck, und
Dipl.-Phys. Dr.rer.nat. Daniel Schulte

Mitwirkung: Dr. M.Sc. Elena Fol

Bernd Stechauner
Matrikelnummer: 1426914
Genf, am 1. Dezember 2021

Kurzfassung

Um auf bisher unbekannte Phänomene in der Teilchenphysik zu stoßen, ist es eines der wesentlichsten Aspekte der Hochenergiephysik, Teilchenbeschleuniger mit sehr hohen Energien (TeV) zu optimieren und diese auch neu zu entwickeln, damit neue Entdeckungen gemacht werden können. Für das Erreichen hoher Teilchenenergien und Luminositäten braucht es vorallem neue Beschleuniger, die größer sind, aber zugleich enorme finanzielle Kosten verursachen. Deshalb spielen bei der Planung dieser Anlagen, abseits wissenschaftlicher Notwendigkeit, ökonomische und Energieeffizienz eine sehr tragende Rolle. In Zukunft ist es das Ziel nicht nur Higgs-Bosonen im hohen Ausmaß zu generieren, sondern auch Teilchen zu erzeugen, die uns noch völlig unbekannt sind. Dadurch kann die Masse dieser Teilchen ermittelt werden und gewährt der Menschheit aller Wahrscheinlichkeit nach einen Blick hinter das gegenwärtige Standardmodell der Teilchenphysik und öffnet die Tür für bahnbrechende neue Entdeckungen. Seit dem Bekanntwerden der europäischen Strategie für Teilchenphysik des Jahres 2020 ist es gleichsam zwingend, dass sich Wissenschaftler unter anderem dem Konzept für die Entwicklung eines Myonen-Beschleunigers widmen, mit federführender Beteiligung des CERNs.

Der Vorteil dieses Konzepts ist zum einen, dass Myonen zu den Leptonen zählen und bei der Kollision die gesamte Schwerpunktsenergie für die Erschaffung neuer Teilchen umgesetzt wird, was bei Kollisionen mit Hadronen nicht möglich ist. Das macht den Leptonenbeschleuniger bei hohen Energien zu einer sehr präzisen Entdeckungsmaschine. Zum anderen sind Myonen 200-mal schwerer als Elektronen, woraus folgt, dass Bremsstrahlung und Synchotronstrahlung vernachlässigt werden können, was wiederum bei Elektronenbeschleunigungen nicht möglich ist. Dennoch weist der Myonen-Strahl nach seiner Erzeugung noch eine sehr hohe Emittanz auf, die das Divergieren des Strahls antreibt. Die einzig machbare Möglichkeit, diese Emittanz innerhalb der sehr kurzen Lebenszeit des Myons zu reduzieren bzw. zu kühlen, beruht auf dem Prinzip der Ionisationskühlung. Vergangene Studien haben nicht optimale Emittanzen erzielt. Deswegen zielt diese Arbeit darauf ab, die Emittanz des Strahls stufenweise abzukühlen mittels spezifischer Absorber in sehr hohen Magnetfeldern, bevor er schließlich auf mehrere TeV beschleunigt wird und der Myonen-Beschleuniger als geeignete Entdeckungsmaschine funktioniert.

Abstract

Discovering unknown phenomena in particle physics – one of the most essential aspects of high energy physics, requires optimizing and developing high energy particle accelerators, for new discoveries. To be able to reach high particle energies (TeV) at all, new accelerators are needed that are larger and come with high financial costs. For this reason, it is very relevant to develop energy efficient and economic accelerators while continuing progress in that area. One of the most important goals is not only produce Higgs bosons on a much larger scale than it is possible so far, but also generate completely unknown particles. This will allow us to determine the mass of these particles and is likely to give us a glimpse of the physics beyond the Standard Model and therefore opening new doors for groundbreaking discoveries. Since the publication of the European Strategy for Particle Physics in 2020, it is known that scientists are further working on creating a concept of a new muon accelerator led by CERN.

Advantage of this technology include that muons are leptons and therefore convert the entire center of mass energy to create new particles during collisions, which would not be possible in collisions with hadrons. This makes the lepton accelerator to a precision and discovery machine at high energies. Further, muons are 200 times heavier than electrons. As a result, bremsstrahlung and synchotron radiation may be neglected, which in turn cannot be done with electron accelerations. Nevertheless, the muon beam creates a high emittance after its creation, which drives the divergence of the beam. The only feasible way to reduce or cool this emittance within the very short lifetime of the muon is based on the principle of ionization cooling. Past studies have not achieved optimal final emittance values. Therefore, this work aims at gradually cooling the emittance of the muons beam by means of specific absorbers inside very high magnetic fields before it is finally accelerated to several TeV. As a result, the final cooling system should provide muon beams with the optimal properties required by the muon collider design.

A scientific study for the International Muon Collider Collaboration.

Contents

Chapter 1: Introduction

The idea to accelerate and collide muons was already proposed by G. Budker [1, 2] in the 1960s and later developed by Skrinsky [3]. Despite the muon's short lifetime of 2.2 μs, a muon collider can prove to be a very useful technology for expanding our knowledge of the universe's beginning. Currently, the most powerful exploration machine is the Large Hardron Collider (LHC) located at the European Organization for Nuclear Research (CERN), where particle beams collide at a centre of mass (cm.) energy up to 13 TeV for investigation of rare interaction processes in particle physics.

One big issue is that protons are hadrons, which contain quarks and a multiplicity of gluons. Those are the mediators of the strong force and the interaction particle between the quarks. Gluons, in turn, can briefly transform into quark-anti-quark pairs, known in particle physics as sea quarks of the nuclei. It can be seen that a nucleus consists of numerous complex systems coupled to each other. Therefore the parton distribution function was introduced, that describes the fragmentation of the energy among the quark-gluon system. The proton's energy of 938 MeV is relatively high compared to a single (fictive) quark masses of a few MeV.

For that reason, bounded hadrons seems to be unsuitable for bringing the entire beam energy to collision. Other types of particles can be used, which are able to propagate freely in space. For this purpose, leptons such as electrons seem to be suitable. The most powerful electron-positron accelerator was the Large Electron Positron Collider (LEP) at CERN. Nevertheless, electrons colliding in a circular collider have a significant disadvantage. When they are deflected by accelerator specific beam optics, they lose energy in form of synchrotron radiation described with its dissipation power [4, 5]

$$P(E, r_0) = \frac{e^2 \cdot c}{6\pi\epsilon_0 r_0^2} \left(\frac{E}{m_0 c^2} \right)^4 . \tag{1.1}$$

Equation (1.1) illustrates, that deflection of a relativistic particle leads to an energy loss proportional to m^{-4}, due to emitting photons. The natural constants in equation (1.1) stand for the elementary charge $e = 1.6022 \times 10^{-19}\,\mathrm{C}$, the vacuum permittivity $\epsilon_0 = 8.8542 \times 10^{-12}\,\mathrm{AsV^{-1}m^{-1}}$ and the speed of light in vacuum $c = 2.9979 \times 10^{8}\,\mathrm{ms^{-1}}$.

The cm. energy at LEP was limited to 209 GeV (104.5 GeV per beam direction), which only allowed to thoroughly study the electroweak sector of the Standard Model (SM), in fact the existence of the Higgs particle was not clarified.

Until 2012, there had been an intensive search of the Higgs particle to prove the validity of the SM. LEP predicted that this fundamental particle must be heavier than 115 GeV [6]. Only with the conversion of LEP to LHC and the following operation, the data collection analyzes allowed to measure at the two detectors ATLAS [7] and CMS [8] a particle approximately at 125 GeV, which identified as the spin-0 Higgs boson [9].

Nevertheless, the Higgs sector could not be measured precisely and the question still remains whether there is one or even more Higgs like particles, opening new doors for physics Beyond the Standard Model (BSM). In 2021, research groups working at the LHCb experiment could confirm the violation of lepton universality, which is not compatible with the current SM [10]. In the same year, researchers from the g-2 experiment at Fermilab published data [11] showing that the measured anomalous magnetic moment (g-2) of the muon did not agree with the theoretical expectation and therefore provides the need to further explore and extend the SM.

For discovering BSM an accelerator is needed that generates novel Higgs involved phenomena, which cannot be proven at the present LHC. An alternative instrument would be a lepton collider, which brings instead of the electron the 200 times heavier sister particle (the muon) to collision. As it can be seen in equation (1.1), the synchrotron radiation reduces for muons by a factor of 10^{-9} and can be therefore neglected. Thus, muons could be accelerated to several TeV. The challenges, however, are to catch muons immediately after their production, bundle and accelerate them within their short lifetime.

The production rate can be described as the product of the luminosity $\mathcal{L}$ of a collider ring and the effective cross section σ:

$$\dot{N} = \mathcal{L} \cdot \sigma. \tag{1.2}$$

It is worth delving into equation (1.2) in the next two chapters for gaining a better understanding of short-lived and exotic particle generation created by a $\mu^+\mu^-$-smasher. This chapter will treat the muon collider's $\mathcal{L}$ precisely to provide a better understanding of collider beam parameters. Further, the importance of the emittance reduction by ionization cooling will be underlined, as it is the main topic of this thesis. Prior to the interaction of the ionization cooling concept, it is worth to to provide the mathematical background required of this technique.

1.1 Relativistic kinematics

In accelerator physics, it is common to describe particle motions in space-time. It is worth to define the mathematical tools for describing it by means of Einstein's special relativity [12], which is inevitable needed for this work. A physical quantity is Lorentz invariant, if it does not change its value under a transformation to any relatively moving inertial frame. One of such quantities is the Einstein's relativistic energy-momentum relation

$$E^2 = m_0^2 c^4 + p^2 c^2, \tag{1.3}$$

where the rest mass of the system is expressed by $m_0 c^2$, while p is its relativistic momentum. In special relativity, time, length and masses depend on the speed relatively to a certain laboratory frame. Thus, the momentum p can be defined by

$$p = mv = m_0 \gamma \frac{v}{c} c = m_0 \gamma \beta c \tag{1.4}$$

usually expressed in eV/c units, where β and $\gamma = (1-\beta^2)^{-1/2}$ are the velocity depended Lorentz factors. Energy and momentum can be summarized as

$$E = \gamma m_0 c^2 \qquad p = \beta \gamma m_0 c \tag{1.5}$$

and satisfy equation (1.3). In the special relativity, a system of energy and momentum is not described any more in the three-dimensional space, but in in the four-dimensional Minkowski space, which contains a time component additionally to the three spatial coordinates. The so-called contravariant four-vector for describing the relativistic momentum is defined as

$$p^\mu = \begin{pmatrix} E, & p_\mathrm{x} c, & p_\mathrm{y} c, & p_\mathrm{z} c \end{pmatrix}^\top = \begin{pmatrix} E, & \vec{p} c \end{pmatrix}^\top \tag{1.6}$$

practically also known as the four-momentum of a particle and can be transformed in any initial frame by Lorentz transformation. The Lorentz-invariant product of such a four-vector follows the rule of the Lorentz product and is the multiplication of a covariant and a contravariant four vector

$$\mathbf{a} \cdot \mathbf{b} = a_\mu b^\mu = g_{\mu\nu} a^\nu b^\mu = \begin{pmatrix} a^0 & -\vec{a} \end{pmatrix} \begin{pmatrix} b^0 \\ \vec{b} \end{pmatrix} = a^0 b^0 - \vec{a}\vec{b}, \tag{1.7}$$

where the indices $\mu = 0, 1, 2, 3$ label the space time coordinates and the metric tensor

$$g_{\mu\nu} = \begin{pmatrix} 1 & 0 & 0 & 0 \\ 0 & -1 & 0 & 0 \\ 0 & 0 & -1 & 0 \\ 0 & 0 & 0 & -1 \end{pmatrix}, \tag{1.8}$$

describes the relationship between covariant and contravariant four-vectors. Equipped with the technique of special relativity, it is possible to introduce the flux factor

$$F = 4E_{\mathbf{a}}E_{\mathbf{b}}(v_{\mathbf{a}} + v_{\mathbf{b}}) = 4(E_{\mathbf{a}}p_{\mathbf{b}} + E_{\mathbf{b}}p_{\mathbf{a}}) = 4\sqrt{(\mathbf{p_a}\mathbf{p_b}) - m_{\mathbf{a}}^2 m_{\mathbf{b}}^2} \tag{1.9}$$

where the right side oft this equation was derived by means of (1.5). It can be seen that the argument inside the root contains a Lorentz product and a scalar expression of particle masses, which are both invariant under a specific boost transformation.

1.2 Luminosity

Obtaining an expression for $\mathcal{L}$, it is worthwhile to consider two particle distributions, each confined in bunches, as illustrated in Figure 1.1. Lets assume these two bunches crossing at the collision point s. The particle distributions inside the bunches are described by a Gaussian

$$\rho_{\mathbf{i}}(x, y, s, \pm s_0) = N_{\mathrm{i}}\, \rho_{x,\mathbf{i}}(x)\rho_{y,\mathbf{i}}(y)\rho_{z,\mathbf{i}}(s \pm s_0), \tag{1.10}$$

for all three spatial directions with $N_{\mathbf{i}}$ ($\mathbf{i} = \mathbf{a}, \mathbf{b}$) being the number of particles per bunch.

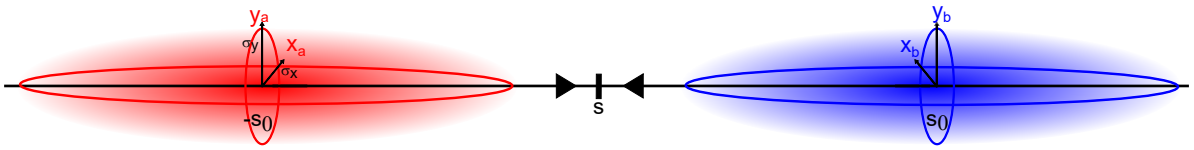

Figure 1.1: Schematic view of a head-on bunch collision, where the particles inside the bunches are distributed by a Gauss function.

Lets further assume, that the Gaussians of both beams are equally, which follows to

$$\begin{aligned}
\rho_{x,\mathbf{a}}(x) &= \rho_{x,\mathbf{b}}(x) = \left(\sqrt{2\pi}\sigma_x\right)^{-1} e^{-\frac{x^2}{2\sigma_x^2}} \\
\rho_{y,\mathbf{a}}(y) &= \rho_{y,\mathbf{b}}(y) = \left(\sqrt{2\pi}\sigma_y\right)^{-1} e^{-\frac{y^2}{2\sigma_y^2}} \\
\rho_{z,\mathbf{a}}(z) &= \rho_{z,\mathbf{b}}(z) = \left(\sqrt{2\pi}\sigma_s\right)^{-1} e^{-\frac{z^2}{2\sigma_s^2}}.
\end{aligned} \tag{1.11}$$

Since the two bunches are moving towards each other, the overlapping integral depends not only on the space components but also on the time component. The following

expression for the bunch luminosity has the form

$$\mathcal{L}_{\text{bunch}} = K \int dt\, d^3x\, \rho_{\mathbf{a}} \rho_{\mathbf{b}}, \tag{1.12}$$

where the kinematic factor K is an expression of the velocity of each bunch and can be derived by equation (1.9) from the previous section:

$$K = v_{\mathbf{a}} + v_{\mathbf{b}} = \frac{F}{E_{\mathbf{a}} E_{\mathbf{b}}} = \sqrt{\left(\frac{p_{\mathbf{a}}}{E_{\mathbf{a}}} - \frac{p_{\mathbf{b}}}{E_{\mathbf{b}}}\right)^2 - \left(\frac{p_{\mathbf{a}}}{E_{\mathbf{a}}}\right)^2 \left(\frac{p_{\mathbf{b}}}{E_{\mathbf{b}}}\right)^2 - \left(\frac{p_{\mathbf{a}} p_{\mathbf{b}}}{E_{\mathbf{a}} E_{\mathbf{b}}}\right)^2}. \tag{1.13}$$

By means of the vectorial identity $\vec{a} \times \vec{b} = \vec{a}^2\vec{b}^2 - (\vec{a}\vec{b})^2$, the kinetic factor becomes $K = \sqrt{(\vec{v_{\mathbf{a}}} - \vec{v_{\mathbf{b}}})^2 - (\vec{v_{\mathbf{a}}} \times \vec{v_{\mathbf{b}}})^2/c^2}$. In the case of head-on collisions and velocities near to c, each bunch speed can be set to $\vec{v}_{\mathbf{a}} = (0,\, 0,\, c)^\top$ and $\vec{v}_{\mathbf{b}} = (0,\, 0,\, -c)^\top$ and the kinetic factor reduces to $K = 2c$. For simplicity, the time element in equation (1.12) can be expressed by $dt = ds_0/c$ and the $\mathcal{L}_{\text{bunch}}$ transforms to

$$\mathcal{L}_{\text{bunch}} = 2\frac{N_{\mathbf{a}} N_{\mathbf{b}}}{\sqrt{2\pi}^6 \sigma_x^2 \sigma_y^2 \sigma_s^2} \int_{-\infty}^{\infty} dx\, e^{-\frac{x^2}{\sigma_x^2}} \int_{-\infty}^{\infty} dy\, e^{-\frac{y^2}{\sigma_y^2}} \int_{-\infty}^{\infty} ds_0\, e^{-\frac{(s-s_0)^2}{2\sigma_s^2}} e^{-\frac{(s+s_0)^2}{2\sigma_s^2}}. \tag{1.14}$$

By applying the integration rule of $\int_{-\infty}^{\infty} dx\, \exp(-\alpha x^2) = \sqrt{\pi/\alpha}$, the bunch luminosity gets its final form of

$$\mathcal{L}_{\text{bunch}} = \frac{N^2}{4\pi\sigma_x\sigma_y}, \tag{1.15}$$

using $N_{\mathbf{a}} = N_{\mathbf{b}} = N$. For a symmetric Gaussian beam its transverse sizes have equal values $\sigma_x = \sigma_y = \sigma_\perp$. Inside the accelerator, the particles will be accelerated nearly to the speed of light ($\beta \approx 1$), the expression (1.15) changes to

$$\mathcal{L}_{\text{bunch}} = \frac{N^2}{4\pi\epsilon_{\perp,\text{N}}\beta^*_\perp}\gamma, \tag{1.16}$$

where the beam size $\sigma_\perp$ is defined as the product of the transverse beta-function $\beta^*_\perp$ (at the collision point) and the normalized transverse emittance $\epsilon_{\perp,\text{N}}$, which properties will be discussed in detail in chapter 3.

If one considers a collider ring with a circumference C and one single collision point in the beam line, the time between two bunch collisions is approximately $t = C/c$. Taking the decay of the muons into account, the integrated bunch luminosity divided by the collision time results to

$$\frac{1}{C/c} \int_0^{\infty} \mathcal{L}_{\text{bunch}}\, dt \propto \int_0^{\infty} N^2\, dt = \int_0^{\infty} N_0^2 e^{-\frac{2t}{\gamma\tau_0}}\, dt, \tag{1.17}$$

where the particle decay is assumed to decrease exponentially. In this case, N_0 describes the number of particles at the moment of the injection into the collider. In addition, Einstein's relativistic time dilation must be included, which increases the mean decay time τ_0 of the muons by γ. Assuming that a fresh bunch is injected into the ring with a certain repetition rate f_r, one finally obtains an expression of

$$\mathcal{L} = \frac{\gamma^2 \tau_0 c}{2C} \frac{N_0^2}{4\pi \epsilon_{\perp,\mathrm{N}} \beta_\perp^*} f_\mathrm{r}. \tag{1.18}$$

According to this definition, it can be seen that the $\mathcal{L}$ increases when $\beta_\perp^*$ reaches small values. Nevertheless, $\beta_\perp^*$ has limited design value at the interaction point, which can be explained by means of the so called hour glass effect [13]. Before the bunch reaches the interaction point, the beam size is squeezed to a minimum value $\sigma_{\perp,0}$. From there to the next optical element, no external field acts on the beam, which is also referred to as a drift. From the interaction point to a certain distance s, $\beta_\perp^*$ changes in the drift as

$$\beta_\perp^*(s) = \beta_{\perp,0}^* + \frac{s^2}{\beta_{\perp,0}^*}, \tag{1.19}$$

where $\beta_{\perp,0}^*$ describes the minimum betatron-function at the collision point. The origin of equation (1.19) can be derived by the mathematical tools of chapter 3. The transverse beam width increases parabolic after the collision, and follows to $\beta_{\perp,0}^* \approx \sigma_z$, i.e. the minimum beta-function at the interaction point is an expression of a minimum longitudinal distance σ_z, which corresponds to the root mean square (rms) bunch length. The bunch length can be described by means of the longitudinal emittance. It is defined as

$$\epsilon_\mathrm{L} = \sigma_z \sigma_\delta, \tag{1.20}$$

where σ_δ describes the relative momentum spread, assuming negligible longitudinal beam correlation at the collision point. Using the normalized longitudinal emittance $\epsilon_{\mathrm{L,N}} = \gamma \epsilon_\mathrm{L}$ ($\beta \approx 1$), the luminosity for the muon collider finally scales to

$$\mathcal{L} = \frac{\gamma^3 \tau_0 c}{2C} \frac{N_0^2 \sigma_\delta}{4\pi \epsilon_{\perp,\mathrm{N}} \epsilon_{\mathrm{L,N}}} f_\mathrm{r}. \tag{1.21}$$

As it can be seen from equation (1.21), the luminosity depends on various accelerator-specific parameters.

- High luminosities are achieved when the circumference of the collider ring is kept as small as possible. The circumference C depends on the strength of the bending magnets in the collider complex, which rise increases the number of collisions and hence, the luminosity. By means of the Lorentz force the luminosity is proportional

to

$$\mathcal{L} \propto \langle B \rangle \frac{N^2 \gamma^2 \sigma_\delta}{\epsilon_{\perp,\mathrm{N}} \epsilon_{\mathrm{L,N}}} f_\mathrm{r}, \tag{1.22}$$

with $\langle B \rangle$ as the average magnetic field of the collider. Increasing beam energies requires higher magnetic fields. Strong focusing at the interaction point sets further challenges for the collider design. It results that the R & D of high magnetic facilities is inevitable.

- The luminosity also depends on the beam current $I \propto \gamma N f_\mathrm{r}$, as follows

$$\mathcal{L} \propto \langle B \rangle \frac{N \gamma \sigma_\delta}{\epsilon_{\perp,\mathrm{N}} \epsilon_{\mathrm{L,N}}} I \tag{1.23}$$

- Due to the muon generation from the hadronic shower, the transverse emittance must be decreased as much as possible, before the beam is injected into $\mu^+\mu^-$ smasher. The process can be ensured by ionization cooling to the beam energies in the MeV range. However, this process increases the energy spread σ_E and therefore the bunch length. Radio frequency (RF) cavities are used to reduce σ_E for preventing high rises in σ_z.

1.3 Muon collider design

The initial design of a possible muon collider has been developed by the previous U.S. Muon Accelerator Program (MAP) study [14, 15] and will be integrated, investigated and improved by the internationl Muon Collider Collaboration (IMCC) study. The pre-accelerator and collider complex is built up in six main structures:

- Proton driver
- Front end
- Cooling channel
- Recirculating linear accelerator
- Accelerator ring
- and Collider.

The arrangement of these main elements is sketched in the Figure 1.2. In the following, the composition of these components will be briefly discussed.

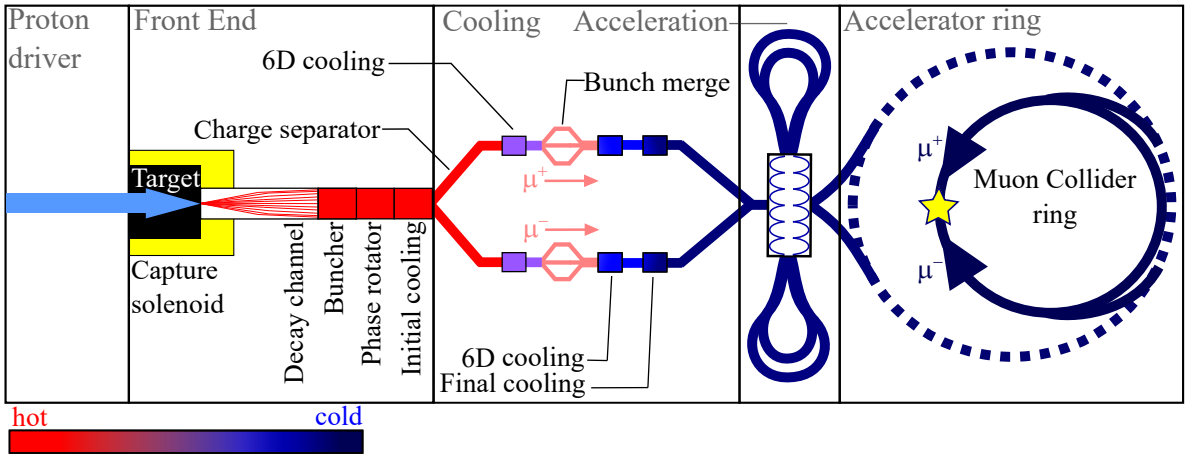

Figure 1.2: For the IMCC studies the MAP design will be adapted and further improved. It contains the front end where the muons are produced from a hadronic shower and further bunched by RF systems. The transverse momenta of the particles and the emittance of the beam have to be reduced by cooling channels to enable further beam injection into a LINAC and a ring accelerator.

Proton driver and front end

Target and decay channel: Generating an intense muon beam is a challenging task. Surrounded by a high solenoid field ($\sim$ 20 T), a multi-GeV proton beam is imping into a target with a power of a few MW [16]. The p^+-target interaction creates a hadronic shower containing negative and positive pions, which further transform in a decay channel ($\sim$100 m) to μ^+ and μ^-. The high magnetic field in the target area should maximize the capture of the charged pions, which have high initial transverse momenta. Past studies [17] suggested Hg [18] and C as possible target candidates, however, more investigations have to be conducted in order to verify, if those materials withstand an appropriate operation time.

Buncher: After rejecting high energy particles by means of a chicane channel [19], a sequence of RF cavities is following, which is confined inside a 1.5 T solenoidal field [19]. The RF frequency f_{RF} and the phase are set to a reference particle in the middle of the initial muon bunch. The RF voltage is increasing, while the f_{RF} decreases, hence maintaining an adiabatic capture of muons into separated bunches. The length of this channel is around 30 m.

Phase rotator: These 40 m long series of cavities set the highest energy particle in the bunch stationary. A decreasing f_{RF} accelerates the low energy particles in the bunch after each cavity. In the end of the bunch, all particles should have the same energy, which means a minimization of the momentum/energy spread. In the end of the channel, the

initial bunch of muons has separated into 21 bunches of μ^+ interleaved with 21 bunches of μ^- [20].

Initial cooling: After the Phase rotator, the beam is matched into an alternating 2.8 T solenoid field in the first cooling channel. Tens of cells are used, with each cell containing absorber blocks and four RF cavities [20]. The principle of ionization cooling will be described further in chapter 4. In the past simulation studies [19] on initial cooling Lithium-Hydrate (LiH) has been used as absorber material. However, other studies also completely exclude the initial cooling sector because of longitudinal emittance growth and to place the charge separator or the 6D-cooling channel straight after the phase rotator [21].

Cooling

Charge separator and pre-merge 6D-cooling: After the front end channel, the beam will be divided into two separate charges by means of bent solenoids [22]. Due to the dispersion, the particles are separated according to their momenta. Therefore, muons with higher energies will be transported through longer absorber paths to ensure more cooling in all 6 phase space directions than for low energy muons. A special target geometry and bending optics has to be designed. In the past, an ionization cooling ring (RFOFO) [23], a cooling (Guggenham) channel [24] and a helical cooling channel (HCC) [25, 26] have been taken into account. Another possible option is a helical FOFO snake channel design [27], where charge separation is not needed. The choice of the most appropriate 6D-cooling design is one of the subjects of the ongoing IMCC study.

Bunch merge: Due to equation (1.21), the luminosity is proportional to the squared number of muons in one bunch. The bunch merge servers to combine the 21 bunches from the front end to one single bunch of each charge. A >100 m long bunch merge contains dozens of RF cavities [28, 29]. At first, the 21 bunches are merged longitudinally into seven bunches. Afterwards, each of those bunches is kicked by a kicker magnet into 7 trombones [30] for a transverse merge. Each trombone has a different arc length, such that all bunches reach a specific re-combination point (funnel) at the same time.

After merge 6D-cooling and final cooling: After the bunch merge, the longitudinal as well as the transverse emittance grow by the factor of 10. Therefore, the beam has to be cooled again with an additional 6D-cooling channel. In the after-merge-cooler, a lower emittance compared to the emittance in the pre-merge channel is achieved [29]. The last stage in the cooling section is the final cooling. It combines several cells, with each cell containing liquid hydrogen absorber in a high magnetic field solenoid (30-50 T), followed by accelerating and phase focusing RF cavities. The goal is to decrease the transverse emittance as low as possible, for maintaining high $\mathcal{L}$ and low machine sizes and therefore minimizing material costs.

Accelerator and collider ring

Acceleration: The cooled bunch has a very low energy (few MeV) and a large longitudinal emittance after the cooling section, i.e. the length of the bunch is wide. Therefore, the beam must be first accelerated with normal conducting (NC) cavities at very low frequencies, whereby the frequency can be increased while reaching higher energy. At the energy of about 1 GeV, the beam will be guided into a super conducting radio frequency (SRF) Recirculation Linear Accelerator (RLA) [31], which has a dog bone geometry. This kind of accelerator is unique and offers a factor two higher RF efficiency, compared to a corresponding race track Linac. After reaching 100 GeV of beam energy, the beam is gaining its final colliding energy (several TeV) with a Rapid Cycling Synchrotron (RCS) [32]. Since it is currently not possible to use superconducting bending magnets for ramping, NC-magnets have to be used, where lower fields will be achieved, which leads to a larger circumference of the ring accelerator.

Collider ring: As one can see from the equation (1.21), the aim is to minimize the circumference of the collider for obtaining high luminosities. Due to the high rigidity of the beam, the field strength in the collider's bending magnets also has to be increased. Assuming a system consisting solely of deflecting magnets, the length of all magnets can be expressed as

$$L[\mathrm{m}] = 2\pi \frac{p/e[\mathrm{kg\,m\,s^{-1}\,C^{-1}}]}{B[\mathrm{T}]} \quad \Rightarrow \quad L[\mathrm{km}] \approx 21 \frac{E[\mathrm{TeV}]}{B[\mathrm{T}]} \tag{1.24}$$

I.e. the collider size strongly depends on the development of super conductor technology in the future. Considering the possibility to build 10 T arcs, a 28.5 TeV muon collider would have a circumference of approximately 30 km which would be similar to one of of the LHC. The usage of exiting collider infrastructure, which is available at CERN, would therefore minimize construction costs and maintain smaller ecological footprint. Additionally, the radiation effects have to be strongly considered. On one hand, due the products of the muon decay

$$\begin{aligned} \mu^+ &\longrightarrow \overline{\nu}_\mu + e^+ + \nu_e \\ \mu^- &\longrightarrow \nu_\mu + e^- + \overline{\nu}_e, \end{aligned} \tag{1.25}$$

ultra high energetic electrons [33] can disturb the superconducting properties of the collider environment, which therefore has to be shielded. On the other hand, due to the high decay rate, the neutrino radiation cannot be neglected anymore. Potential contamination of surrounding area and safety issues need to be considered. Further studies have to be done for neutrino flux mitigation. One possible solution is beam wobbling [34, 35].

Table 1.1: Parameter list defined by the international muon collider collaboration [36].

Parameter	Symbol	Units	3 TeV	10 TeV	14 TeV
Luminosity	$\mathcal{L}$	$10^{34}\,\mathrm{cm}^{-2}\mathrm{s}^{-1}$	1.8	20	40
Muons/bunch	N	10^{12}	2.2	1.8	1.8
Repetition rate	f_r	Hz	5	5	5
Beam power	P_beam	MW	5.3	14.4	20
Collider circumference	C	km	4.5	10	14
Average bending field	$\langle B \rangle$	T	7	10.5	10.5
Norm. long. emittance	$\epsilon_\mathrm{L,N}$	MeV m	7.5	7.5	7.5
Energy spread	σ_E/E	%	0.1	0.1	0.1
Bunch length	σ_z	mm	5	1.5	1.07
Interaction point beta	β	mm	5	1.5	1.07
Norm. trans. emittance	$\epsilon_{\perp,\mathrm{N}}$	μm	25	25	25
Interaction point beam size	$\sigma_\perp$	μm	3.00	0.90	0.63

1.4 Thesis goal and structure

After deriving the luminosity of a muon collider, this chapter sketched the infrastructure of such a novel machine. The goal of this overview was to introduce the reader about the feasibility and technical challenges of this machine.

Chapter 2 discusses the motivation of such a multi TeV collider. The main focus lays on the Higgs particle and its field, which gives massive particles their mass and could possible interact with unknown particles like dark matter. Also the Higgs self interactions by one subject of the investigation, which gives insights into the shape of the Higgs potential. Furthermore, the possible operation of a muon collider of a Higgs factory will be presented, when the muon collider's cm. energy operates at the Higgs resonance.

The theoretical background of this work is based on the behavior of muons inside solenoids. Chapter 3 introduces the magnetostatic of these optics and describes the single particle dynamic in it. This will be further projected on an ensemble of muons, where a beam can be defined by specific parameters in the phase space. This chapter goes into a precise explanation of the transverse emittance, which is one key parameter for the final cooling technique.

For reducing the emittance of a muon beam, a cooling technique especially adapted for muons will be introduced, which is also known as ionization cooling. Back in the days, this method was rarely used in the accelerator physics field and therefore ionization cooling is hardly to find in academical books and publications. For this reason, chapter 4 attempts to describe especially the beam dynamics of ionization cooling and the physics

behind a final cooling cell. An expression described the change of the emittance will be presented, denoted as the cooling equation.

Tests with the simulation code ICOOL bring the opportunity to implement the application of liquid deuterium as absorber material in the ICOOL's legacy code, because it has similar properties to liquid hydrogen and it was never foreseen in previous cooling simulations. Due to the simultaneous transverse focusing of solenoids, the transverse beam parameters are coupled. Chapter 5 describes a decoupling technique, which will be applied on the ICOOL simulations.

Before demonstrating emittance reduction using ICOOL, chapter 6 will describe the solution of the cooling equation by a numerical approximation technique, since it is not possible to solve it analytically. At next, the muons will be tracked in a hard edge solenoid with an absorber inside and the beam parameters will be additionally analyzed by two different codes. One analysis technique is based on a rotating frame, which causes a decoupling of the beam parameters and makes it easy to calculate the emittance. The other code comes from the ICOOL package. Both techniques will be compared with the theoretical prediction and discussed in this chapter. In the final section, the impact of the absorber windows on the emittance will be explored with ICOOL and interpreted.

Finally, one reaches the last and most practically advanced part of this thesis. Chapter 7 introduces the complexity of real solenoids, which have end field effects next to their entrance and exit. A Transfer matrix approach for these kind of solenoids, which motivates the idea of creating a similar lattice matrix by using a sequence of small hard edge field matrices. The main goal of this chapter is to minimize the beam correlation in the absorber area inside the solenoid, which can be achieved by with optimizing the end fields. This will be performed by an analytic model and later applied for the used ionization cooling code. It will be discussed, if it is possible to cool a muon beam below the lowest reached normalized transverse emittance from the past MAP studies [37].

Chapter 2: Physics potential

In the 20th century, particle physics had explained many phenomena by means of the Quantum Electrodynamic (QED) [38–41] and the Quantum Chromodynamic (QCD) [42]. These two mechanism, known as the electromagnetic and strong force, were not sufficient enough to explain multiple physical phenomena, such as the radioactive beta decay. For this type of radioactivity, the nuclear charge number of an atom is changed by emitting an electron (e^-)/ positron (e^+) and an electron-anti-neutrino ($\overline{\nu}_e$)/ electron-neutrino (ν_e).

Already in the 1930s, E. Fermi [43] attempted to explain the beta decay by a 4-fermion-point interaction caused by a short-lived and heavy exchange particle. This transmitting force is known as the weak interaction, whereby C. S. Wu made a great scientific contribution by discovering experimentally the non-conserved parity of the beta decay [44], theoretically predicted by T. D. Lee [45] one year before Wu's famous experiment. Formally, the parity transformation is a sign flip of the three spatial coordinates.

With the hard efforts of C. Rubbia [46, 47] and S. Van der Meer [48], they have been discovered at CERN's Super Proton Synchrotron (SPS) two charged $W^{+/-}$ and one neutral Z^0 spin-1 vector bosons, during proton anti-proton collisions. The properties of the Z^0 boson additionally lead to a mixture of the electromagnetic and weak interaction, which was already predicted by S. L. Glashow [49], A. Salam [50] and S. Weinberg [51] and combined these two forces to the origin of the names Glashow-Salam-Weinberg (GSW) electroweak unification.

In those times, the masses of these new vector bosons could not be explained. Also the mechanism which gives the fermions their mass has not been inquired, because it was a matter of course that the terrestrial life is "solid" and "compact". Nevertheless, the young theorists P. W. Higgs [52] and F. Englert with R. Brout [53] independently searched for a new mathematical unification. They created a theoretical technique, where massive particles generate their masses by coupling with a certain field, also know as the Brout-Englert-Higgs (BEH) field. This kind of mass generation is called the BEH mechanism. This chapter provides motivation for the investigation of building a muon collider by

some basic analytical calculations and approximations from the particle physics point of view.

2.1 Cross section

The effective cross section is an expression that describes the probability of an interaction between approaching particles. Consider type **a** particles propagate with a flux $\phi_{\mathbf{a}}$ through a region with density $n_{\mathbf{b}}$ (particles per unit volume), the interaction rate in this region can be expressed as

$$r_{\mathbf{b}} = \sigma \cdot \phi_{\mathbf{a}}, \tag{2.1}$$

where σ describes the interaction probability between particle **a** and **b**. Lets further assume a finite time δt, where **a**-particles pass with velocity $v_{\mathbf{a}}$ through a defined surface A with $\delta N_{\mathbf{b}} = n_{\mathbf{b}}(v_{\mathbf{a}} + v_{\mathbf{b}})A\delta t$ particles of type **b** moving with velocity $v_{\mathbf{b}}$ in opposite direction, visualized in Figure 2.1 on the left side.

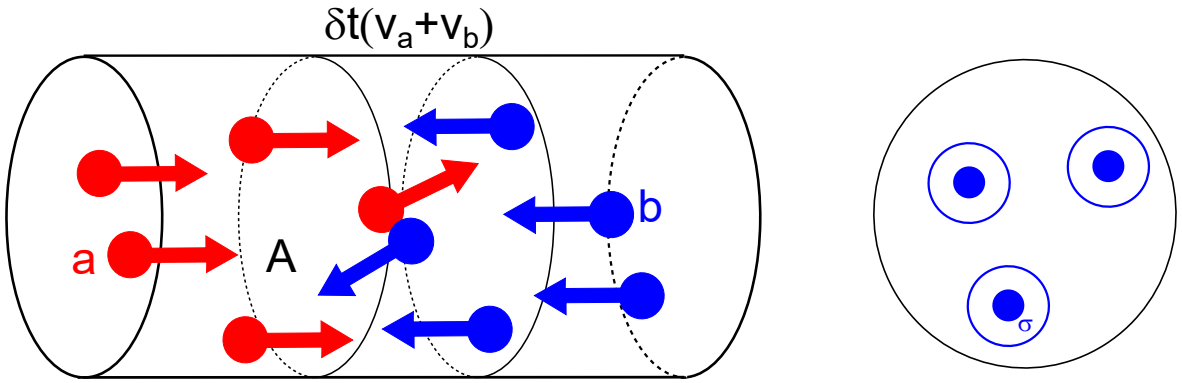

Figure 2.1: The **left** sketch shows colliding particles which are interacting in a small region. The **right** figure illustrates the projected view of a penetrating particles, where an interaction only takes place, when it is imping into the cross section σ, placed around a target particle.

An interaction only takes place, if particle **a** penetrates through the surface σ (Figure 2.1 right), which is known as the cross section. In classical physics, σ is $\pi(r_{\mathbf{a}} + r_{\mathbf{b}})^2$, which is an expression of the colliding particles' radii $r_{\mathbf{a}}, r_{\mathbf{b}}$. In particle physics, σ comes from a quantum mechanical approach described by an average value, that still allows an interaction, by exchanging a virtual particle. For that reason, the interaction probability can be described by

$$\delta P = \frac{\delta N_{\mathbf{b}} \cdot \sigma}{A} = n_{\mathbf{b}}(v_{\mathbf{a}} + v_{\mathbf{b}})\sigma\, \delta t, \tag{2.2}$$

which further results to an interaction rate

$$r_{\mathbf{a}} = \frac{\delta P}{\delta t} = n_{\mathbf{b}}(v_{\mathbf{a}} + v_{\mathbf{b}})\sigma. \tag{2.3}$$

Generalizing the rate $r_{\mathbf{a}}$ for a finite number of **a**-particles for a beam with $N_{\mathbf{a}} = n_{\mathbf{a}} \cdot V$ particles it further develops to a generalized rate

$$r = r_{\mathbf{a}}\, n_{\mathbf{a}}\, V = (n_{\mathbf{a}} v)(n_{\mathbf{b}} V)\sigma = \phi_{\mathbf{a}}\, N_{\mathbf{b}}\, \sigma \tag{2.4}$$

with $v = v_{\mathbf{a}} + v_{\mathbf{b}}$ and is consistent with definition (2.1). Normalizing the interaction rate for one particle per volume leads to the transition matrix element

$$\Gamma_{fi} = \frac{v_{\mathbf{a}} + v_{\mathbf{b}}}{V}\sigma, \tag{2.5}$$

which can be derived by Fermi's golden rule [41, 43]. Normalizing this equation using the one particle per volume approach $n_{\mathbf{a}} = n_{\mathbf{b}} = 1/V$, where V can be described by an unitary cell, the cross section scales to

$$\sigma = \frac{\Gamma_{fi}}{v_{\mathbf{a}} + v_{\mathbf{b}}}. \tag{2.6}$$

Defining a suitable expression for the transition rate requires a complicated derivation, which would be beyond the scope of this work. It can be verified by means of reference [54], allowing to describe the cross section by the following structure

$$\sigma = \frac{1}{4E_{\mathbf{a}}E_{\mathbf{b}}} \frac{1}{(2\pi)^2} \frac{p_f}{4\sqrt{s}} \int |M_{fi}|^2 \, d\Omega, \tag{2.7}$$

in case of a collision in the cm. frame, where $E_{\mathbf{x}}$ ($\mathbf{x} = \mathbf{a}, \mathbf{b}$) describes the energy of particle **a** and **b** in the cm. frame, the cm. energy of the system $\sqrt{s} = E_{\mathbf{a}} + E_{\mathbf{b}}$ and the final momentum p_f of the particle after its collision. The expression within the solid angle Ω integral stands for the Lorentz invariant transition matrix element M_{fi}.

The value $4E_{\mathbf{a}}E_{\mathbf{b}}$ in equation (2.7) can be expressed by the flux factor (1.9) and the Lorentz invariant properties of equation (2.7). When colliding particles have the same initial momentum p_i, the flux factor can be also expressed as

$$F = 4E_{\mathbf{a}}E_{\mathbf{b}} \left(\frac{p_i}{E_{\mathbf{a}}} + \frac{p_i}{E_{\mathbf{b}}} \right) = 4p_i(E_{\mathbf{a}} + E_{\mathbf{b}}) = 4p_i\sqrt{s} \tag{2.8}$$

with the cm. energy $E_{\mathbf{a}} + E_{\mathbf{b}} = \sqrt{s}$. Thus, the cross section of the Lorentz-invariant two

body collision can be defined as

$$\sigma = \frac{1}{64\pi^2 s}\frac{p_f}{p_i}\int |M_{fi}|^2 \, d\Omega. \tag{2.9}$$

2.2 BEH mechanism

Unlike in quantum mechanics, in which the particle are represented as a wave function, one can use the principle of quantum field theory, in which the particles are described as excitations of the a quantum field. Instead of the Schrödinger equation (or the Dirac equation in the relativistic case) the Euler-Lagrange equation is used

$$\frac{\mathrm{d}}{\mathrm{d}t}\left(\frac{\partial L}{\partial \dot{q}_\mathrm{i}}\right) - \frac{\partial L}{\partial q_\mathrm{i}} = 0, \tag{2.10}$$

with the Lagrangian $L(q_\mathrm{i}, \dot{q}_\mathrm{i})$, q_i, which is a function of a set of generalized coordinates q_i and $\dot{q}_\mathrm{i}$ (the dot is the time derivative of q_i). In the case of a system of particles with n generalized coordinates, the Lagrangian can be exchanged by the Lagrange density $\mathcal{L}$ and the generalized coordinates are replaced by the time-space depending fields $\phi_\mathrm{i}(x^\mu)$ and forms to

$$\partial_\mu\left(\frac{\partial \mathcal{L}}{\partial(\partial_\mu \phi_\mathrm{i})}\right) - \frac{\partial \mathcal{L}}{\partial \phi_\mathrm{i}} = 0, \tag{2.11}$$

where the derivative is defined as

$$\partial_\mu \phi_\mathrm{i} \equiv \frac{\partial \phi_\mathrm{i}}{\partial x^\mu}. \tag{2.12}$$

Lets consider the Lagrangian of the Dirac equation

$$\mathcal{L}_\mathrm{Dirac} = i\overline{\psi}\gamma^\mu\partial_\mu\psi - m\overline{\psi}\psi \tag{2.13}$$

with m as the fermion mass, i the imaginary number, ψ the spinor field and γ^μ as the gamma matrix. The definition of the gamma matrices in the Dirac-Pauli notation are

$$\gamma^0 = \begin{pmatrix} \mathbb{1} & 0 \\ 0 & -\mathbb{1} \end{pmatrix} \qquad \gamma^k = \begin{pmatrix} 0 & \sigma_\mathbf{k} \\ -\sigma_\mathbf{k} & 0 \end{pmatrix}, \tag{2.14}$$

where $\sigma_\mathbf{k}$ $(k = 1, 2, 3)$ represents the Pauli matrices. Equation (2.13) must be invariant under a U(1) local phase transformation of the field $\psi(x) \to \psi'(x) = e^{iq\chi(x)}\psi(x)$ with

the local phase $\chi(x)$ and the charge q in the exponent. Nevertheless, in doing so

$$\begin{aligned}\mathcal{L}_{\text{Dirac}} \rightarrow \mathcal{L}'_{\text{Dirac}} &= i\overline{\psi}'\gamma^\mu\partial_\mu\psi' - m\overline{\psi}'\psi' \\ &= ie^{-iq\chi}\overline{\psi}\gamma^\mu[e^{iq\chi}\psi + iqe^{iq\chi}\partial_\mu(\chi)] - m\overline{\psi}\psi \\ &= \mathcal{L}_{\text{Dirac}} - q\overline{\psi}\gamma^\mu\partial_\mu(\chi)\psi,\end{aligned} \tag{2.15}$$

it can be determined, that the Lagrangian of equation (2.13) is not gauge invariant. Therefore, a covariant derivative and an additional gauge field must be introduced

$$\begin{aligned}D_\mu &= \partial_\mu + iqA_\mu \\ A'_\mu &= A_\mu - \partial_\mu\chi,\end{aligned} \tag{2.16}$$

for establishing the invariance, whereby the unwanted term $q\gamma^\mu\partial_\mu(\chi)$ will be finally canceled. Thus the new gauge invariant Lagrangian for spin-$\frac{1}{2}$ fermions leads to

$$\mathcal{L}_{\text{Fermion}} = \overline{\psi}(i\gamma^\mu\partial_\mu - m)\psi - q\overline{\psi}\gamma^\mu A_\mu\psi, \tag{2.17}$$

with an additional exchange gauge boson, also know as the photon. The expansion of this expression by introducing the gauge invariant kinetic term $F_{\mu\nu}F^{\mu\nu}$, the QED Lagrangian for an electron with charge $q = -e$ and the massless interaction photons can be described by

$$\mathcal{L}_{\text{QED}} = \overline{\psi}(i\gamma^\mu\partial_\mu - m)\psi + e\overline{\psi}\gamma^\mu A_\mu\psi - \frac{1}{4}F_{\mu\nu}F^{\mu\nu}. \tag{2.18}$$

The local gauge principle is an elegant description of the standard model in QED and QCD, but the local gauge invariance for massive particles of the weak interaction is destroyed.

For that reason, Brout, Englert and Higgs introduced a scalar field

$$\mathcal{L}_{\text{Scalar}} = \frac{1}{2}(\partial_\mu\phi)^*(\partial^\mu\phi) - V(\phi) = \frac{1}{2}(\partial_\mu\phi)^*(\partial^\mu\phi) - \frac{1}{2}\mu^2\phi^2 - \frac{1}{4}\lambda\phi^4, \tag{2.19}$$

where the first term in $\mathcal{L}_{\text{Scalar}}$ is the kinetic term of the scalar field ϕ, the second term is an expression of the particle mass μ and the third term is associated with the self interaction of this scalar field $\lambda > 0$. If $\mu^2 > 0$, the potential has its minimum at 0 (Figure 2.2 left), but else if $\mu^2 < 0$, the potential has two minima at $-v$ and v and one maximum at 0, which can be seen in Figure 2.2 on the right hand side.

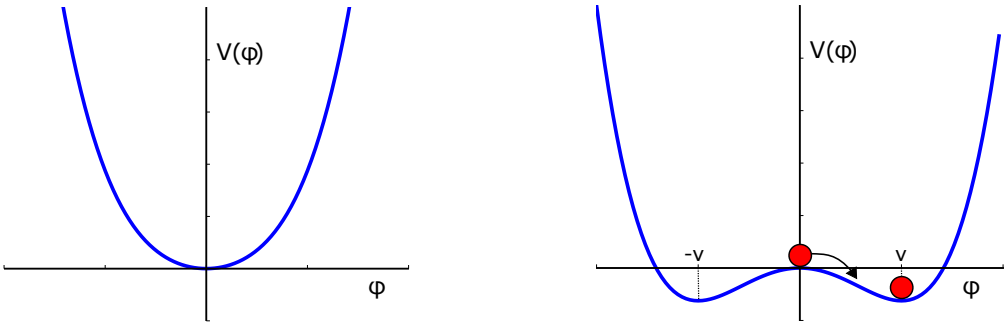

Figure 2.2: The scalar field have one minimum for negative μ (left), but two in the positive values of μ which are known as the vacuum states.

The derivation of this equation (2.19) exhibits the two vacuum states

$$v = \pm\sqrt{\frac{-\mu}{\lambda}}. \tag{2.20}$$

If one takes the liberty to decide between the two vacuum states, the symmetry is broken. For the following calculation, the positive value v will be chosen for simplicity.

Lets assume, that in the early beginning of the universe, where all particle were massless, the scalar potential was not in any minimum state. For simplicity, lets imagine a particle place on the maximum of the potential and falls spontaneously into one of the minima, which results in a total break of the system's symmetry, like it is illustrated in Figure 2.2. Compared to classical mechanics, the particle does not simply remain stationary in the potential's valley, but oscillates back and forth around the vacuum state, which can be regarded as an excitation around this state

$$\phi(x) = h(x) + v. \tag{2.21}$$

Inserting this new expression with the new excited field h into equation (2.19) leads to

$$\begin{aligned}\mathcal{L}(h) &= \frac{1}{2}(\partial_\mu h)^*(\partial^\mu h) - \lambda^2 v h^2 - \lambda v h^3 - \frac{1}{4}\lambda h^4 + \frac{1}{4}\lambda v^4 \\ &= \frac{1}{2}(\partial_\mu h)^*(\partial^\mu h) - \frac{1}{2}m_h^2 h^2 + \text{triple} + \text{quartic} + \text{const},\end{aligned} \tag{2.22}$$

where $\frac{1}{2}(\partial_\mu h)^*(\partial^\mu h)$ describes the kinetic term of the h-field and $m_h = \sqrt{2\lambda v^2}$ the mass of this spin-0 particle. The next two terms describe the cubic and the quartic interaction of the scalar field, where λv is the coupling constant of the triple and $\frac{1}{4}\lambda h^4$ the one of the quartic interaction. These self interactions can be illustrated as Feynman diagrams

in Figure 2.3. The constant $\frac{1}{4}\lambda v^4$ has no physical meanings and it will be therefore not considered in the further calculations of this chapter.

Figure 2.3: Cubic (left) and quartic (right) self interaction of the h-field.

In summary, the BEH mechanism is based on the following three techniques:

- spontaneous symmetry break and choice of a specific vacuum state,
- field perturbation at this vacuum state and
- covariant derivative exchange with local gauge transformation subsequently.

This rule helps to understand the generation of electroweak boson and fermion masses, while the last mentioned one will be explained in detail in the next section.

2.3 Fermionic mass generation

The leptons and quarks generate their masses by coupling to the BEH field, which was described by H. Yukawa [55]. The fermionic field can be expressed by a left-handed isospin doublet f_L and a right-handed isospin singulett f_R. For leptons and down-like particles, the $\mathrm{SU(2)_L}$-$\mathrm{U(1)_Y}$ Lagrangian yields to

$$\mathcal{L}_\mathrm{fermion} = -g_f \left(\overline{\psi}_\mathrm{L}\phi\psi_\mathrm{R} + \overline{\psi}_\mathrm{R}\overline{\phi}\psi_\mathrm{L}\right), \tag{2.23}$$

where g_f is the coupling constant of the fermion-Higgs vertex and ϕ as a doublet state of the Higgs field. After the symmetry break the Lagrangian for e.g. leptons scales to

$$\begin{aligned}\mathcal{L}_\mathrm{lepton} &= -\frac{g_e}{\sqrt{2}}\left[\begin{pmatrix}\overline{\nu}_e & \overline{e}\end{pmatrix}_\mathrm{L}\begin{pmatrix}0\\ v+h\end{pmatrix}e_\mathrm{R} + \overline{e}_\mathrm{R}\begin{pmatrix}0 & v+h\end{pmatrix}\begin{pmatrix}\nu_e\\ e\end{pmatrix}_\mathrm{L}\right]\\ &= -\frac{g_e}{\sqrt{2}}\left[\overline{e}_\mathrm{L}e_\mathrm{R}v + \overline{e}_\mathrm{L}e_\mathrm{R}h + \overline{e}_\mathrm{R}e_\mathrm{L}v + \overline{e}_\mathrm{R}e_\mathrm{L}h\right].\end{aligned} \tag{2.24}$$

The same derivations can be done with up-like particles by using the charge conjugation operator $-i\sigma_2$ on the isospin states ψ. In general, the fermion mass can be easily

expressed by the first term in equation (2.24) and yields to $m_f = -g_f v/\sqrt{2}$, which further gives an expression of the Higgs-fermion coupling term

$$g_{\mathrm{H\bar{f}f}} = -\frac{im_f}{v} \tag{2.25}$$

and is needed for some calculations in one of this chapter's section. Before that, it is worth to mention, that the BEH mechanism does not generate neutrino masses. Nevertheless, due to neutrino oscillations, a group around the Super-Kamiokande experiment proofed the appearance of a non-zero neutrino mass [56]. Therefore, the BEH theory reaches its limits, which is an indication of BSM physics.

2.4 Possibilities for discovering hidden sectors

What can be achieved with $\mu^+\mu^-$ collisions are the still undiscovered self interactions of the Higgs particle, illustrated in Figure 2.3. Due to this, the Higgs sector cannot be fully confirmed without measuring the cubic and quartic self interaction coupling constants as well the Higgs-electroweak couplings. Their determination is crucial for exploring possible different λ-values of equation (2.19), which finally defines the shape of the Higgs potential [57, 58] in Figure 2.2. Additionally, this would open new doors for studying the electroweak symmetry break precisely. However, with a future 100 TeV p^+p^+ collider it would be extremely challenging to measure these kind of scalar self couplings [59, 60].

A multi-TeV muon collider in the $10^{35}\,\mathrm{cm}^{-2}\mathrm{s}^{-1}$ luminosity range provides the indication of the cubic and quartic self coupling [61]. The only processes, which are able to create such self interactions is Higgs-strahlung or at $\sqrt{s} \gtrsim 1.5\,\mathrm{TeV}$ W-boson fusions are dominated since the cross sections scales with $\sigma \sim \log(s)$ [61]. This two processes are depicted in Figure 2.4.

What can still be found out is whether the Higgs is connected to other scalar/vectorial particles, which are still totally unknown. Since it couples with all mass-bearing SM particles (except neutrinos), it is possible that Higgs is connected with unknown massive matter. New stable particles interacting with BEH field would be excellent dark matter candidates.

It is in a high interest to accelerate the investigation of Higgs physics. As this section already showed new physics seem to be hidden behind the Higgs particle, which is also known as the Higgs portal model [62]. After providing several physical motivation to build a muon smasher, the IMCC tries to proof the feasibility of such a discovery machine. Nevertheless, there exists a concept of a pre-stage in the low energy range described in the next section, which would be suitable for a possible test facility.

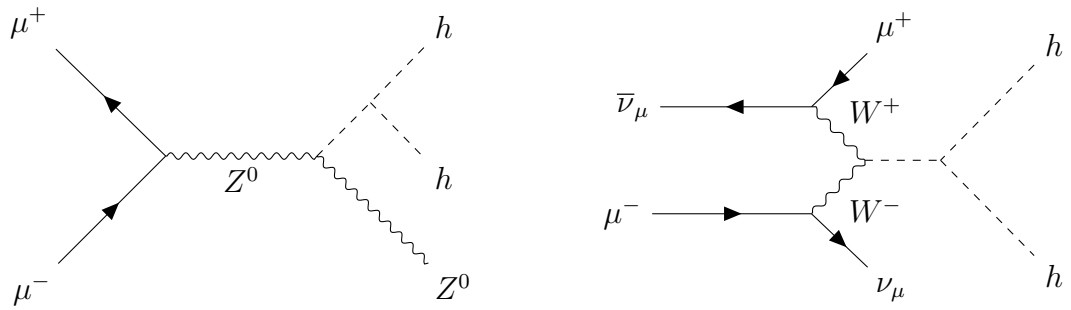

Figure 2.4: Two possibilities of cubic Higgs interaction processes at a $\mu^+\mu^-$ collision exist: **Righ**t: Higgs-strahlung; **Left**: W fusion with (or Z^0 fusion at higher energy).

2.5 Higgs factory as a pre-stage option

Before constructing a multi TeV muon collider, one option is to work with well cooled muon beams in the low energy range in form of preliminary stage. Based on the higher coupling of the muons to the Higgs field (explained in section 2.3) the next paragraphs proof the feasibility to suggest a muon collider based Higgs factory as a pre-stage facility. With such a machine it would be able to measure the Higgs's mass and its decay width very precisely.

For calculating a s-channel Higgs event, it is necessary to introduce helicity of a particle. This is a four-vector, which describes the projection of one particle's or antiparticle's spin on its momentum. While a particle/antiparticle has one of the two different spin states, depends on spherical polar coordinates (θ, ϕ) of the momentum p. The so called spinors $u_\uparrow$ and $u_\downarrow$ describe the particles up and down helicity, while $v_\uparrow$ and $v_\downarrow$ are the spinors of the antiparticle.

In the ultra relativistic limit ($E \gg m$), up and down helicity states transforms into Lorentz invariant right and left handed chiral states:

$$\begin{aligned} u_\mathrm{R} &= \sqrt{E}\begin{pmatrix} c \\ s\,e^{i\phi} \\ c \\ s\,e^{i\phi} \end{pmatrix}, \qquad u_\mathrm{L} = \sqrt{E}\begin{pmatrix} -s \\ c\,e^{i\phi} \\ s \\ -c\,e^{i\phi} \end{pmatrix} \\ v_\mathrm{R} &= \sqrt{E}\begin{pmatrix} s \\ -c\,e^{i\phi} \\ -s \\ c\,e^{i\phi} \end{pmatrix}, \qquad v_\mathrm{L} = \sqrt{E}\begin{pmatrix} c \\ s\,e^{i\phi} \\ c \\ s\,e^{i\phi} \end{pmatrix} \end{aligned} \tag{2.26}$$

where $s = \sin(\theta/2)$ and $c = \cos(\theta/2)$ were written for simplifications. Lets assume a Higgs creation by a high energy $\mu^+\mu^-$ annihilation (a so called s-channel), which further

decays into the most proper bottom (often called beauty) meson $\bar{b}b$ pair. It is possible to construct the matrix element of this interaction process by means of the corresponding Feynman diagram in Figure 2.5 left.

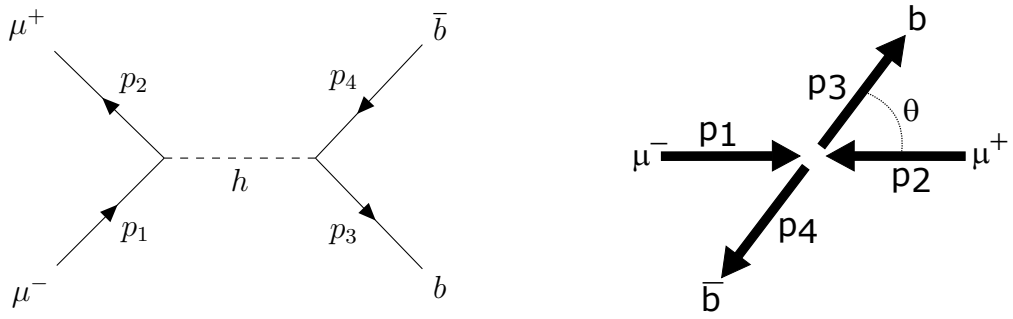

Figure 2.5: Left: The s-channel Feynman diagram illustrates the creation of the Higgs particle due to $\mu^+\mu^-$ annihilation. The Higgs further decays into to the most proper $b\bar{b}$-pair. Right: Scattering kinematic of the muon collision in the $\phi = 0$ plane.

For the matrix element, the four-current of the μ- and b-channel has to be evaluated by means of the Feynman rules [54]. The Lorentz-invariant currents are composed of the chiral states multiplied in the opposite flux direction, which are linked to the coupling strengths with the BEH field from section 2.3. Together with the Higgs propagator the Matrix element can be formed to

$$-iM_{fi} = \left[\overline{v}(p_2)\left\{-i\frac{m_\mu}{v}\right\}u(p_1)\right]\frac{1}{q^2 - m_{\mathrm{H}}^2 + im_{\mathrm{H}}\Gamma_{\mathrm{H}}}\left[\overline{u}(p_3)\left\{-i\frac{m_b}{v}\right\}v(p_4)\right]. \tag{2.27}$$

Due to the scalar properties of h, only left-left or right-right handed four-currents are unequal zero. The factor Γ_{H} in the propagator is the total decay width of the Higgs and has the value of approximately 1.3 MeV [63]. The bar over the first chiral states in each four-current is the corresponding adjoint spinor of $\overline{u} = u^\dagger\gamma^0$ or $\overline{v} = v^\dagger\gamma^0$.

Due to the Lorentz invariant properties of M_{fi}, it is possible to make the calculation in the rest frame of the Higgs particle. The spherical polar coordinates for the chiral states can be evaluated by means of Figure 2.5 right and will be simplified by choosing the unitary plane $\phi = 0$. Further, the four possible matrix elements scale in the Higgs frame to

$$M_{\mathrm{RR\,RR}} = M_{\mathrm{LL\,LL}} = -M_{\mathrm{RR\,LL}} = -M_{\mathrm{LL\,RR}} = \frac{m_\mu m_b}{v^2 m_{\mathrm{H}}\Gamma_{\mathrm{H}}}\,4E^2, \tag{2.28}$$

where $E = m_{\mathrm{H}}/2$ is the muon energy. By means of the squared matrix element

$$\langle|M|^2\rangle = \frac{1}{4}\left[|M_{\mathrm{RR\,RR}}|^2 + |M_{\mathrm{RR\,LL}}|^2 + |M_{\mathrm{LL\,RR}}|^2 + |M_{\mathrm{LL\,LL}}|^2\right], \tag{2.29}$$

the cross section for the Higgs s-channel can be evaluated with equation (2.9) and scales to

$$\sigma_{\mu^+\mu^-\to h\to\bar{b}b} = \frac{m_\mu^2 m_b^2}{16\pi v^4} \frac{s}{\left(s - m_{\mathrm{H}}^2\right)^2 + m_{\mathrm{H}}^2 \Gamma_{\mathrm{H}}^2}, \tag{2.30}$$

which is a type of the so called Breit-Wigner resonance formula.

In the case of direct Higgs production via e^+e^- annihilation, the cross section would be the same like (2.30), but replacing m_μ with m_e. While the electron is 200 times lighter than the muon, the cross section of the muon smasher would be $4 \cdot 10^4$ higher than what can be achieved by an electron collider, which motivates the idea of muon driven Higgs factory.

Nevertheless, it must be taken into account, that muon annihilations and corresponding b-pair creations can be also mediated by electroweak processes. A positive and negative muon can create as well a neutral particle like a photon or a Z boson as depicted in the Feynman diagram in Figure 2.6.

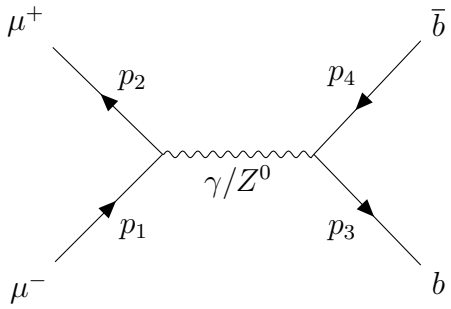

Figure 2.6: Photon/Z^0 boson exchange process for a b-pair production caused by a $\mu^+\mu^-$ annihilation.

For QED like processes, the cross section depends only on the charge of the involved particles, which is the same for electrons and muons ($l^\pm = e^\pm, \mu^\pm$). A bottom-muon pair interaction by a photon scales to the cross section of

$$\sigma_{l^+l^-\to\gamma\to\bar{b}b} = \frac{4\pi\alpha^2}{27s} \tag{2.31}$$

In such a lepton collider, this b-pair production appears also from a Z^0 creation after a $\mu^+\mu^-$ annihilations. The final cross section of this process is a combination of vectorial c_V and axial-vectorial c_A leptonic and down-kind coupling constants. Applying the

Feynman rules, the cross section scales to

$$\sigma_{l^+l^-\to Z\to\bar{b}b} = \frac{g_Z^4 m_Z^2 s}{192\pi} \frac{\left[\left(c_V^l\right)^2 + \left(c_A^l\right)^2\right]\left[\left(c_V^b\right)^2 + \left(c_A^b\right)^2\right]}{\left(s - m_Z^2\right)^2 + m_Z^2\Gamma_Z^2}, \tag{2.32}$$

where g_Z is the coupling of the physical Z^0 Boson, Γ_Z its decay width and m_Z the mass of the Z^0 boson. All used parameters in equation (2.32) are collected in the Particle Data Group (PDG) [63] .

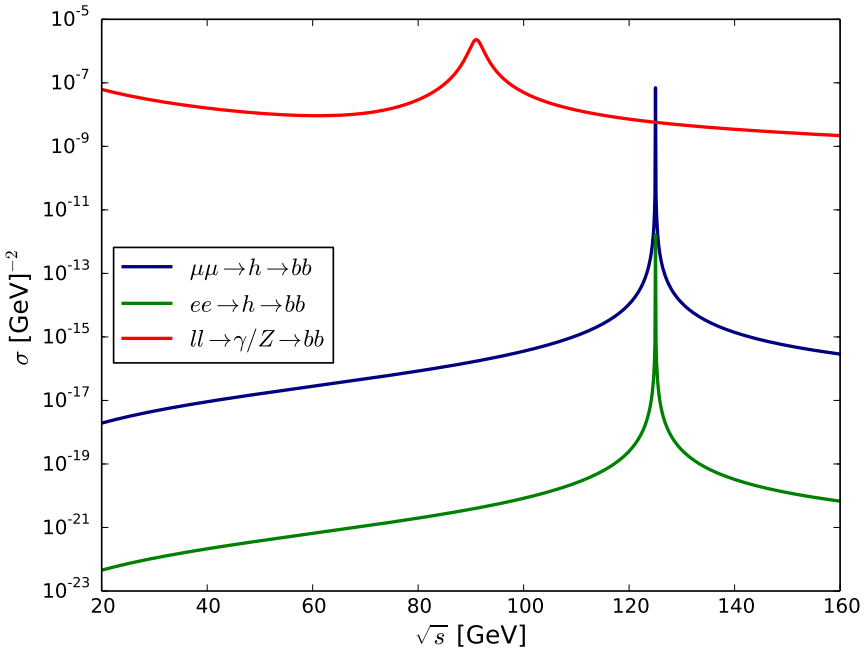

Figure 2.7: At the Higgs resonance the collision of muons is several magnitudes higher than with electrons. The mediation via γ/Z^0 is for electrons and muons the same, because these processes are only charge depended. Higgs created by electron annihilation could not be detected, due to the high background of the γ and Z^0 creation.

Comparing the s-channel of the Higgs creation with the electroweak process in Figure 2.7, it is indeed possible to produce Higgs particles with muons, depicted as the blue line in the graph. Compared with electron-positron collision, a direct Higgs creation would never be possible due to the electrons weak Higgs coupling constant g_e. Electron colliders for Higgs factories would only be possible as a linear collision complex in the TeV range for mitigating synchrotron radiation. Proposed linear colliders like the Compact Linear Collider (CLIC) [64, 65] and the International Linear Collider (ILC) [66, 67] generate Higgs via WWH and ZZH processes, as shown depicted in Figure 2.4.

As it can be seen in Figure 2.7, the width of the Higgs resonance is very thin, which leads to the requirement of a very small energy spread for a future muon collider design. A recent discussion predicts an energy spread of around 0.004% for muon collider operating at 125 GeV cm. energy [68]. Therefore, ionization cooling with 6D-cooling cells plays a crucial role for a muon driven Higgs factory.

Luminosity requirements are several orders of magnitudes lower than for a multi TeV muon collider [14]. Nevertheless, since the luminosity is inverse proportional to the cubic cm. beam energy, a small emittance has to be achieved, which could be provided by final colling cells. However, the final cooling follows to higher energy spreads and it would be difficult to scan the resonance of the Higgs particle.

This chapter gave a brief motivation why a muon collider should be built as a next generation accelerator machine. As mentioned, the final cooling is one of the bottle necks of the proposed collider design and is the main focus of this thesis. Ionization cooling is the target technology for a final cooling cell and is a kind of exotic technique in accelerator science because it almost had never come into use. Therefore, this thesis continues with the beam dynamics of solenoids, which are main components of a final cooling cell. After that, this work will follow with the physics behind ionization cooling.

Chapter 3: Beam dynamics

The main goal of this thesis is to describe and investigate the method of squeezing a spread muon beam and reducing its transverse momenta in the same time, what is especially applied in a final cooling cell. The formal description of the cooling technique applied in the muon collider design studies requires the introduction to accelerator typical beam parameters, which are usually defined by means of beam dynamical formalism provided in this chapter.

Accelerator scientists usually use a standard coordinate system, which is curvilinear. It follows the path s of an ideal particle and points towards the direction of the beam line. One uses the term of a so called reference orbit for such an individual track. Perpendicular to s is the horizontal x-axis, which outwards radial of the ideal orbit. The vertical coordinates are directed in the y-axis. Referred to the reference orbit, each particle motion can be described by that orthogonal system (x, y, s), which is also known as the Frenet-Serret space and is illustrated in Figure 3.1.

It is useful to introduce a co-moving tangential z-axis in addition. Together with the vertical and radial axes, they describe a Cartesian coordinate system. The axes of s and z differ by their metric from each other. In particular, this thesis is following mostly the particle motions in the x-y-plane, which is also known as transverse beam dynamics. For completeness, physical descriptions along the s axis is usually referred to as longitudinal beam dynamics.

It is sufficient to define the 6-dimensional phase space coordinates for a complete description of a particle, which are composed of 3 spatial and 3 momentum deviations

$$\begin{pmatrix} x, & p_x, & y, & p_y, & z, & p_z \end{pmatrix}^\top . \tag{3.1}$$

Accelerator physicists usually assume that the quotient of the transverse momentum $p_{x,y}$ and the longitudinal one p_z is very small compared to 1 (assumption: $p_z \approx p_s$). According to linear approximation, it is possible to express the transverse momenta as angles

$$x' = \frac{\partial x}{\partial s} \approx \frac{p_x}{p_s} \quad \text{and} \quad y' = \frac{\partial y}{\partial s} \approx \frac{p_y}{p_s}, \tag{3.2}$$

which are the derivatives with respect to s. The angles are often differentiated according to z, but the resulting differences to equations (3.2) are negligible in the linear approximation [69].

The longitudinal displacement of a particle from the ideal one with velocity v_s can be described as

$$l = -v_s \left(t - t_s\right), \tag{3.3}$$

where the expression in brackets describes the time delay between the reference and objective particle. The momentum deviation specifying the momentum p of a particle relative to the reference one p_s is defined as

$$\delta = \frac{p - p_s}{p_s} = \frac{\Delta p}{p_s}. \tag{3.4}$$

Distinguishing between momentum and angle phase spaces, text books sometimes define the so called trace space in case of an angle depended beam description [70], which is finally summarized to

$$\left(x, \quad x', \quad y, \quad y', \quad l, \quad \delta\right)^\top. \tag{3.5}$$

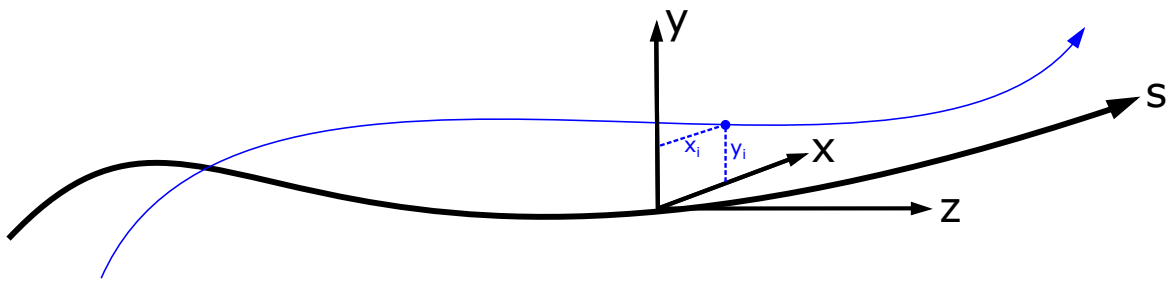

Figure 3.1: The Frenet-Serret coordinate system is curvilinear and follows an ideal trajectory s. An addition Cartesian system can be introduced as well at any position of s.

For this work, high field (HF) solenoids will be used as focusing elements in a final cooling cell. Before a single particle trajectory can be described in such an optical component, it is necessary to understand the field dynamics of such solenoids.

3.1 Magnetostatics of solenoids

The solenoid field is assumed to be stationary, or in other words, if it is not changing in time. Hence, the time depending terms in Maxwell's equations cancel away and the

magnetic field $\vec{B}$ contained equations reduce to

$$\nabla \vec{B} = 0, \tag{3.6}$$

$$\nabla \times \vec{B} = \mu_0 \vec{j}. \tag{3.7}$$

Those are the fundamental field descriptions of magnetostatics, where the law (3.6) describes that there are any field divergences demonstrating the non existence of magnetic monopoles. Formula (3.7) is known as the Ampere's law and expresses an electrical current flux $\vec{j}$ induced by a rotating field. Solenoids are usually made out of wounded helical coils and create a dipole field, when the wires are supplied by direct current I.

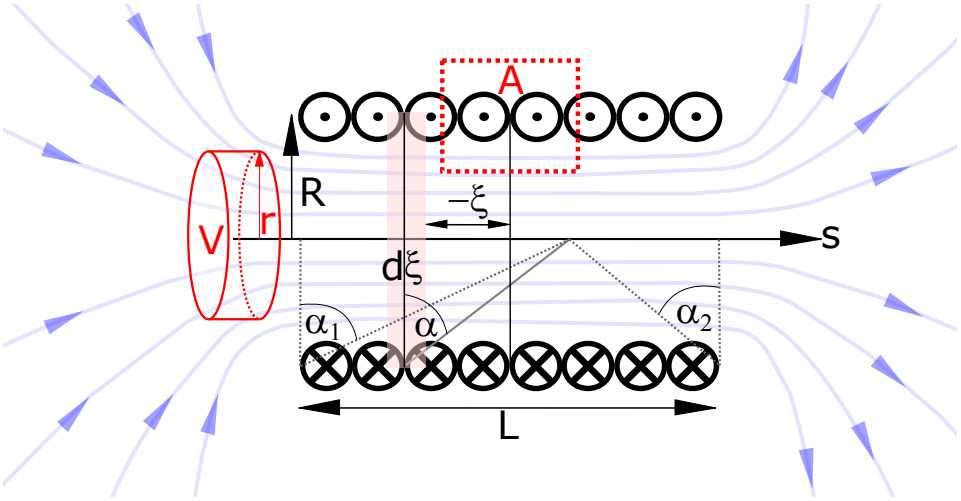

Figure 3.2: For a solenoid of length L and radius R, the almost constant field inside can be calculated by using the integral over area A. The radial parts of the end fields can be determined by integrating an additionally introduced cylinder with volume V and radius r. The axial field strength at any point at s is the summation of the coil elements $d\xi$ from the beginning α_1 of the coil to its end α_2.

It can be assumed, that the field is approximately constant inside the solenoid and its value can be calculated by the following approach. If one imagines an arbitrary closed curve with surface A, like it is depicted in Figure 3.2, it possible to apply the surface integral on equation (3.7). By means of Stoke's theorem the surface integral applied on a rotation is equal to the loop integration, and the field in a solenoid yields to

$$\oint \vec{B}\, d\vec{s} = N\mu_0 I \quad \rightarrow \quad B_s = n\mu_0 I, \tag{3.8}$$

where N is the number of loops of the solenoid and n the loops per unit length.

As it can also be seen in Figure 3.2, the field in front of the entrance and behind the

exit of the solenoid has a radial component B_r, which is commonly called fringe field. To express it mathematically, one can consider an arbitrary cylinder with volume V and radius r illustrated in Figure 3.2. In doing the integration of equation (3.6) over this volume, the divergence disappears by applying Gauss's theorem and the volume changes to a surface integration of the cylinder. From the center comes a magnetic flux of $\pi r^2 B_s$ flowing through the entrance of that concentric cylinder. Considering an infinitely long cylinder, at one point, the flux is going to exit the side surface, which can be expressed as

$$r^2 \pi B_s + 2\pi r \int B_r \, ds = 0 \quad \rightarrow \quad B_r = -\frac{r B_s'}{2}, \tag{3.9}$$

where the radial field is proportional to the longitudinal derivative of B_s.

For real solenoids, the longitudinal field $B_s(s)$ decreases by increasing the distance ξ from its center, depicted in Figure 3.2. The origin of the coordinate system is assumed to be in the middle of the solenoid and its optical axis is equal with the reference orbit. The field from a small coil element with length $d\xi$ acting on an arbitrary point on the s axis is

$$dB = \frac{\mu_0 \, I \, R^2 \pi \, n}{2\pi \left[R^2 + (s-\xi)^2\right]^{3/2}} d\xi, \tag{3.10}$$

when the solenoid has the length L and radius R [71]. The field strength can be further integrated over the angle

$$\begin{aligned} B_s(s) &= -\frac{\mu_0 n I}{2} \int_{\alpha_1}^{\alpha_2} \cos(\alpha) \, d\alpha \\ &= \frac{B_s}{2} \left[\frac{s + L/2}{\sqrt{R^2 + (s + L/2)^2}} - \frac{s - L/2}{\sqrt{R^2 + (s - L/2)^2}} \right]. \end{aligned} \tag{3.11}$$

Equipped with the knowledge of the solenoids' field dynamics, the next section will describe the particle's motion in such a field.

3.2 Single particle motion inside solenoids

For describing the track of a single particle inside a solenoid in this section, it is useful to apply cylindrical coordinates with unitary vectors

$$\hat{r} = \begin{pmatrix} \cos(\theta) \\ \sin(\theta) \\ 0 \end{pmatrix}, \qquad \hat{\theta} = \begin{pmatrix} -\sin(\theta) \\ \cos(\theta) \\ 0 \end{pmatrix}, \qquad \hat{s} = \begin{pmatrix} 0 \\ 0 \\ 1 \end{pmatrix}, \tag{3.12}$$

while the position of the particle r, its first and second time derivative can be expressed as

$$\begin{aligned}\vec{r} &= r\hat{r} + s\hat{s},\\ \dot{\vec{r}} &= \dot{r}\hat{r} + r\dot{\theta}\hat{\theta} + \dot{s}\hat{s},\\ \ddot{\vec{r}} &= \left(\ddot{r} - r\dot{\theta}^2\right)\hat{r} + \left(2\dot{r}\dot{\theta} + r\ddot{\theta}\right)\hat{\theta} + \ddot{s}\hat{s}.\end{aligned} \tag{3.13}$$

The force acting on the particle by the solenoid's magnetic field can be expressed as the Lorentz force in the cylindrical system

$$q\left(\dot{\vec{r}} \times \vec{B}\right) = \gamma m \ddot{\vec{r}}. \tag{3.14}$$

Setting the derivations (3.13) into the Lorentz equation (3.14), the force is following to

$$m\gamma \begin{pmatrix} \ddot{r} - r\dot{\theta}^2 \\ 2\dot{r}\dot{\theta} + r\ddot{\theta} \\ \ddot{s} \end{pmatrix} = q \begin{pmatrix} r\dot{\theta}B_s \\ -\left(\dot{s}rB_s'/2 + \dot{r}B_s\right) \\ \dot{r}\dot{\theta}rB_s'/2 \end{pmatrix}, \tag{3.15}$$

where the magnetic azimuthal component was assumed to be $B_\theta = 0$. The focusing strength can be derived by integrating the first line of equation (3.15) and yields to

$$\ddot{r} = -\frac{q^2 r B_s^2}{4(\gamma m)^2} \quad \rightarrow \quad r' = -\frac{q^2}{4}\int \frac{r B_s^2}{(\gamma m \dot{s})^2}\, ds, \tag{3.16}$$

where $\dot{\theta}$ can be derived by the second line of equation (3.15) and the time derivative exchanges by $\partial/\partial t = \dot{s}\,\partial/\partial s$. The focal length of a solenoid with length L and a field B_s is defined for a particle with a given momentum p as

$$\frac{1}{f} = kL = \frac{r'}{r} = \frac{q^2}{4}\int \frac{B_s^2}{p^2}\, ds, \tag{3.17}$$

following that the focusing strength of a solenoid scales to

$$k = \kappa^2 = \frac{q^2 B_s^2}{4p^2}. \tag{3.18}$$

In order to calculate the track of a single particle, the solenoid's environment has to be first separated into three parts. One is the area of the confined space of the solenoid itself. The other two are the entrance and the exit regions. Lets consider the case of a hard edge solenoid, which fringe field length is infinite small. Due to the radial field component, the particle experiences in the entrance of the solenoid an azimuthal

momentum kick, which can be expressed by the second component of equation (3.14)

$$\dot{p_\theta} = q\dot{s}B_r \quad \rightarrow \quad \dot{s}p'_\theta = -\frac{q\dot{s}rB'_s}{2}, \tag{3.19}$$

where it was assumed that the particle initially propagates only in longitudinal direction with velocity $\dot{s}$. Transforming the momentum kicks into trace space coordinates, they follow to

$$\begin{aligned} \Delta x' &= \frac{\Delta p_x}{p_s} = -\frac{p_\theta \sin(\theta)}{p_s} = \kappa y, \\ \Delta y' &= \frac{\Delta p_y}{p_s} = \frac{p_\theta \cos(\theta)}{p_s} = -\kappa x. \end{aligned} \tag{3.20}$$

In accelerator physics the particle propagation is described by means of in the so called transport matrices. In the fringe fields at the entrance and the exit of the solenoid, the propagation is described by

$$\mathbf{M}_{\text{entry}} = \begin{pmatrix} 1 & 0 & 0 & 0 \\ 0 & 1 & \kappa & 0 \\ 0 & 0 & 1 & 0 \\ -\kappa & 0 & 0 & 1 \end{pmatrix}, \qquad \mathbf{M}_{\text{exit}} = \begin{pmatrix} 1 & 0 & 0 & 0 \\ 0 & 1 & -\kappa & 0 \\ 0 & 0 & 1 & 0 \\ \kappa & 0 & 0 & 1 \end{pmatrix}. \tag{3.21}$$

Those matrices differ from each other by their opposite momentum kicks. For hard edge solenoids, the magnetic field in the body is constant and the particle is carrying out a circular motion in the transverse plane. Over the length L of the solenoid [69], the total rotation angle is

$$\theta = -\frac{qB_s}{p_s}L = -2\kappa L. \tag{3.22}$$

The transport matrix of the solenoid's body can be further expressed as

$$\mathbf{M}_{\text{body}} = \begin{pmatrix} 1 & \frac{L}{\theta}\sin(\theta) & 0 & -\frac{L}{\theta}(1-\cos(\theta)) \\ 0 & \cos(\theta) & 0 & -\sin(\theta) \\ 0 & \frac{L}{\theta}(1-\cos(\theta)) & 1 & \frac{L}{\theta}\sin(\theta) \\ 0 & \sin(\theta) & 0 & \cos(\theta). \end{pmatrix} \tag{3.23}$$

Finally, the solenoid matrix is the multiplication of the body and its fringe field transport matrices

$$\mathbf{M}_{\text{Sol}} = \mathbf{M}_{\text{exit}}\mathbf{M}_{\text{body}}\mathbf{M}_{\text{entry}} = \begin{pmatrix} C^2 & SC/\kappa & SC & S^2/\kappa \\ -\kappa SC & C^2 & -\kappa S^2 & SC \\ -SC & -S^2/\kappa & C^2 & SC/\kappa \\ \kappa S^2 & -SC & -\kappa SC & C^2 \end{pmatrix}, \tag{3.24}$$

with $C = \cos(\kappa L)$ and $S = \sin(\kappa L)$. It can be seen that the transport matrix of a solenoid couples the particle motion transversely, which has to be taken into account in future muon cooling simulations.

3.3 Transverse beam dynamics

In accelerator physics, the properties of an ensemble of particles are considered, because calculating the trajectory of each particle would be impractical. The sum of all tracks forms an envelope in a beam line, which can be described by specific parameters. Those depend on the optical elements and will be introduced in this section.

The optical functions are well defined in a circular accelerator due to its periodic boundary conditions. In such a ring, it is worth looking at the two-dimensional trace space of a single particle, while it passes through an arrangement of beam optical elements.

Evaluating the trace space coordinates (x, x') after each turn of the particle at a specific point s in the optical lattice, the occupied trace space of the particle forms to an ellipse-like shape. This is better known as the trace (phase) space ellipse and is illustrated in Figure 3.3. Particles starting with smaller initial trace space coordinates form ellipses which are within the one of the particle with a higher spatial and angular offset.

In beam dynamics, one chooses a particle, which elliptical surface describes the whole beam. Usually, the beam profile is assumed to be Gaussian and considers the standard deviations $(\sigma_x, \sigma_{x'})$ as the phase space limits of the beam. Equal calculations are valid for the (y, y') trace space. However, this section will generalize the 2-dimensional dynamics in (x, x') coordinates Since the optical elements of a ring are periodical, the particle equation of motion can be described by the so called Hill's equation [72]

$$x''(s) - k(s)x(s) = 0, \tag{3.25}$$

which differs from the harmonic oscillator by the non constant focusing strength $k(s)$. The Hill equation describes the oscillating motion inside the presence of strong focusing elements in a ring. Equation (3.25) can be solved by Floquet's theorem and follows to

$$x(s) = \sqrt{\epsilon_x}\sqrt{\beta_x(s)}\cos(\psi(s) + \phi), \tag{3.26}$$

which describes the transverse path of the particle along the reference orbit s. The so called beta or betatron function $\beta_x(s)$ is a function of the amplitude of the beam's oscillation and describes together with ϵ_x the beam size or the maximum amplitude $\sqrt{\epsilon_x \beta_x(s)}$ of the beam motion at any position s. The parameter $\psi(s)$ is the phase advance and ϕ its initial condition.

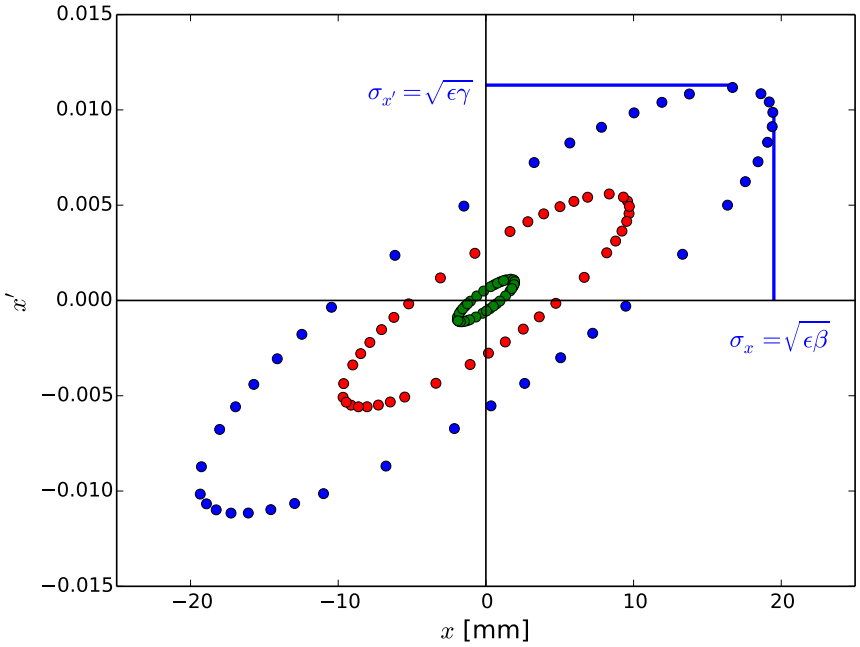

Figure 3.3: Particles orbiting a periodical beam optical structure and form at each point of s a trace space ellipse. Observing the blue ellipse it can be concluded, that this particle has the highest initial offset in angle and spread in comparison to the red an green motion. The maximum of x and x' defines for a Gaussian beam the rms values σ_x and $\sigma_{x'}$, which are functions of one beam parameter multiplied by ϵ.

The fist and second s depending derivatives of Hill's solutions are

$$x'(s) = \sqrt{\epsilon_x}\frac{\beta_x'(s)}{2\sqrt{\beta_x(s)}}\cos(\psi(s)-\phi) - \sqrt{\epsilon_x}\sqrt{\beta_x(s)}\psi'\sin(\psi(s)-\phi), \tag{3.27}$$

$$\begin{aligned} x''(s) = &\sqrt{\epsilon_x}\left(\frac{\beta_x''(s)}{2\sqrt{\beta_x(s)}} - \frac{(\beta_x'(s))^2}{4\sqrt{\beta_x(s)}^3} - \sqrt{\beta_x}(\psi'(s))^2\right)\cos(\psi(s)-\phi) \\ &- \sqrt{\epsilon_x}\left(\sqrt{\beta_x(s)}\psi''(s) + \frac{\beta_x'(s)}{\sqrt{\beta_x(s)}}\psi'(s)\right)\sin(\psi(s)-\phi). \end{aligned} \tag{3.28}$$

Inserting equation (3.26) and (3.28) into Hill's equation (3.25), the equation of motion is separated into a cosine and a sine term, which are fulfilling Hill's equation only when both are 0 [70]. The phase advance can be expressed by setting the sine term to zero following

$$\psi(s) = \int_{s_0}^{s_1}\frac{d\tilde{s}}{\beta_x(\tilde{s})}. \tag{3.29}$$

Setting the cosine term equals zero and and express ψ' with (3.29), a second order differential equation of the beta function can be expressed by

$$2\beta_x''(s)\beta_x(s) - \left(\beta_x'(s)\right)^2 + 4\beta_x^2(s)\kappa^2 - 4 = 0, \tag{3.30}$$

which is in this case the beam envelope equation of solenoidal fields. Lets further consider the first derivative of the Hill's solution by exchanging the cosine with $x(s)/\sqrt{\epsilon_x\beta_x(s)}$, which is

$$x'(s) = -\frac{\sqrt{\epsilon_x}}{\sqrt{\beta_x(s)}}\left(\alpha_x(s)\frac{x(s)}{\sqrt{\epsilon_x\beta_x(s)}} + \sin(\psi(s) - \phi)\right), \tag{3.31}$$

where a new beam parameter $\alpha(s)$ was introduced, namely

$$\alpha_x(s) = -\frac{\beta_x'(s)}{2} \tag{3.32}$$

which describes the skewness of the ellipse and is a kind of coupling between the motion of space and angle known as correlation. Bringing the x-depending term of equation (3.31) to the left side and further square the whole equation, the geometrical emittance can be expressed as an ellipse equation

$$\epsilon_x = \beta_x(s)x'^2(s) + 2\alpha_x(s)x(s)x'(s) + \gamma_x(s)x^2(s), \tag{3.33}$$

where the third beam parameter $\gamma_x(s)$ is defined as

$$\gamma_x(s) = \frac{1 + \alpha_x^2(s)}{\beta_x(s)}. \tag{3.34}$$

This geometrical emittance describes the beam ellipse in the trace space and by multiplying π it expresses the occupied area of the beam. Due to Liouville's theorem this trace space area remains to be constant along the beam line, but the shape of the ellipse is changing at each point of s. This is certainly true, but due to changes of p_s in a beam optical complex, the beam sizes changes due to relativistic contractions. To undergo this issue the geometrical emittance can be made Lorentz invariant by multiplying the Lorentz factors on it

$$\epsilon_{x,\mathrm{N}} = \beta\gamma\,\epsilon_x, \tag{3.35}$$

which is also called the normalized emittance and was already mentioned in chapter 1. The s depended parameter are known as Twiss parameters or also Courant-Snyder invariants [73] and describe the elliptical shape of the beam ellipse. In Figure 3.3 it is possible to express the beam sizes by means of the geometrical emittance and specific Twiss parameters.

Trace space coordinates transformation from a point s_0 to s_1 can be computed applying a single transfer matrix or even a lattice matrix $\mathbf{M}(s)$, which is the multiplication of

several transfer matrices, on an initial trace space vector

$$\begin{pmatrix} x_1 \\ x_1' \end{pmatrix} = \begin{pmatrix} c(s) & s(s) \\ c'(s) & s'(s) \end{pmatrix} \begin{pmatrix} x_0 \\ x_0' \end{pmatrix}, \tag{3.36}$$

where $\mathbf{M}(s)$ depends on sine $s(s)$ and cosine $c(s)$ like functions and their derivatives. By means of the inverse matrix $\mathbf{M}^{-1}$ it is possible to find the transfer matrix for the Twiss parameters, which scales to

$$\begin{pmatrix} \beta_1 \\ \alpha_1 \\ \gamma_1 \end{pmatrix} = \begin{pmatrix} c^2(s) & -2c(s)s(s) & s^2(s) \\ -c(s)c'(s) & c(s)s'(s) + c'(s)s(s) & -s(s)s'(s) \\ c'^2(s) & -2c'(s)s'(s) & s'^2(s) \end{pmatrix} \begin{pmatrix} \beta_0 \\ \alpha_0 \\ \gamma_0 \end{pmatrix}. \tag{3.37}$$

Since the introduction of the luminosity in equation (1.18), the normalized transverse emittance is considered as one main target parameter of a potential muon collider and this thesis will pay central attentions on that. This work will present later the performance of single particle tracks for the final cooling. It is therefore essentially to introduce a statistical technique for evaluating the emittance of an ensemble of particles.

3.4 Statistical emittance definition

The particle distribution of a beam can be described by its first central moment $\langle x \rangle$ or $\langle p_x \rangle$, which is the core's motion of a particle bunch and is also know as the mean value

$$\langle x \rangle = \frac{\sum_{i=0}^{N} x_i}{N}, \quad \langle p_x \rangle = \frac{\sum_{i=0}^{N} p_{x_i}}{N}. \tag{3.38}$$

The second central moments [74] of a beam distribution are defined as

$$\langle x^2 \rangle = \frac{\sum_{i=0}^{N} \left(x_i - \langle x \rangle\right)^2}{N}, \quad \langle p_x^2 \rangle = \frac{\sum_{i=0}^{N} \left(p_{x_i} - \langle p_x \rangle\right)^2}{N}. \tag{3.39}$$

If the core of a beam has a specific offset with respect to the origin of the ideal orbit, the mean value has also to be taken into account, like it was included in equations (3.39). In case of a Gaussian distribution the square root of the second moment yields to its standard deviation $\sigma_x = \sqrt{\langle x^2 \rangle}$ and $\sigma_{p_x} = \sqrt{\langle p_x^2 \rangle}$.

For evaluating the emittance of a beam, it is sufficient to calculate the surface area of the phase space, which is occupied by the particles and are lower equal to the rms limits (σ_x, σ_{p_x}). For a horizontal or vertical lying phase space ellipse, the surface area is the product of the semi major and semi minor axes and the geometrical emittance scales

to

$$\epsilon_x = \sqrt{\langle x^2 \rangle \langle p_x^2 \rangle}. \tag{3.40}$$

In case of a non-upright ellipse, the emittance calculation is not so trivial anymore. Therefore a rotating coordinate system $(\tilde{x}, \tilde{p}_x)$ can be introduced for a correlated phase space ellipse as illustrated in Figure 3.4. The transformation of a single particle in the roting frame follows

$$\begin{aligned} \tilde{x}_i &= |p_{x,i} \cos(\theta) - x_i \sin(\theta)|, \\ \tilde{p}_{x,i} &= |x_i \cos(\theta) + p_{x,i} \sin(\theta)|. \end{aligned} \tag{3.41}$$

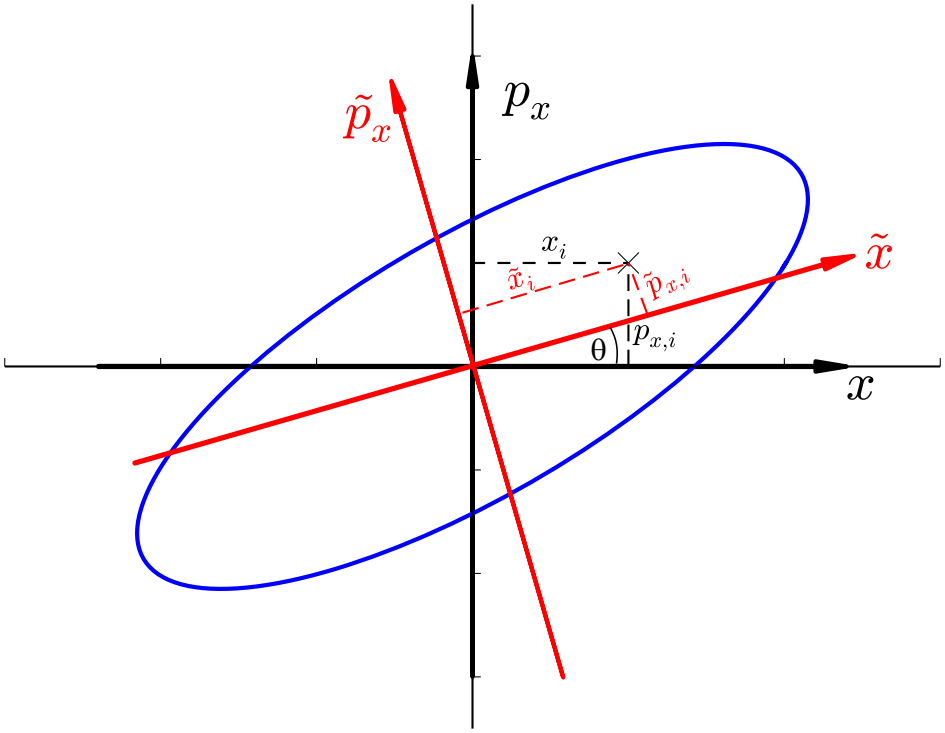

Figure 3.4: The surface area of a correlated phase-space ellipse can be calculated by means of a rotating system $(\tilde{x}, \tilde{p}_x)$.

Considering the rms value of the transformed momentum this would further scale to

$$\langle \tilde{p}_x^2 \rangle = \langle p_x^2 \rangle \cos^2(\theta) + \langle x^2 \rangle \sin^2(\theta) - 2\langle x p_x \rangle \sin(\theta) \cos(\theta). \tag{3.42}$$

This function reaches its minimum at a certain angle $\theta_{\min}$ [74], which can be evaluated by the derivative $\partial \langle \tilde{p}_x^2 \rangle / \partial \theta$ and follows to

$$\tan(2\theta_{\min}) = \frac{2\langle x p_x \rangle}{\langle x^2 \rangle - \langle p_x^2 \rangle}. \tag{3.43}$$

The next step is to rewrite equation (3.42) by means of some trigonometric changes to

$$\langle \tilde{p}_x^2 \rangle = \frac{1}{2}\langle p_x^2 \rangle + \frac{1}{2}\langle x^2 \rangle + \frac{1}{2}\left(\langle p_x^2 \rangle - \langle x^2 \rangle\right)\sin(2\theta) - 2\langle x p_x \rangle \sin(2\theta) \tag{3.44}$$

Inserting the minimum angle (3.43) into the equation above further yields to

$$\langle \tilde{p}_x^2 \rangle = \frac{1}{2}\left(\langle p_x^2 \rangle + \langle x^2 \rangle - 2\frac{\langle x p_x \rangle^2}{\sin^2(\theta_{\min})}\right). \tag{3.45}$$

The coordinate transformation by $\theta_{\min}$ of $\langle x^2 \rangle$ is following the same calculation technique, which was applied for evaluating $\langle \tilde{p}_x^2 \rangle$ and scales to

$$\langle \tilde{x}^2 \rangle = \frac{1}{2}\left(\langle p_x^2 \rangle + \langle x^2 \rangle + 2\frac{\langle x p_x \rangle}{\sin(\theta_{\min})}\right). \tag{3.46}$$

The rotation of the the minimum angle cancels the correlation in the new system and the geometrical emittance can be calculated by the square rooted product of equation (3.45) and (3.46), which is

$$\epsilon_x = \frac{1}{2}\sqrt{\langle x^2 \rangle + \langle p_x^2 \rangle + 2\langle x^2 \rangle \langle p_x^2 \rangle - 4\frac{\langle x p_x \rangle^2}{\sin^2(2\theta_{\min})}}. \tag{3.47}$$

By means of the identity $\sin(\arctan(x)) = x/\sqrt{1+x^2}$, the emittance finally scales to

$$\epsilon_x = \sqrt{\langle x^2 \rangle \langle p_x^2 \rangle - \langle x p_x \rangle^2}, \tag{3.48}$$

which is in turn of the Lorentz invariant case the normalized emittance

$$\epsilon_{x,\mathrm{N}} = \frac{1}{m_\mu c}\sqrt{\left\langle \left(x - \langle x \rangle\right)^2 \right\rangle \left\langle \left(p_x - \langle p_x \rangle\right)^2 \right\rangle - \left\langle \left(x - \langle x \rangle\right)\left(p_x - \langle p_x \rangle\right) \right\rangle^2}. \tag{3.49}$$

From the emittance evaluations it is possible to construct a certain sigma matrix $\mathbf{\Sigma}$ which includes the second moments and their correlation

$$\mathbf{\Sigma} = \begin{pmatrix} \langle x^2 \rangle & \langle x x' \rangle \\ \langle x' x \rangle & \langle x'^2 \rangle \end{pmatrix} = \begin{pmatrix} \epsilon\beta & -\epsilon\alpha \\ -\epsilon\alpha & \epsilon\gamma \end{pmatrix}, \tag{3.50}$$

where it was assumed that $\langle x x' \rangle = \langle x' x \rangle$. The geometrical emittance can be calculated by the square root of the sigma matrix's determinant $\sqrt{\det(\mathbf{\Sigma})}$. The ellipse equation (3.33) can be therefore reconstructed by

$$u^\top \mathbf{\Sigma}^{-1} u = \epsilon_x, \tag{3.51}$$

if $u = (x,\, x')^\top$ and the identity

$$\beta\gamma - \alpha^2 = 1 \tag{3.52}$$

is valid and agrees with equation (3.33). After introducing the theoretical background of the transverse beam dynamic and the single particle motion in a solenoid field, it is possible to apply these for describing the normalized emittance reduction of a muon beam by means of ionization cooling.

Chapter 4: Muon beam cooling

As it was already mentioned in this work, the divergence and the spread of the muon beam must be reduced after its creation as fast as possible. In accelerator physics, the reduction of beam sizes is usually denoted as cooling. Otherwise, the luminosity defined in equation (1.18) cannot reach the desired high level, thus new physics would be hard to explore.

There are several types of cooling techniques like electron cooling [1] and laser cooling [75]. However, these methods would not be suitable for muons, due to their several orders higher cooling time [76] compared with the muon lifetime. Stochastic cooling [77, 78] applied on muon beams had been studied, but seems to be technologically challenging [79].

Passing through the absorber, the muon beam loses momentum as well in transverse components as in the longitudinal direction by storing energy inside the material as shown in Figure 4.1. After the passage through the absorber, the lost energy will be restored by a re-acceleration but only in the longitudinal directions by means of RF cavities. Due to repeating passage through the absorber and RF cavities, the beam will be collimated, which is equalizing with an emittance reduction.

Nevertheless, because of multiple scattering effects appearing inside the absorber, it was suggested to place that in a strong focusing element. A high field solenoid seems to provide a suitable optic, since it focuses the beam in both transverse directions simultaneously described by the solenoid's transfer matrix (3.24). Considering a bunch of muons undergoing these last described processes, the muon beam will be reduced in its transverse emittance.

4.1 Final cooling cell structure

While in the beginning of this chapter the beam collimation was sketched by means of absorbers with RF systems in between, this section describes the role of high field solenoids for a final cooling cell. At first, it is useful to consider a single particle with

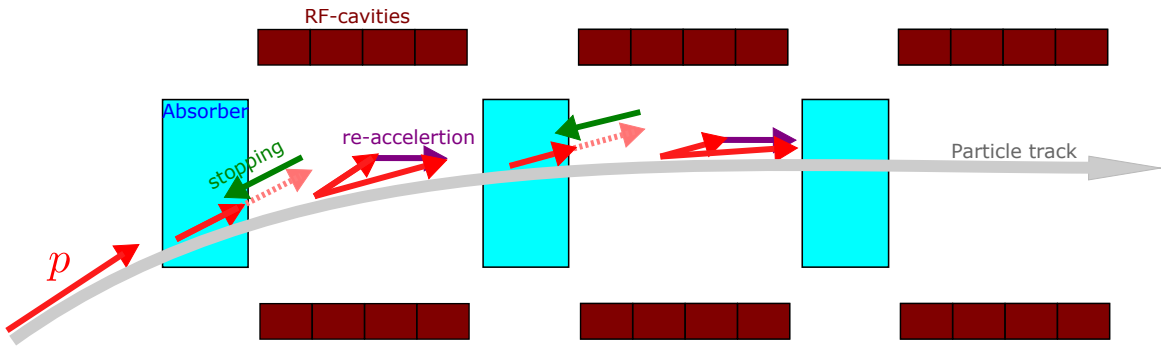

Figure 4.1: For reducing the divergence of a muon beam, its transverse momenta has to be decreased. Passing through low-Z materials followed by longitudinal re-acceleration periodically, the muon beam will be collimated which means a reduction of the transverse emittance.

an initial offset x_0 and momentum p. Propagating in a hard edge solenoid without any absorber inside, the particle's trajectory is a helix, due to the momentum kick at the solenoid's entrance described in matrix (3.24). An example is given in Figure 4.2 left, where a particle is performing a circular motion in the transverse plane, depicted as the blue line. The initial parameters are $p = 100\,\mathrm{MeV/c}$, $x_0 = 0.1\,\mathrm{m}$ and the field strength of the magnet is $5\,\mathrm{T}$.

The next step is to include a momentum loss per unit length inside the solenoid, which simulates in somewhat the stopping power of an absorber, which describes the energy loss of a particle inside matter and will be discussed more in detail in the next section. Performing the tracking of the particle in the transverse plane with a chosen loss of $0.01\,\mathrm{MeV/c}$ per $100\,\mu\mathrm{m}$ longitudinal propagation, the radius of this helix reduces continuously. Figure 4.2 shows this process in a red track and the particle spirals into a limited point, which is half of the initial offset.

One can incorrectly assume, that the geometrical emittance converts to zero, because it seems that the transverse momenta disappear totally by cooling the particles long enough. Assuming a continuous and slow beam stopping of a 4-dimensional distribution in the trace space with σ_x, σ_y, $\sigma_{x'}$ and $\sigma_{y'}$, the spatial spreads are limited by

$$\begin{aligned} \sigma_x &\longrightarrow \sigma_x/2 \equiv \sigma_{x_1}, \\ \sigma_y &\longrightarrow \sigma_y/2 \equiv \sigma_{y_1}, \end{aligned} \tag{4.1}$$

naively shown by the single particle track of Figure 4.2. While reducing the muons' velocity, the angular spread disappear, but due the couplings of the optics distributions

in the transverse plane are created:

$$\begin{aligned} \sigma_{x'} &\longrightarrow \sigma_{x'}/(2\kappa) \equiv \sigma_{y_2}, \\ \sigma_{y'} &\longrightarrow \sigma_{y'}/(2\kappa) \equiv \sigma_{x_2}, \end{aligned} \tag{4.2}$$

where κ is the focusing strength of the solenoid. In the case of a completely stopped muon bunch, the distributions would scale to

$$\begin{pmatrix} \tilde{\sigma}_x \\ \tilde{\sigma}_{x'} \\ \tilde{\sigma}_y \\ \tilde{\sigma}_{y'} \end{pmatrix} = \begin{pmatrix} \sqrt{\sigma_{x_1}^2 + \sigma_{x_2}^2} \\ 0 \\ \sqrt{\sigma_{y_1}^2 + \sigma_{y_2}^2} \\ 0 \end{pmatrix} \approx \begin{pmatrix} \sigma_{x_1}\left(1 + \frac{\sigma_{x_2}^2}{2\sigma_{x_1}^2}\right) \\ 0 \\ \sigma_{y_1}\left(1 + \frac{\sigma_{y_2}^2}{2\sigma_{y_1}^2}\right) \\ 0 \end{pmatrix}, \tag{4.3}$$

when $\sigma_{x_2,y_2} \ll \sigma_{x_1,y_1}$ is assumed. If the beam leaves the solenoid in the right before loosing its energy, the beam will experience a transverse force from the fringe field. Multiplying the momentum kick matrix (3.21) with the distribution vector (4.3), the emittance limitation in the x-plane yields

$$\epsilon_x = \frac{1}{4}\kappa\,\sigma_x\sigma_y + \frac{1}{8}\frac{\sigma_{y'}\sigma_y}{\kappa\sigma_x} + \frac{1}{8}\frac{\sigma_{x'}\sigma_x}{\kappa\sigma_y}, \tag{4.4}$$

and similar to the y-plane.

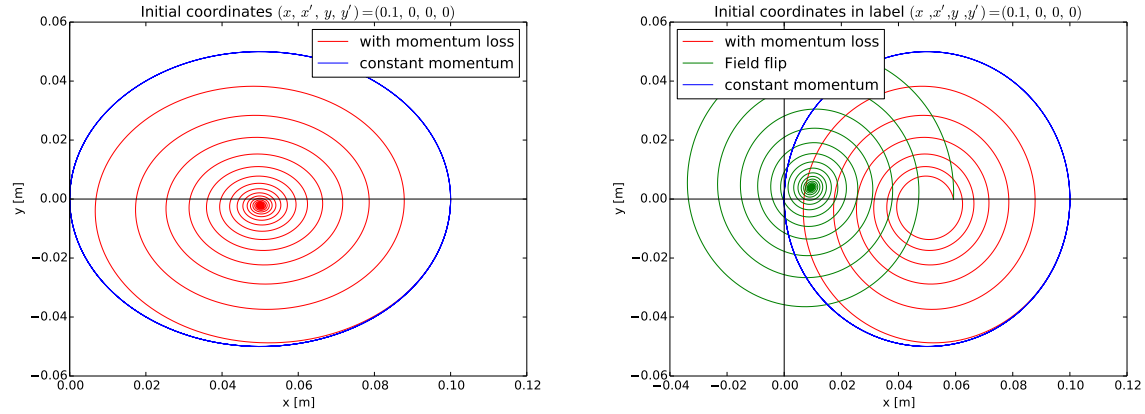

Figure 4.2: The plot on the **left** side illustrates the transverse particle motion inside a solenoid with (red line) and without (blue line) an absorber. For efficient emittance reduction it proves to be useful to set a field flipped solenoid after the first one. As illustrated in the **right** graph, the particle spirals next to the beam optical axis (green line).

To bring the emittance to zero, one possibility is, that the particle leaves the solenoid after $2\pi\, n$ of transverse turns, while n is an arbitrary integer number. Further, the particle enters a second solenoid with an absorber inside. It is assumed, that it has the same field strength as the one before, but its field arrows henceforth in the opposite direction. This is also referred to as a field flip. In Figure 4.2 it can be seen, that indeed in the second solenoid the particle spirals to the reference orbit, which is depicted as the green path in the plot. Therefore the emittance reductions follows to $\epsilon_x \to 0$.

To summarize, the final cooling cell structure contains a high field solenoid with a low-Z absorber material inside. After the beam deceleration, the particles have to be accelerated again by RF cavities. Finally, the muon bunch enters into a field flipped solenoid-absorber complex acting more efficient emittance reduction. The sketch in Figure 4.3 illustrates a typical final cooling cell structure based on solenoids. Before this work goes into detailed description of the beam dynamic in ionization cooling channel, it is useful to know how charged particles like muons behave inside matter, losing the energy by interacting with the absorber electrons.

Ionization cooling is only suitable for muons, because protons would scatter too much in that process and electrons would additionally loose energy due to bremsstrahlung [80]. Lets consider a muon beam with longitudinal and transverse momentum passing through an absorber. For avoiding high scattering effects, a low-Z material with low ordinary numbers seems to be suitable.

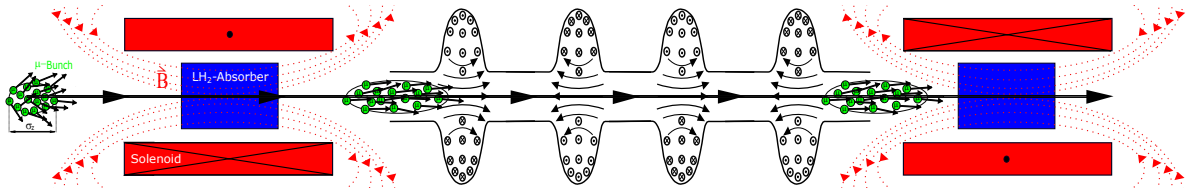

Figure 4.3: A single cell of the final cooling channel consists of two solenoids with absorbers inside, where the right one is field flipped respective to the first optic. In between, a series of RF cavities re-accelerates the beam after losing its momenta in the first solenoid.

4.2 Stopping power of absorbers

Traveling through low-Z material, muons are losing kinetic energy by radiative and collision processes, mostly caused with bounded or free electrons inside the absorber. These kind of inelastic interactions are known as ionizations and excitations, where the passing muon loses a proportion of its kinetic energy $\langle dE/ds \rangle$, also called energy loss or stopping power of the charged particle. For describing this phenomenon in a

mathematical approach, it is useful to consider the classical model introduced by N. Bohr [81, 82].

In the first one-dimensional assumption, a muon interacts with an electron inside the material and experiences a momentum loss expressed by

$$\Delta p = \int F\,dt = e\int E\,\frac{ds}{v}, \tag{4.5}$$

while the force F can be derived by an electric field E acting on the electron's charge e and the time element dt can be exchanged by ds/v. The minimum distance between a specific electron and the path of corresponding interacting muon is described by the impact parameter b, which is illustrated in Figure 4.4. Using the integral form of Gauss's law, where the Cartesian volume element dx^3 is replaced by means of the generalized Stokes theorem with the surface element $2\pi b\,ds$ in cylindrical coordinates, one gets

$$\int \nabla\vec{E}\,dx^3 \overset{\text{Stokes}}{=} 2\pi b\int E\,ds = \frac{Ze}{\epsilon_0} \;\Rightarrow\; e\int E\,\frac{dx}{v} = \frac{1}{4\pi\epsilon_0}\frac{2Ze^2}{bv}. \tag{4.6}$$

with the number of electrons Z within the integrated volume, equally with the already mentioned ordinary number. Further, the momentum can be expressed by means of equation (4.5) as

$$\Delta p = \frac{1}{4\pi\epsilon_0}\frac{2Ze}{bv}. \tag{4.7}$$

The energy transfer from the traveling muon to an electron depends on the impact

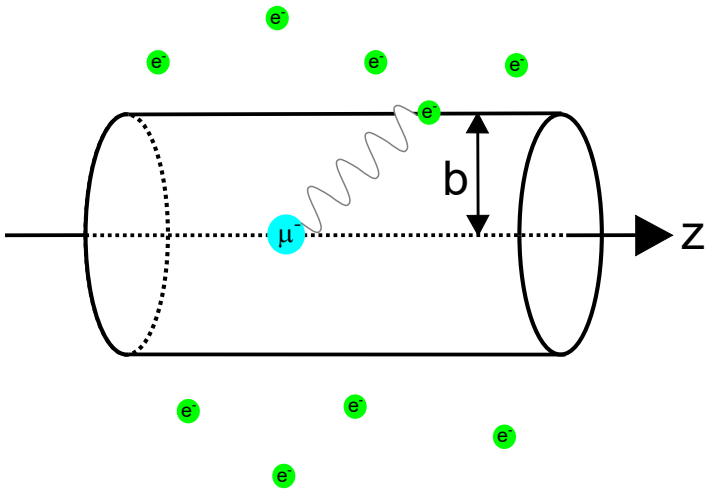

Figure 4.4: The impact parameter b can be described by the minimum distance between an electron and the path of a muon passing through the absorber.

parameter as follows

$$\Delta E(b) = \frac{(\Delta p)^2}{2m_\mathrm{e}} = \frac{1}{(4\pi\epsilon_0)^2}\frac{2Z^2e^4}{m_\mathrm{e}b^2v^2}. \tag{4.8}$$

Further, the loss of the muon's energy inside a volume element $dV = 2\pi b\,db\,ds$ of the absorber with its electron density n_e can be expressed as

$$-dE = \Delta E(b) n_\mathrm{e}\,dV = \frac{1}{4\pi\epsilon_0}\frac{4\pi Z^2e^4}{m_\mathrm{e}v^2} n_\mathrm{e}\frac{db}{b}ds, \tag{4.9}$$

where the final form of the energy loss per unit length inside a specific absorber is the integration from the minimum to the maximum impact parameter and takes the form

$$-\frac{dE}{ds} = \frac{1}{4\pi\epsilon_0}\frac{4\pi Z^2e^4}{m_\mathrm{e}v^2} n_\mathrm{e}\int_{b_\mathrm{min}}^{b_\mathrm{max}}\frac{db}{b}. \tag{4.10}$$

For the minimum impact parameter, head on collisions [83] can be taken into to account, where the electron moves with twice the velocity of the imping muon after colliding with a muon. By means of equation (4.8) the minimum impact parameter can be approached as

$$b_\mathrm{min} = \frac{1}{4\pi\epsilon_0}\frac{Ze^2}{m\gamma\beta^2c^2}, \tag{4.11}$$

while the maximum impact parameter is a function of the mean excitation potential I of a specific absorber and can be expressed as well by means of equation (4.8) as

$$b_\mathrm{max} = \frac{1}{4\pi\epsilon_0}\frac{Ze^2}{c\beta}\sqrt{\frac{2}{m_\mathrm{e}I}}. \tag{4.12}$$

This leads to the conclusion, that the excitation energy can be evaluated experimentally, demonstrating that it follows the law of $I\,[\mathrm{eV}] = 16\,\mathrm{Z}^{0.9}$ for low-Z materials [63]. A list of values of I for different absorbers, prepared specifically suitable for muon cooling simulations, can be found in P. Grubers review [86] or in the Particle Data Group [87]. Finally, the classical non-relativistic stopping power formula transforms to its final form by executing the integral of equation (4.10),

$$-\frac{dE}{ds} = \frac{1}{4\pi\epsilon_0}\frac{4\pi Z^2e^4}{m_\mathrm{e}v^2} n_\mathrm{e}\frac{1}{2}\ln\left(\frac{2m_\mathrm{e}c^2\gamma^2\beta^2}{I}\right). \tag{4.13}$$

For relativistic muons imping with high energies into an absorber, the classical approach can not be used anymore for further energy loss predictions. Therefore, H. Bethe and F. Bloch extended equation (4.13) by including relativistic and quantum mechanical

Table 4.1: Parameter summary of the Bethe-Bloch equation [84, 85].

Symbol	Definition	Units and/or Values
A	Atomic mass of the absorber	$\mathrm{g\ mol^{-1}}$
Z	Atomic number of the absorber	
N_A	Avogadro number	$6.022 \cdot 10^{23}\ \mathrm{mol^{-1}}$
a_0	Bohr radius $4\pi\epsilon_0\hbar^2/(m_\mathrm{e}e^2)$	$5.292 \cdot 10^{-11}\,\mathrm{m}$
r_e	Classical electron radius $e^2/4\pi\epsilon_0 m_\mathrm{e}c^2$	2.817 fm
$m_\mathrm{e}c^2$	Electron mass	0.511 MeV
e	Elementary charge	$1.602 \cdot 10^{-19}\,\mathrm{C}$
α	Fine structure constant $e^2/4\pi\epsilon_0\hbar c$	1/137.036
$m_\mu c^2$	Incident muon mass	105.658 MeV
ϵ_0	Vacuum permittivity	$8.854 \cdot 10^{-12}\,\mathrm{F\,m^{-1}}$
K	$4\pi N_\mathrm{A} r_\mathrm{e}^2 m_\mu c^2$	$0.307\ \mathrm{MeV\ g^{-1}cm^2}$

approaches, leading to the derivation of the well known Bethe-Bloch formula [88–90],

$$-\left\langle \frac{\partial E}{\partial s} \right\rangle = K\frac{Z}{A}\frac{1}{\beta^2}\left[\frac{1}{2}\ln\left(\frac{2m_\mathrm{e}c^2\beta^2\gamma^2 T_\mathrm{max}}{I^2}\right) - \beta^2 - \frac{\delta(\beta\gamma)}{2}\right], \tag{4.14}$$

where T_max describes the kinetic energy of an electron with mass m_e after a head-on collision with a relativistic muon with mass m_μ, which can be described by

$$T_\mathrm{max} = \frac{2m_\mathrm{e}c^2\beta^2\gamma^2}{1 + 2\gamma m_\mathrm{e}/m_\mu + (m_\mathrm{e}/m_\mu)^2}. \tag{4.15}$$

The letter A stands for the atomic number and K is composed on a couple of constants defined in table 4.1. In equation (4.14) the energy depended density term $\delta(\beta\gamma)$ comes from the polarization effect of the media, which will be relevant for considering muon energies above 1 GeV [85]. A full list of the used parameters for the last derivations is provided in Table 4.1.

Bear in mind, that the unit of the stopping power in equation (4.13) and (4.14) is $\mathrm{MeV\,g^{-1}\,cm^2}$, which is also known as the stopping cross section. This can be changed into $\mathrm{MeV\,cm^{-1}}$ multiplying by the appropriate density $\rho\,[\mathrm{g\,cm^{-3}}]$ [87]. The Bethe-Bloch formula is a good approach to describe the energy loss of charged particles due to electron stopping. Especially for muons, this law is valid for the kinetic energy in the range between 5 MeV and 100 GeV.

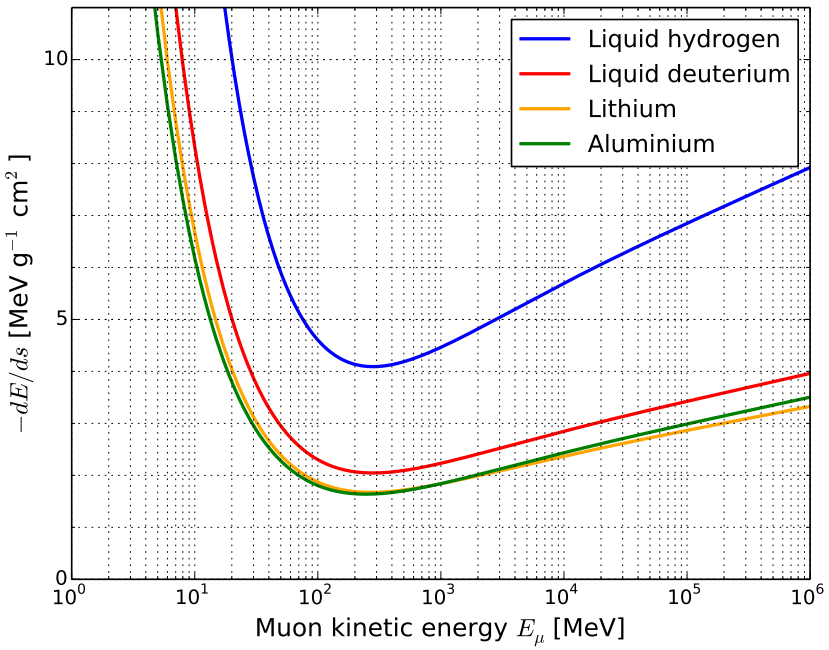

Figure 4.5: The Bethe-Bloch formula describes the electronic stopping of charged particles inside a certain absorber material in the range of some MeV to several GeV. This graph illustrates the stopping cross section of muons inside several elements. Remarkable is the curve of liquid hydrogen, which will be ideally suited for future muon cooling systems. The density factor is not included in this plot.

Below or above this range other theories have to be taken into account which behave completely different than the Bethe-Bloch estimation, such as the Lindhard-Scharff model [90], which describes the energy loss of charged particles in the keV range, where positive and negative muons do not behave equally anymore. E.g. this would be used for frictional cooling [91], which is not foreseen in the final cooling scheme, since relativistic time dilatation would be reduced, hence muons would decay faster in the laboratory system and lowering the luminosity (1.18) at the collision point in the collider ring.

To get some impressions, how equation (4.14) behaves, Figure 4.5 illustrates its function without including any density effects. For a final muon cooling scheme, the energy range is small enough and therefore the density term of equation (4.14) can be neglected.

It is noticeable, that the stopping power for muons inside liquid hydrogen is quite high in comparison to other elements. In the past studies, muon cooling simulations were performed with liquid hydrogen, lithium or even with lithium hydrate. However Figure 4.5 demonstrates, that the shape of lithium is similar to aluminium.

Nevertheless, high-Z elements have higher atomic masses and can lead to higher scattering angles. Therefore, elements with higher Z than lithium are not be taken into account for further muon cooling simulations.

4.3 Transverse muon ionization cooling

If the derivative respective to the reference orbit s is carried out, two terms appear

$$\frac{d}{ds}\epsilon_{\perp,\mathrm{N}} = \epsilon_{\perp}\frac{d(\beta\gamma)}{ds} + \beta\gamma\frac{d\epsilon_{\perp}}{ds}. \tag{4.16}$$

with $\perp = x, y$. The first term of equation (4.16) contains the derivative of both Lorentz factors, which can be expressed by applying relativistic kinematics to

$$\frac{d(\beta\gamma)}{ds} = \frac{1}{mc^2}\frac{d(pc)}{ds} = \frac{1}{mc^2}\frac{d}{ds}\sqrt{E^2 - m^2c^4} = \frac{1}{\beta \cdot mc^2}\frac{dE}{ds}. \tag{4.17}$$

The second term is not so trivial to express and comes from few approximations. The sigma matrix (3.50) was introduced in chapter 3 and the differentiation of the geometrical emittance therefore results to

$$\frac{d\epsilon_{\perp}}{ds} = \frac{d}{ds}\sqrt{\det \boldsymbol{\Sigma}} = \frac{1}{2\epsilon_{\perp}}\left(\sigma_{x'}^2\frac{d\sigma_x^2}{ds} + \sigma_x^2\frac{d\sigma_{x'}^2}{ds} - 2\langle xx'\rangle\frac{d\langle xx'\rangle}{ds}\right). \tag{4.18}$$

Now one has to make a few assumptions, such as the beam being inside an absorber surrounded by a solenoid. Its interior is embedded with a very strong and nearly homogeneous magnetic field (several T) in the longitudinal direction. For simplification, it is assumed that the beam is already matched with the solenoid's machine ellipse. This means also, that the beam envelope has the shape of a waist through the hole solenoid.

From the previous chapter 3 it is clear, that the beam waist is represented as a upright trace space ellipse. Thus, the third term, which expresses the changes of the correlation effects in equation (4.18) is canceled. For strong focusing, the growth of the transverse dimension can be neglected [92], thus the second term in equation (4.18) can be assumed to be zero.

The only term left in the equation (4.18) is the change in the transverse angular distribution, where $\sigma_{x'}^2$ is an expression of many small squared angle deflections of the muon inside the absorber caused by Coulomb scattering described by Rutherford's cross section [93]. These multiple scattering angles are following a Gaussian distribution, but due to hard scattering with nuclei, the angle distribution has a further non-Gaussian tail. This multiple scattering approximation is described by Moliére's theory [94] and

further extended by B. Rossi and K. Greisen [95]. The second moment of the the muon beam can be described as [96]

$$\langle x'^2 \rangle = \left[\frac{13.6[\mathrm{MeV}]}{\beta cp} \sqrt{\frac{s}{L_\mathrm{R}}} \left[1 + 0.038 \ln\left(\frac{s}{\beta^2 L_\mathrm{R}} \right) \right] \right]^2 \approx \frac{(13.6[\mathrm{MeV}])^2}{\beta^2 p^2 c^2} \frac{s}{L_\mathrm{R}}, \tag{4.19}$$

where s also expresses the absorber thickness and L_R is the absorber's depended radiation length. The expression (4.19) is inserted into the remaining second term of equation (4.18). Tanking into account the trace space spread $\sigma_x = \sqrt{\beta_\perp \epsilon_\perp}$ and $\sigma_{x'} = \sqrt{\epsilon_\perp / \beta_\perp}$ for an upright ellipse, one obtains

$$\frac{d\epsilon_\perp}{ds} = \sigma_x^2 \frac{1}{2\epsilon_\perp} \frac{d\langle x'^2 \rangle}{ds} = \frac{\beta_\perp (13.6[\mathrm{MeV}])^2}{2\beta^2 p^2 c^2 L_\mathrm{R}}. \tag{4.20}$$

Finally, the expressions (4.17) and (4.20) can be inserted into equation (4.16) and one gets the well known ionization cooling formula

$$\frac{d\epsilon_{\perp,\mathrm{N}}}{ds} = -\frac{\epsilon_{\perp,\mathrm{N}}}{E\beta^2} \left\langle \frac{\partial E}{\partial s} \right\rangle + \frac{\beta_\perp (13.6[\mathrm{MeV}])^2}{2\beta^3 E m c^2 L_\mathrm{R}} = \text{cooling} + \text{heating}, \tag{4.21}$$

first derived by D. Neuffer [80]. The first term describes the cooling of the muon beam and the second term describes the heating due to scattering effects of muons with the absorber's nuclei. From equation (4.17) the derived energy can be identified as the the energy loss based on the Bethe-Bloch formula (4.14). Both terms depends on specific absorber parameters, some potential candidates for ionization cooling are summarized in the table 4.2.

Table 4.2: Absorber specific parameter list [87].

Parameter	Symbol [Units]	liquid H_2	liquid D_2	liquid He	Li
Mean ionization	I [eV]	21.8	21.8	41.8	40.0
Atomic ratio	Z/A	1	0.5	0.5	0.43
Radiation length	L_R [g cm^{-2}]	63.4	125.98	94.32	82.77
Density	ρ [g cm^{-3}]	0.07080	0.1638	0.1249	0.5340

The betatron function can be estimated by means of equation (3.30). When correlation effects are negligible, the derivatives of the beta function are zero and the envelope equation reduces to $\beta_\perp^2 \kappa^2 = 1$. Therefore, a final expression for a beta function matched to a given solenoid scales to

$$\beta_\perp[\mu\mathrm{m}] = \frac{2p[\mathrm{MeV/c}]}{c \cdot B_s[\mathrm{T}]} 10^{12}. \tag{4.22}$$

The betatron function was expressed in μm, because the emittance in the final cooling simulations is usually expressed in this units. The heating term in equation (4.21) contains the unit MeV, therefore the momentum in (4.22) is expressed in MeV/c.

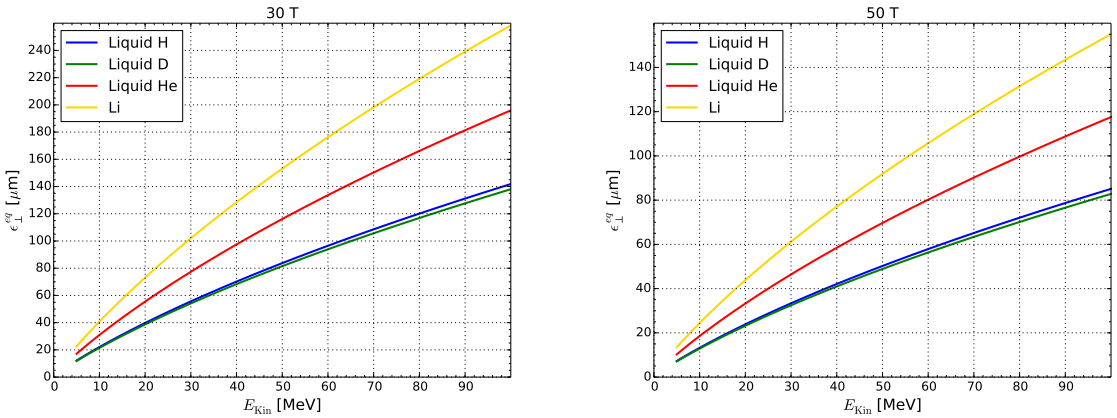

Figure 4.6: These plots show the equilibrium emittance of liquid hydrogen, liquid deuterium, liquid helium and lithium at 30 and 50 T. Cooling can be achieved if the initial normalized emittance is above the equilibrium emittance. Otherwise the beam would be heated up.

Since the change of the normalized transverse emittance in the absorber depends on the instantaneous variables E and $\epsilon_{\perp,\mathrm{N}}$, it is useful to know how cooling and heating terms change in response to these two free parameters. For this purpose, the limit values are determined at which cooling and heating compensate each other. Equation (4.21) is set to zero and further expressed in terms of $\epsilon_{\perp,\mathrm{N}}$ resulting to an expression known as the equilibriums emittance

$$\epsilon_\perp^{\mathrm{eq}} = \frac{\beta_\perp (13.6[\mathrm{MeV}])^2}{2\beta mc^2 L_\mathrm{R} \left\langle \frac{\partial E}{\partial s} \right\rangle}. \tag{4.23}$$

In the Figure 4.6, several $\epsilon_\perp^{\mathrm{eq}}$ have been considered as a function of kinetic energy, which are shown graphically for different high magnetic fields and absorber materials. It has to mentioned that the graphs behave differently compared to the previous final cooling study [37]. For a dominating cooling term in equation (4.21), it must be ensured that the initial normalized emittance is higher than the corresponding equilibrium emittance.

For the final cooling design, the minimum requirements for the beam energy and field strength can be found by means of formula (4.23). Assuming perfect beam parameter matching conditions, Figure 4.7 shows the behavior of the magnetic field, B, according to the beam's kinetic energy E_Kin at different equilibrium emittances. For example, with a strength of 30 T for the last solenoid in the final cooling channel, the kinetic beam

energy has to be lower than approximately 12 MeV to achieve the target normalized transverse emittance of $\epsilon_{\perp,\mathrm{N}} = 25\,\mu$m [36].

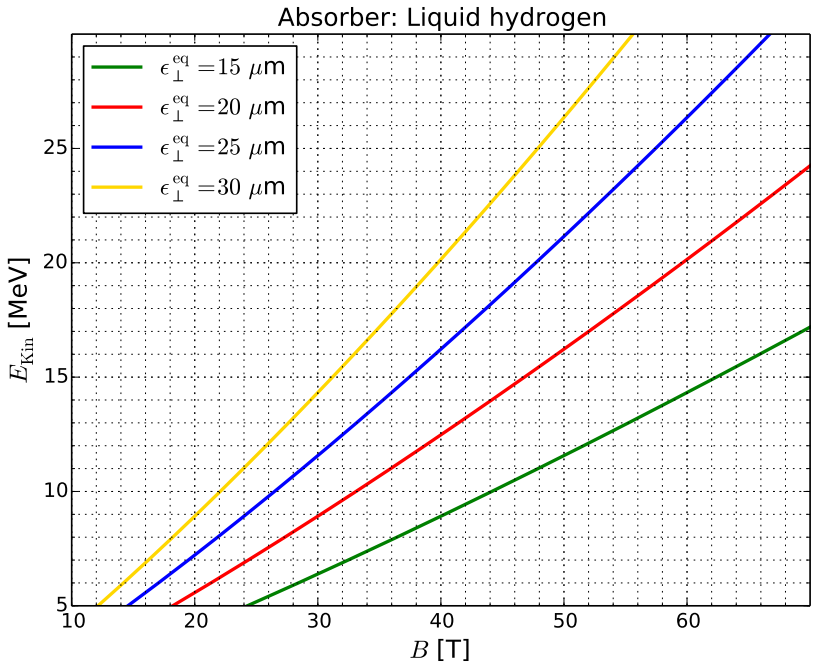

Figure 4.7: Field strength and beam energy requirements for the final cooling design can be estimated by using the equilibrium emittance $\epsilon_\perp^{\mathrm{eq}}$.

So far the impact of ionization cooling on the transverse emittance was well discussed, the behavior of the longitudinal emittance's changes of a beam will be briefly introduced in this section. In general, the longitudinal emittance ϵ_{L}, in the uncorrelated case, is the product of the bunch length σ_z and the the relative momentum spread σ_δ. Multiplied by the Lorentz factors, this parameters scale to the normalized longitudinal emittance defined as

$$\epsilon_{\mathrm{L,N}} = \beta\gamma\,\sigma_z\sigma_\delta = \beta\gamma\,\epsilon_{\mathrm{L}}. \tag{4.24}$$

Its change caused by an absorber can be derived by the same technique as it was applied to the transverse emittance change before in equation (4.18) and approximates to

$$\frac{d}{ds}\epsilon_{\mathrm{L,N}} \approx -\epsilon_{\mathrm{L,N}}\frac{d}{dE}\left\langle\frac{\partial E}{\partial s}\right\rangle. \tag{4.25}$$

As it can be seen, the longitudinal emittance change depends on the slope of the Bethe-Bloch function $\langle\partial E/\partial s\rangle$ and results to positive values for kinetic beam energies above 200-300 MeV (absorber depended), but negative below this range. Nevertheless, in order

to maximize transverse emittance reductions, only kinetic energies of about 100 MeV will be considered and leads to increase of the normalized longitudinal emittance.

Additionally, muons penetrating through the absorber are deflected by Coulomb scattering at random points. Their energy loss is stochastic and can be described by the so called straggling distribution function [92, 97, 98]. This contributes to a further heating term in the formula (4.25) and increases the longitudinal emittance in the final cooling sector more. However, this thesis deals exclusively with the transverse emittance reduction, since it has a higher priority, due to the capability to shrink the size of the accelerator and of the collider ring according to the beam width obtained with a reduced transverse emittance.

4.4 Simulation tool for ionization cooling

Simulation studies on ionization cooling with muons require a three-dimensional tracking code. The decay of muons and the interaction between these unstable particles with matter have to be taken into account. The required program must include energy losses, multiple scattering effects and momentum straggling. In addition, magnetic field maps on the particle tracks have to be created, which satisfy the beam optics requirements for the final cooling cell and have to be consistent with Maxwell's equations.

For such requirements, two simulation codes can be considered for ionization cooling studies. One option is the usage of a `G4BEAMLINE`, which is based on the `GEANT4` code [99]. This simulation tool was used for the previous final cooling study during the MAP collaboration [37]. Another existing code is a `FORTRAN77` based simulation framework, which is called `ICOOL` created by R. Fernow [100] at the Brookhaven National Laboratory. In the past couple of decades, only a few of the published ionization cooling studies have been performed this program. Therefore it was decided especially for this thesis to get familiar with `ICOOL` and execute simulation test, which will be further verified against theoretical models.

`ICOOL` was specifically developed for the purpose of designing muon colliders and neutrino factories. Installing `ICOOL` on a `LINUX` or `macOS` based operating system, one option are the following command lines :

```
1 $ wget --no-check-certificate https://www.cap.bnl.gov/ICOOL/icool-332.
      zip
2 $ unzip icool-332.zip
3 $ make
```

The first command downloads the `ICOOL` package, while the last one compiles the program. A remark at the edge, this study used `ICOOL-331.1` for any special reason,

which is almost identical with the newest version. To perform beam tracking in ICOOL, the command file for001.dat has to be set up, which structure contains [101]

- Simulation control variables,
- Beam definitions,
- Muon-absorber interaction and
- Tracing definitions.

The simulation is then to be executed from the command line:

```
$ ../icool
```

It the next chapters the tests with ICOOL will be presented and the beam parameter methods fo analyzing will be introduced. The 6-dimensional coordinates of each muon will be saved in a file called for009.dat on specific positions at the reference orbit s. The task is therefore to perform a suitable statistical analyzes code for evaluating the normalized emittance. Finally, the first results of muon beam cooling with different absorber materials inside high magnetic fields will be presented in section 6.2.

Chapter 5: ICOOL simulation tests

As it was already mentioned before, ICOOL is not a commonly used standard program for beam dynamic studies. However, it was suggested to perform some important tests for checking the program's functionality for future beam cooling simulations. In this chapter, the main target is to analyze the scatter distribution of muons with various absorber materials and further compare them with existing analytical models. On this occasion, this work took the opportunity to integrate and test liquid deuterium in ICOOL, which was never foreseen as ionization cooling target before. In the last section of this chapter, a strategy will be presented to analyze the beam parameters obtained form ICOOL. Since solenoids couple the transverse beam dynamics, a special statistical decoupling mechanism will be applied for evaluating the beta function and the beam correlation with the theory introduced in chapter 3.

5.1 Scattering simulations of high-Z materials

Tests of multiple scattering events caused by high-Z elements play also an essential role in the field of ionization cooling. For the confinement of liquid absorbers, thin metallic layers will be used. After cooling the emittance in liquid absorbers, the beam has to penetrate through that confinement layer at least. Scattering effects and emittance changes in high-Z materials has to be also considered in the muon collider study. For minimizing multiple scatterings, it is suggested to test Be and Al, because they are high up in the periodic table and are therefore metals with low densities.

First experiments with muon ionization cooling were performed at the international Muon Ionization Cooling Experiment (MICE) using liquid hydrogen, where $\sim 300\,\mu$m thick Al walls were used for the absorber confinement [102]. Those barriers are denoted as windows in the muon collider community. At MICE they were made out of one primary and a second safety Al window with a thin vacuum gap in between [103].

Concerning Be: on one hand, thin Be windows can also be considered since it is used for separating RF cavities in the cooling channel [104]. On the other hand, this element

is carcinogenic due to its toxic properties against human bodies. Engineering progresses on Be window constructions will seem to be a challenge in the near future.

For testing the scattering effects with ICOOL simulations, 10^4 muons were generated. They initial longitudinal momentum was set at $47\,\mathrm{MeV/c}$ ($E_{\mathrm{Kin}} \approx 10\,\mathrm{MeV}$), which is within the momentum range, where the particles leave the absorber and therefore passing further through the metallic window. For the simulation, momentum and spatial spreads in each direction were excluded, for maintaining a pure parallel and mono-energetic beam. Penetrating through the absorber, the divergence of the beam can be tracked with ICOOL and the calculation on the muons' rms scattering angle can be statistically executed.

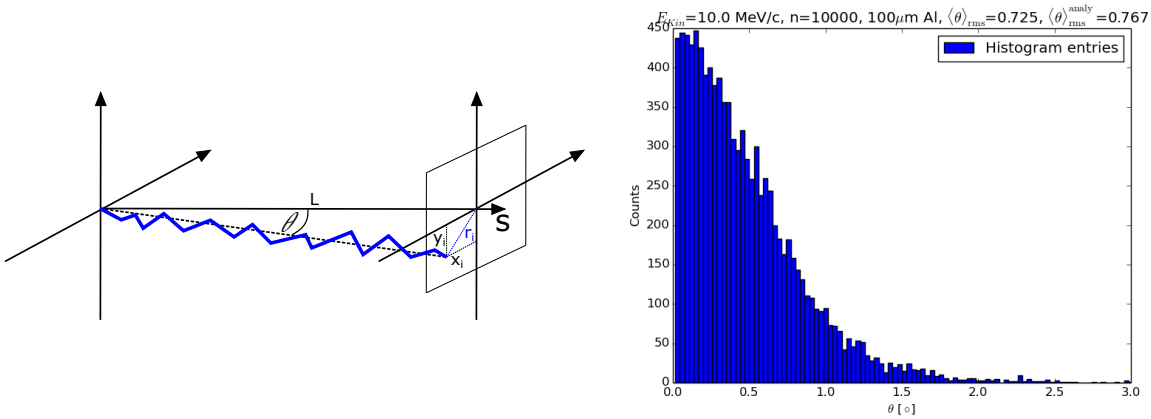

Figure 5.1: On the **left** side, a particle penetrates an absorber with length L and its trajectory is perturbed from multiple deflections. Its angle can be calculated by means of the muon's initial and end position. The histogram on the **right** side exhibits the Gaussian shape of the angle distribution with a characteristic non-Gaussian tail.

In the program, the particle tracking step size for the following ICOOL job was set at $1\,\mu$m. The reason for this was that the absorbers thickness varies from 20 to 1000 μm. Such very thin windows are worth to investigate, since a $6\,\mu$m aluminised mylar was already used for liquid hydrogen confinements for spallation reaction experiments [105].

Several multiple scatter models are available in ICOOL, but especially for this study the so called Fano-model was applied [101]. Under this program setting, ICOOL simulates multiple small angle deflections caused by Coulomb scattering, which depends on the absorber material. The net scattering angles of the muons follows a Gaussian distribution. In addition, rare hard scattering effects (muon-nucleus collisions) cause a non-Gaussian characteristic tail in the angle distribution.

Evaluating the rms scatter angle, the angle of every single muon at the end of the absorber has to be observed. It has to be ensured, that only muons are included, since

ICOOL counts also electrons created by muon decays in the program's output file. The lighter electrons would deflect inside the absorber much stronger, which would distort the total muon rms scatter angle. ICOOL has the feature to switch off the muon decay, which can sortout the problem for the calculation.

By means of a specific absorber length L the angle of each muon can be calculated in the x-plane with

$$\theta_i = \arctan(x_i/L). \tag{5.1}$$

For verifying the calculation, the sketch in Figure 5.1 on the left side can be helpful. Sorting the evaluated scatter angles into a histogram, the distribution can be determined, where one example is illustrated with a 100 μm thick Al absorber in the right plot of Figure 5.1. In this histogram, also the characteristic tail in the high angle range can be confirmed.

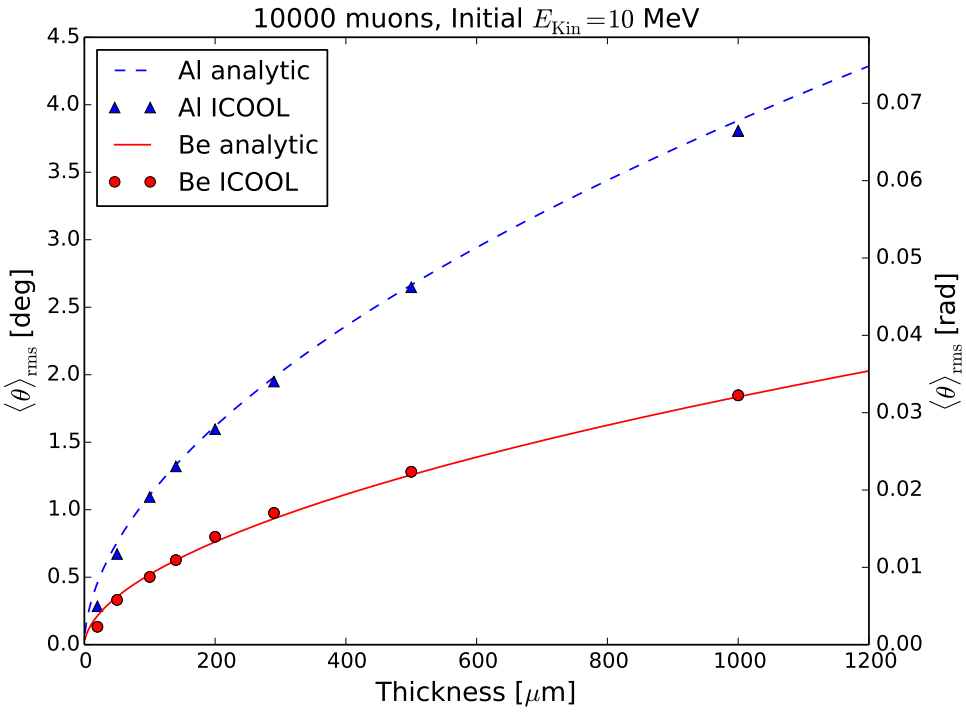

Figure 5.2: The rms angles for different window thicknesses calculated by ICOOL agree with the analytical model from the PDG. The triangles in blue illustrates the simulations through Al, while the red dots are the ones for Be.

For certain absorber lengths, the rms scatter angle

$$\langle\theta_{\mathrm{ICOOL}}\rangle = \frac{\sqrt{\sum_{i=0}^{n}\theta_i^2}}{n}. \tag{5.2}$$

can be compared with equation (4.19), suggested from the PDG [63]. The comparison is illustrated in Figure 5.2 and it seems that scattering at low energies and thin high-Z materials follows the analytical model in a good agreement.

5.2 Liquid hydrogen and deuterium scattering analyses

Due to multiple scattering events, only a few low-Z elements come into to account for ionization cooling [103, 106]. These absorbers would be H_2 and He both in a liquid state, or solid Li. However, during the past, the isotope deuterium has never been considered as a possible absorber candidate for ionization cooling. This common isotope can be extracted from heavy water, which is for example used in nuclear power plants.

Deuterium has one additional neutron more compared to hydrogen, and has in a liquid state a radiation length approximately twice the one of liquid hydrogen (table 4.2). Comparing the equilibrium emittance in Figure 4.6, it can be realized that analyzing liquid deuterium leads to slightly lower $\epsilon_{\perp}^{\mathrm{eq}}$ compared to liquid hydrogen. Following that, the cooling efficiency could be improved by using this isotopic configuration of hydrogen.

The next step is to implement this proposed material in `ICOOL`. Ten material specific parameters were added into the `ICOOL` code (`icool.for`), which are the ordinary and atomic numbers, its density and the seven deuterium specific Sternheimer coefficients taken from the PDG [87].

For testing the functionality of liquid deuterium with `ICOOL`, investigating the rms scatter angle was suggested again like in the previous section. To get closer to the final cooling conditions, the absorber length ranges from 20 mm to 1 m and a beam with 10^4 muons was generated at $p_s = 176.4\,\mathrm{MeV/c}$ ($E_{\mathrm{Kin}} \approx 100\,\mathrm{MeV}$) without any spatial or momentum spreads. The particle tracking step size for this test were set at 1 mm for saving computation time.

Due to low probability of hard scattering events in liquid deuterium, no angular limitations were suggested for calculating the rms scatter angle. Additionally, a second test run was performed with liquid hydrogen, to compare those almost similar materials. Both simulations were contrasted with the corresponding analytical prediction (4.19) and then illustrated in Figure 5.3.

As expected, the scattering angle of liquid deuterium is slightly higher compared to liquid hydrogen, because of the lower radiation length. Figure 5.3 shows, that both simulations are following the shape of the theoretical prediction, but do not fit exactly

with predicted values. It can be assumed that the analytical model reaches its limits for long absorbers and higher imping energies.

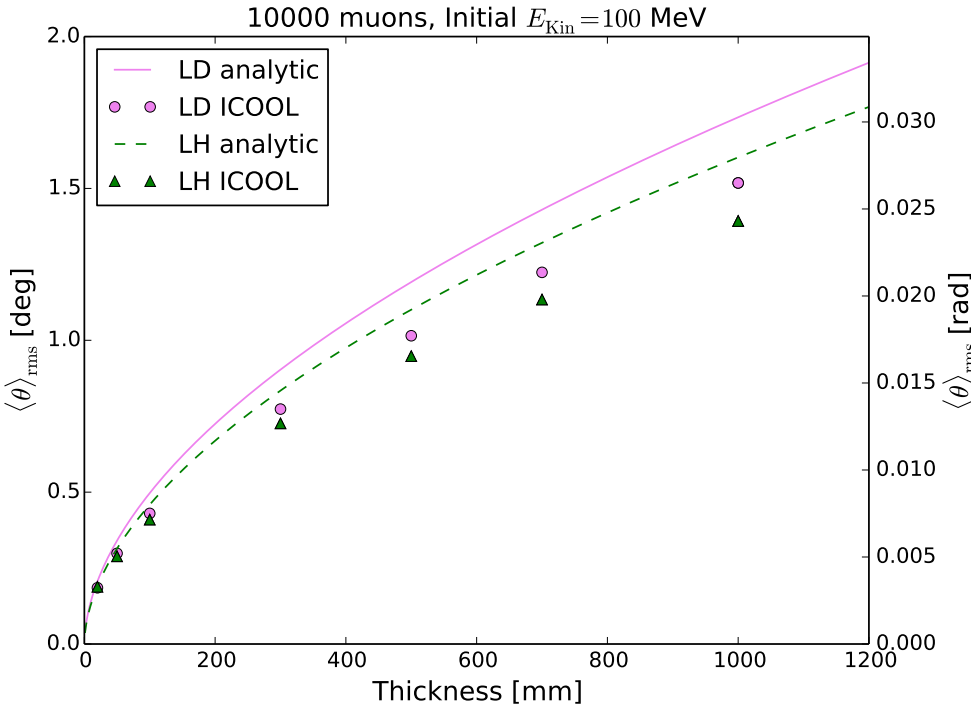

Figure 5.3: This graph compares the calculated rms angles of liquid hydrogen (triangles) and liquid deuterium (dots) from `ICOOL` with the PDG's analytical model.

5.3 Parameter decoupling by means of rotations

Since the transverse coordinates are coupled in a solenoid, the emittance can not be easily calculated by the description of section 3.4. One way for determining them is to transform the particle coordinates into a rotating system. The rotation causes a decoupling of the off-diagonal sub-matrices in a 4-dimensional transverse sigma matrix $\mathbf{\Sigma}^{4\mathrm{D}}$ and the beam parameter calculations in the (x, p_x) and (y, p_y) plane can be done separately.

For calculating the rotation angle, the second line of equation (3.15) has to be taken into account and can be rewritten as

$$\frac{m\gamma}{r}\frac{\partial}{\partial t}\left(r^2\dot{\theta}\right) = \frac{-q}{2r}\frac{\partial}{\partial t}\left(r^2 B_z\right). \tag{5.3}$$

Subsequently, the time derivatives cancel themselves out and the rotation angle can be expressed as

$$\theta_{\mathrm{L}} = -q \int \frac{B_s}{2p_s}\, ds, \tag{5.4}$$

which is better known as the Larmor angle. This rotation is not only depending on the magnetic field of the solenoid and the longitudinal momentum of the particle, but also its axial position of the reference particle plays a crucial role.

Following a particle with an initial vertical y-offset and entering a solenoid with a longitudinal momentum p_z, it performs a helical motion in the (x, y, s) space. This circulation passes through the initial position of the particle and a point on the beam optical axis s periodically, which is illustrated in Figure 5.4. A θ_{L} depended rotating coordinate system $(\tilde{x}, \tilde{y})$ depicted in red in Figure 5.4 shows, that the particle performs only an oscillation on the $\tilde{y}$-axes. This rotation decouples the particle track from the x-direction.

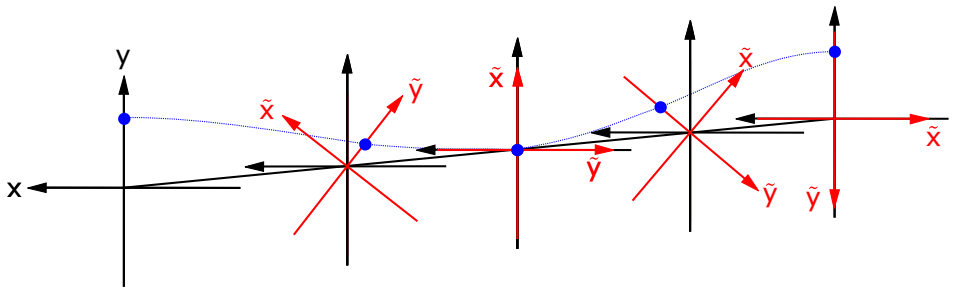

Figure 5.4: To provide a better understand of the decoupling mechanism applied by a rotating coordinate system, it is useful to follow the track of a circulating particle on the (x, y) orbit with an initial offset only in y direction. An accompanying rotating coordinate system $(\tilde{x}, \tilde{y})$, which depends on the particle's momentum p_z, the field B_s and the position s, decouples the motion and the particle moves only along the $\tilde{y}$ axis.

For proofing the beam dynamics with `ICOOL`, one single particle was initially generated with an offset of $y = 10\,\mathrm{cm}$ and a longitudinal momentum of $p_z = 176.4\,\mathrm{MeV/c}$ inside the environment of a homogeneous 4 T hard edge solenoid field. Tracking the particle position, which is recorded in the `ICOOL`'s output file. Observing the tracked particle position in the transverse plane shows the expected circular movement of the muon, as illustrated as the blue dots in Figure 5.5. Applying the rotation matrix

$$\mathbf{R}(\theta_{\mathrm{L}}) = \begin{pmatrix} \cos(\theta_{\mathrm{L}}) & 0 & \sin(\theta_{\mathrm{L}}) & 0 \\ 0 & \cos(\theta_{\mathrm{L}}) & 0 & \sin(\theta_{\mathrm{L}}) \\ -\sin(\theta_{\mathrm{L}}) & 0 & \cos(\theta_{\mathrm{L}}) & 0 \\ 0 & -\sin(\theta_{\mathrm{L}}) & 0 & \cos(\theta_{\mathrm{L}}) \end{pmatrix} \tag{5.5}$$

on each transverse particle position $(x,\ x',\ y,\ y',)$ follows to the predicted particle motion along the y-axes, depicted in Figure 5.5.

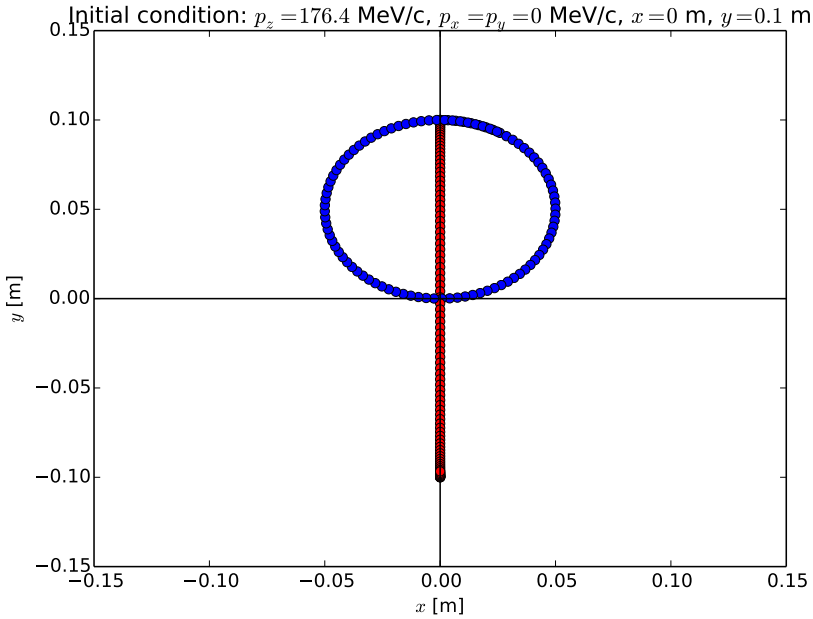

Figure 5.5: Tracking with `ICOOL` a muon in a 4 T solenoid field results to a circular motion (blue). In a rotating frame, the particle moves on the y-axis (red dots), which is depends only on one transverse plane.

After introducing the rotation matrix, it is worth to execute the transformation on the solenoid's transfer matrix

$$\mathbf{R} \cdot \mathbf{M}_{\text{Sol}} = \begin{pmatrix} C & S/\kappa & 0 & 0 \\ -\kappa S & C & 0 & 0 \\ 0 & 0 & C & S/\kappa \\ 0 & 0 & -\kappa S & C \end{pmatrix}. \tag{5.6}$$

It can be observed, that the decoupled matrix focuses a particle not only in (x, p_x), but also in the (y, p_y) phase space. That is one of the key arguments to use such solenoid for ionization cooling.

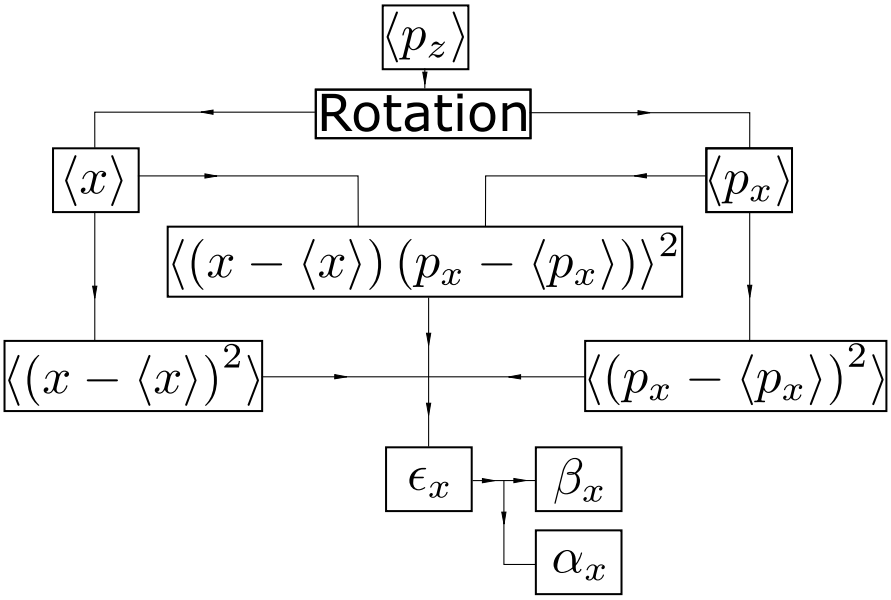

Figure 5.6: Flowchart of the beam parameter analyzes. The particles will be decoupled by a rotating coordinate system.

The next step is to apply the rotating coordinate system technique for evaluating the beam parameters of a whole muon bunch with ICOOL. The betatron function inside a solenoid for a specific reference momentum p_s and a constant field strength B_s can be calculated by means of equation (4.22). For each simulation it has to be ensured, that the beam parameters are matched with the given parameters of the lattice. For a hard edge solenoid, the matching condition of the muon distribution are

$$\sigma_{x,y} = \sqrt{0.3\frac{B_z m_\mu \epsilon_{\perp,\mathrm{N}}}{2}}, \quad \sigma_{p_x,p_y} = \sqrt{\frac{2 m_\mu \epsilon_{\perp,\mathrm{N}}}{0.3 B_z}}. \tag{5.7}$$

For instance creating a 1 m long and 4 T strong hard edge solenoid lattice with ICOOL, the value of the machine specific beta function is approximately 29.4 cm for a reference beam momentum of $p_s = 176.4\,\mathrm{MeV/c}$. For the ongoing simulation no energy spreads will be included. Further, a beam with 10^4 muons was created and distributed by means of 5.7. Otherwise, the betatron function of the beam would oscillate inside this optical element, due to beam filamentations [69].

After tracking the generated beam through that hard edge lattice in the ICOOL, the next task is to analyze the beam parameters provided in ICOOL's output file. Analyzing the beam parameters at each longitudinal position, the mean momentum $\langle p_z \rangle$ is evaluated. It is important to underline again, that ICOOL includes during the simulation the decay of the muon. Therefore it has to be taken into account, that any electrons will be

counted. Otherwise, the electron would distort the muon distribution and the emittance of the muon beam would not be constant anymore.

Further the transverse coordinates will be transformed by the matrix (5.5), which rotation angle is depending on $\langle p_z \rangle$, B_s and s. After decoupling, the next step is to calculate the transverse spreads $\langle x \rangle$, $\langle y \rangle$ and the mean transverse momenta $\langle p_x \rangle$, $\langle p_y \rangle$. Finally the normalized transverse emittance can be evaluated by means of equation (3.49). A flowchart in Figure 5.6 summarizes the operations steps of the beam parameter calculation.

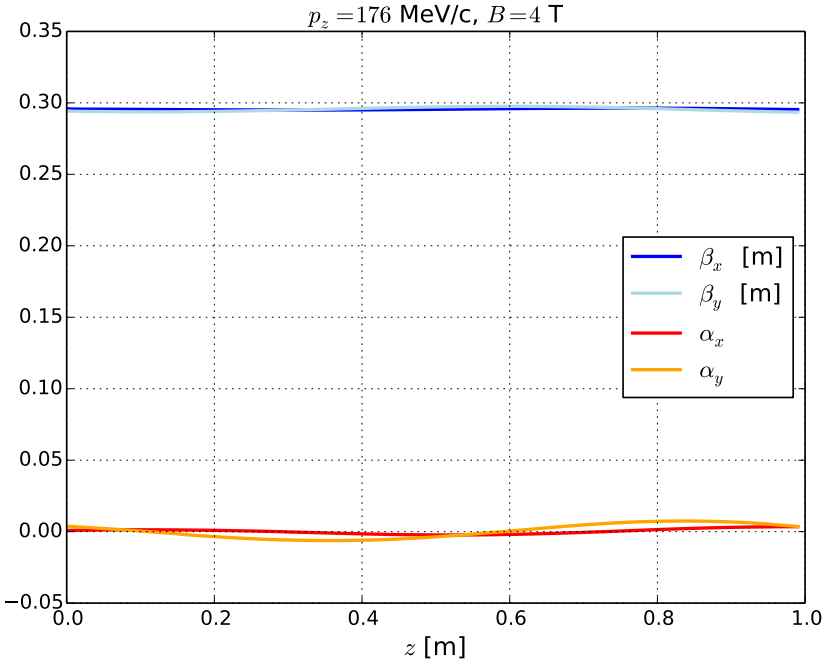

Figure 5.7: If the beam matches with the machine ellipse of a 4 T strong hard edge solenoid, it can be observed that the values β_x and β_y are indeed constant, applying a rotating coordinate system to decouple the particle coordinates. The correlations α_x and α_y are almost 0.

Back to the simulation example, the beam parameters can be evaluated along the optical axes. The beta functions and their corresponding correlations are illustrated in Figure 5.7 for both transverse planes. It can be noticed, that the beam fulfills almost the matching conditions (5.7) and the betatron functions β_x and β_y are indeed constant. The correlations α_x and α_y are oscillating weakly around zero, due to statistical reasons and can be improved by tracking a larger number of muons. But this will lead to longer running times by executing an `ICOOL` job.

After performing beam optics analyzes and material tests with ICOOL, the next step is to start simulations with solenoids, filled with low-Z materials inside. In the following chapter, the previously discussed decoupling technique will be applied for evaluating the normalized emittance reductions and compared with a standardized ICOOL diagnostic code.

Chapter 6: Cooling results in hard edge fields

This chapter presents the first ionization cooling results done by ICOOL in the case simple hard edge fields filled with absorbers. A semi-analytical code was developed to compute the cooling formula (4.21) and the results are compared with ICOOL simulations. Tracking the muon beam in a absorber field hard edge solenoidal field, two codes where applied after each ICOOL run for evaluating the beam parameters and their differences will be discussed in the following. In the final section, the influences of thin metallic windows on the emittance will be simulated and discussed.

6.1 Numerical solutions of the cooling equation

To become familiar with ionization cooling, it is useful to illustrate the emittance change graphically by performing semi-analytical calculations. While the cooling formula is not solvable analytically due to the heating component, a precise numerical method has to be chosen and applied on equation (4.21) for finding an appropriate approximation.To evaluate a first order differentiation formula numerically, the four-stage Runge Kutta (RK4) method was used here, as it is a fast and simple algorithm [107, 108].

Before going into the details ot this method, it is useful to define the common numerical solution of an arbitrary initial value problem $\partial y(x)/\partial x$, which is usually expressed as a multi-step linear equation or better known as a recursion formula in form of

$$y(x_{n+1}) = y(x_n) + \Delta x\, \Phi(x_n, y(x_n);\, \Delta x), \tag{6.1}$$

where the initial parameters x_0 and y_0 have to be given [109]. $\Phi(x_n, y(x_n);\, \Delta x)$ is the increment function and characterize such numerical approximations. The value Δx stands for the iteration step, which influences the calculation time and the precision of an initial value problem.

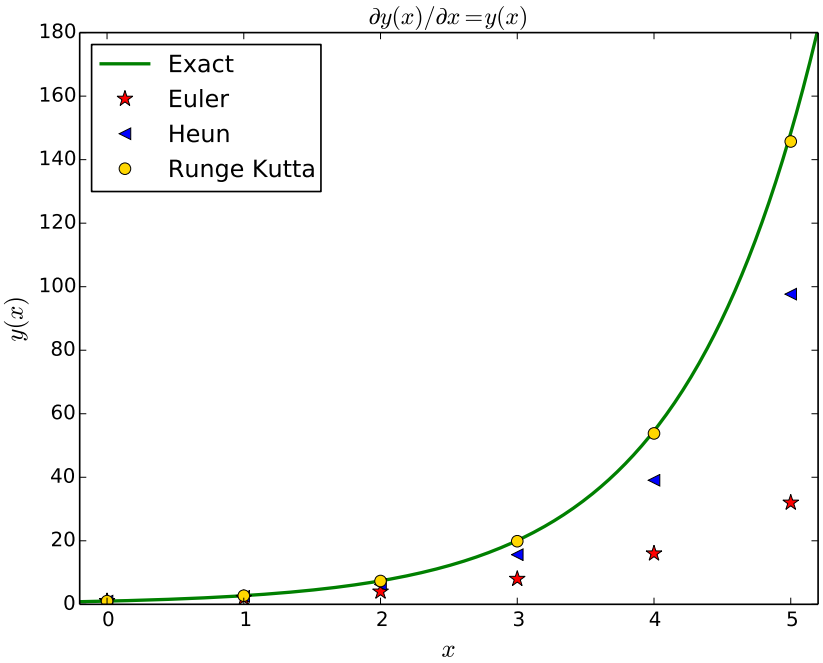

Figure 6.1: In this plot the function $\partial y(x)/\partial x = y(x)$ is numerically approximated by the RK4 method and compared with the Euler and Heun algorithm. By using $x(0) = y(0) = 0$ and $\Delta x = 1$, the RK4 fits very well with the analytical solution.

The increment of RK4 consists of four different slope functions and is expressed as

$$\Phi(x_n, y(x_n)) = \frac{1}{6}\left(k_1 + 2k_2 + 2k_3 + k_4\right), \tag{6.2}$$

while their definitions are written by discredizing the differential equation to

$$f(x_n, y(x_n)) = \left(\frac{\partial y}{\partial x}\right)_n \tag{6.3}$$

and the k terms finally specify to

$$\begin{aligned} k_1 &= f(x_n,\, y(x_n)), \\ k_2 &= f(x_n + \frac{\Delta x}{2},\, y(x_n) + \frac{\Delta x}{2} k_1), \\ k_3 &= f(x_n + \frac{\Delta x}{2},\, y(x_n) + \frac{\Delta x}{2} k_2), \\ k_4 &= f(x_n + \Delta x,\, y(x_n) + \Delta x k_3). \end{aligned} \tag{6.4}$$

The advantage of using RK4 compared to other conventional methods can be shown by the simple example $y(x) = \partial y(x)/\partial x$, which analytical solution is the exponential function. Choosing the initial condition $x(0) = y(0) = 0$ and the iteration step $\Delta x = 1.0$, the RK4 computation illustrated as the yellow dots in Figure 6.1 shows a good agreement with the analytical solution depicted in this graph as the solid line.

Compared to one-stage numerical methods, e.g. the Euler method [109] or the Heun technique [110], which reduces due to higher error expansions in using the same iteration like before as it can be seen in Figure 6.1. This single-step calculation can be improved with a smaller choice of Δx, however it will require computation time simultaneously.

Algorithm 1 solves the cooling equation with RK4

Require: $\epsilon_{\text{initial}}$, E_{initial}, E_{stop}, ΔE ▷ Initial conditions
function COOL(E, ϵ) ▷ Cooling function
  return $-\epsilon/(E\beta^2)$
end function
function HEAT(E) ▷ Heating function
  $a = \beta_\perp \, (13.6)^2$ ▷ Unit in MeV
  $b = 2\beta^3 E m c^2 L_{\text{R}}$
  return $(a/b) \times \langle \partial E/\partial z \rangle^{-1}$
end function

$\epsilon_0 = \epsilon_{\text{initial}}, \; E_0 = E_{\text{initial}}$
repeat
  save(ϵ_0, E_0)
  $k_1 = (\text{COOL}(E_0, \epsilon_0) + \text{HEAT}(E_0)) \times \Delta E$ ▷ Calculation of k_1

  $E_1 = E_0 - 0.5 \times \Delta E, \; \epsilon_1 = \epsilon_0 + 0.5 \times k_1$
  $k_2 = (\text{COOL}(E_1, \epsilon_1) + \text{HEAT}(E_1)) \times \Delta E$ ▷ Calculation of k_2

  $E_2 = E_1, \; \epsilon_2 = \epsilon_0 + 0.5 \times k_2$
  $k_3 = (\text{COOL}(E_2, \epsilon_2) + \text{HEAT}(E_2)) \times \Delta E$ ▷ Calculation of k_3

  $E_3 = E_0 - \Delta E, \; \epsilon_3 = \epsilon_0 + k_3$
  $k_4 = (\text{COOL}(E_3, \epsilon_3) + \text{HEAT}(E_3)) \times \Delta E$ ▷ Calculation of k_4

  $k = \frac{1}{6} \, (k_1 + 2k_2 + 2k_3 + k_4)$ ▷ Increment
  $\epsilon = \epsilon_0 + k$ ▷ Recursion formula

  $\epsilon_0 = \epsilon, \; E_0 = E_3$
until $E_0 \leq E_{\text{stop}}$

Applying the RK4 algorithm on the cooling formula, some changes of equation (4.21) have to be performed at first. Since the cooling equation is the derivative of the normalized transverse emittance with respect to the ideal orbit s, the iteration Δs could be used at the first look. However, since the energy change is high for materials in the range of $5 < E_{\mathrm{Kin}} < 100\,\mathrm{MeV}$, the choice of ΔE as energy step sizes might be more practical. Transforming equation (4.21) into a recursive expression yields to

$$\epsilon_{n+1} = \epsilon_n - \frac{\epsilon_n}{E\beta^2}\Delta E + \frac{\beta_\perp \left(13.6[\mathrm{MeV}]\right)^2}{2\beta^3 E m c^2 L_{\mathrm{R}}} \left\langle \frac{\partial E}{\partial s} \right\rangle^{-1} \Delta E, \tag{6.5}$$

where ϵ_n is defined here as the normalized transverse emittance at step n. For a specific material, the following code in algorithm 1 was created.

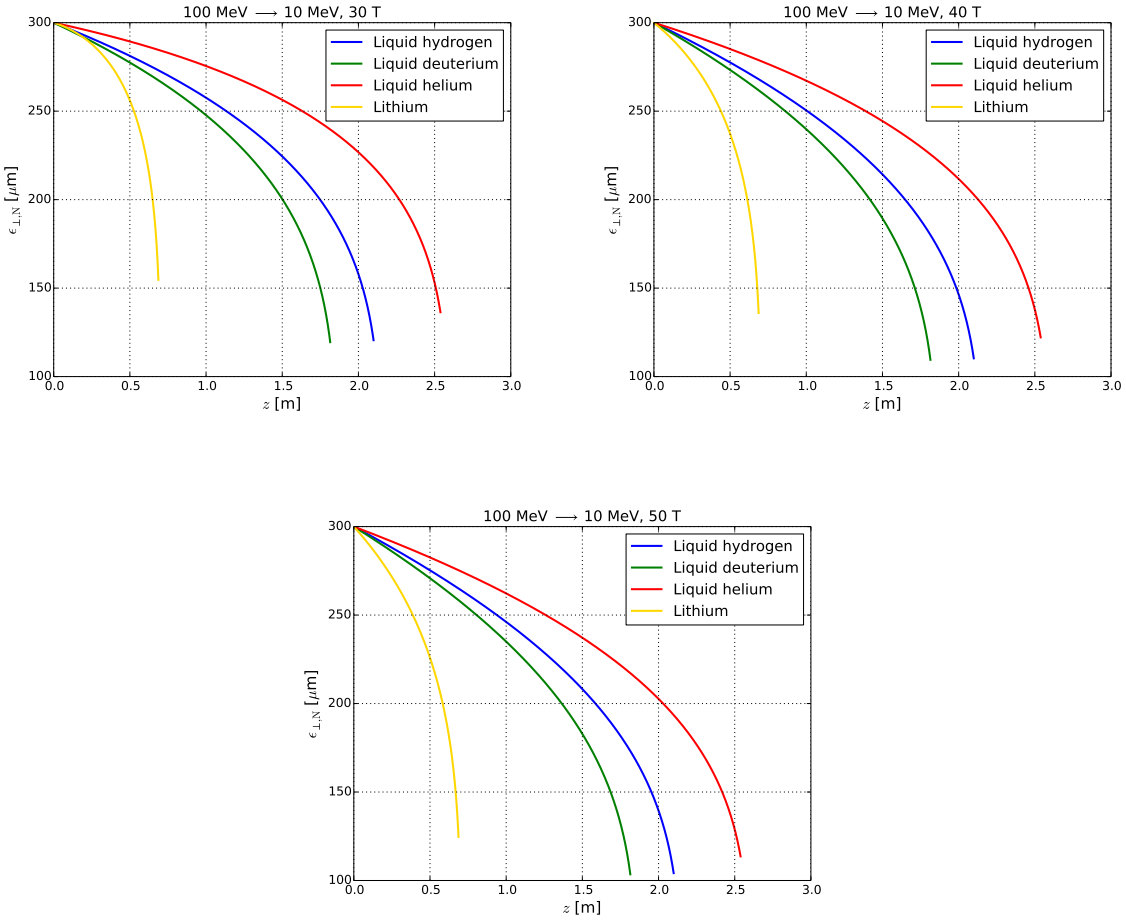

Figure 6.2: Emittance reductions with the initial parameters $\epsilon_{\perp,\mathrm{N}} = 300\,\mu\mathrm{m}$ and $E_{\mathrm{Kin}} = 100\,\mathrm{MeV}$. The approximations were computed using different absorbers and magnetic fields. The calculations stopped, when they reached a kinetic energy of 10 MeV.

The next step is to calculate several emittance reduction processes placed in different absorbers. It was suggested to compare liquid hydrogen, liquid deuterium, liquid helium and lithium under different magnetic fields [30 T, 40 T, 50 T] by varying the initial parameters $\epsilon_{\perp,\mathrm{N}}$ and E. An iteration step of $\Delta E = 0.1\,\mathrm{MeV}$ was chosen for evaluating the emittance computation very fast.

A past study [24] referenced, that the transverse normalized emittance reached a value of around $300\,\mu\mathrm{m}$, when the muon beam transfers from the 6D-cooling to the final cooling channel. Therefore, the first calculations starts with this parameter proposal, while an initial kinetic Energy of 100 MeV was chosen, since it is a limit for ionization coolings. Feeding algorithm 1 with the given initial parameters $\epsilon_{\perp,\mathrm{N}}$, E_{Kin} and ΔE, the resulting emittance approximations are presented in Figure 6.2, while the calculation routine stops after reaching the chosen stopping condition of $E_{\mathrm{Kin}} = 10$ MeV.

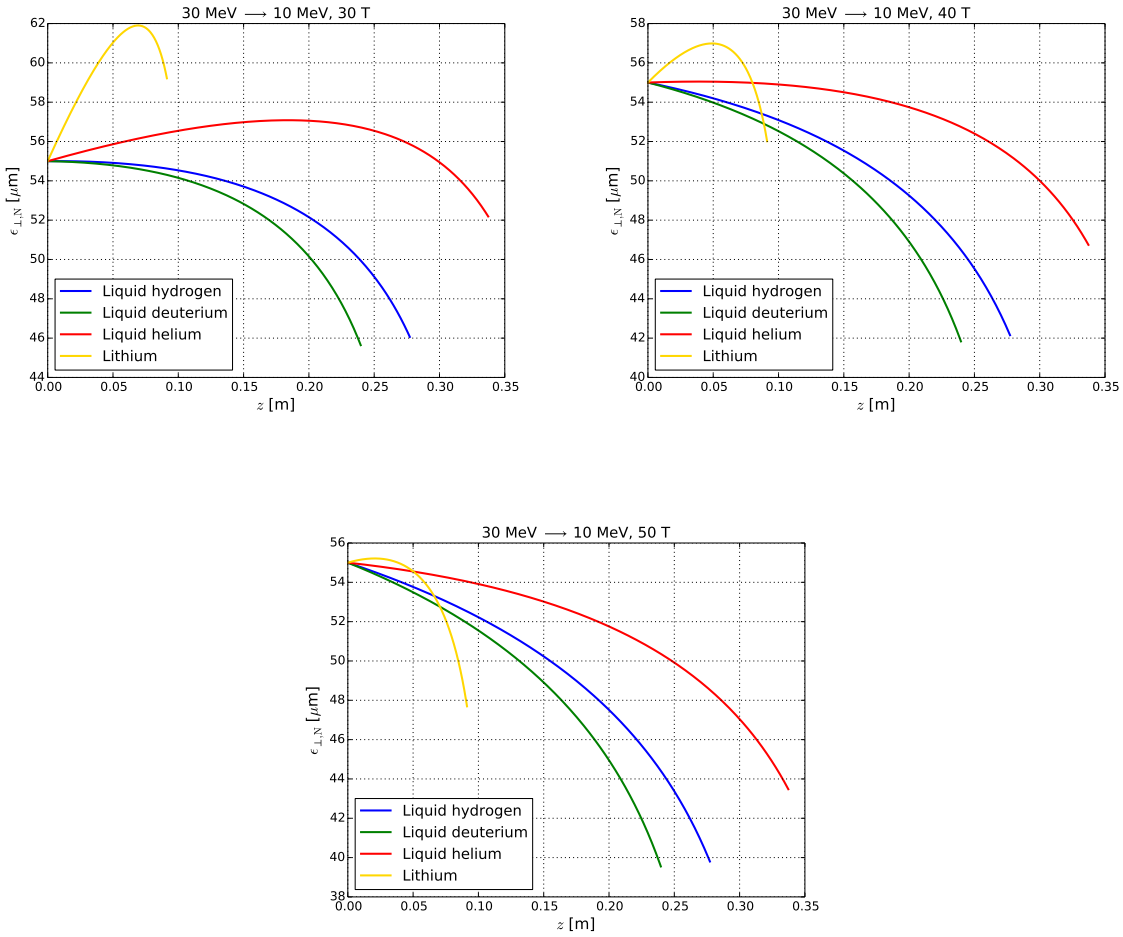

Figure 6.3: Approximation of the cooling equation beginning with $\epsilon_{\perp,\mathrm{N}} = 55\,\mu\mathrm{m}$ and $E_{\mathrm{Kin}} = 30\,\mathrm{MeV}$.

Figure 6.2 demonstrates the agreement with the predicted equilibrium emittance shown in Figure 4.6, proving that the beam will be cooled by all low-Z materials in the three high field environments. Especially lithium seems to be very effective, since it cools the emittance down to very low values within short distances. This could be a possible game changer for the costs of solenoid fabrications, because the solenoid's length can be shortened. Nevertheless, the solenoid and absorber width will stay in correlations with the size and costs of the re-acceleration components in the final cooling sector.

As it was already mentioned in the previous study [37], a final emittance of around 55 μm was reached, which is still a factor of 2 too high compared to the target parameter in table 1.1. For ensuring cooling, the initial kinetic beam energy must be low,according to (4.23). The field strength for was set at 50 T. For instance, let's consider a beam at an initial normalized transverse emittance of 55 μm and a kinetic energy of 30 MeV going through different absorbers, which results can be compared in Figure 6.4. Applying lithium and liquid helium results to large values of $\epsilon_{\perp}^{\mathrm{eq}}$ and would cool the beam very inefficient or even heat it up. Only liquid deuterium and hydrogen are suitable absorber candidates of a kinetic energy of $30 < E_{\mathrm{Kin}} < 10$ MeV.

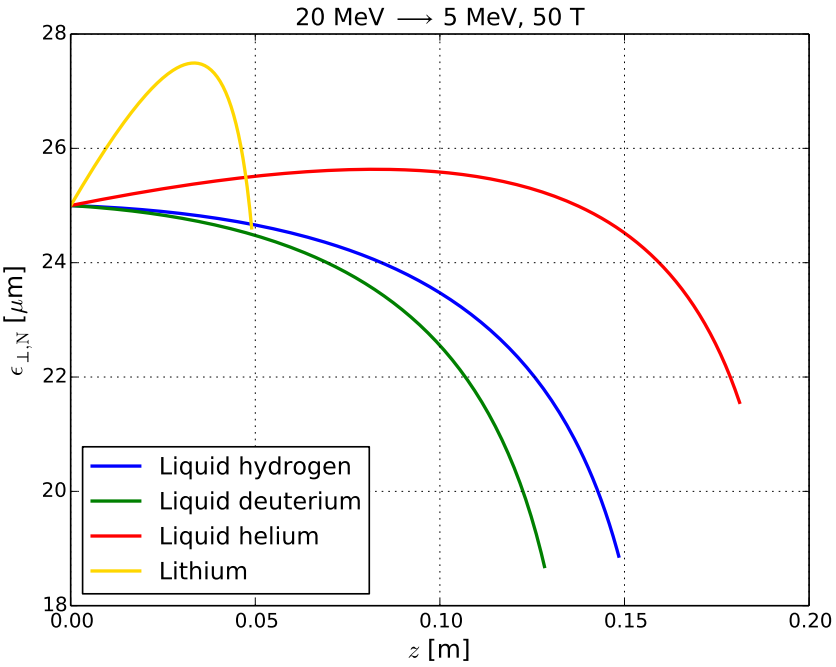

Figure 6.4: With 50 T solenoid fields it is still possible to cool the target emittance of 25 μm further down with liquid hydrogen or deuterium.

The take home massages of the plots in Figure 6.2 and 6.3 is, that in the high emittance and high energy range lithium would be suitable for absorbers in a final cooling cell.

But, the absorber length has to be short, because the muons would be decelerate to much and decay in addition. In the simulations Otherwise, in low emittance and energy ranges, only liquid hydrogen or deuterium can be used, while the other elements seems to be very inefficient for ionization cooling. Liquid helium shows in general a very bad performance, since it is a noble gas and therefore hard to ionize. The interaction of imping muons in helium with its strong bounded electrons is weak and therefore the muons' momentum can not be significantly reduced and cooling becomes inefficient. These primary calculations proof already, that liquid helium can be excluded for future absorber choices in final cooling.

Before closing this section, it is worth to mention, that maybe it would be possible to cool a beam below the emittance goal of 25 μm, which would improve other target parameters for the muon collider design. This would for example reduce the muon production at the proton-target interaction point or would decrease the size of the entire muon collider complex. As Figure 6.4 depicts, it is indeed possible to reach values below 25 μm with liquid hydrogen or deuterium for example inside 50 T fields.

6.2 First emittance reduction demonstration with `ICOOL`

The next step is to compare the theoretical predictions with the simulations. Here, the emittance reductions of a hard edge solenoid with absorbers are investigated. The solenoid is sliced in the simulation, possible due to condition

$$\mathbf{M}_{\text{exit}} \cdot \mathbf{M}_{\text{entry}} = \mathbb{1}, \tag{6.6}$$

coming from description (3.21).

In the simulation setup, 10^4 particles were used for each `ICOOL` job. The hard edge field lattices for 30 T and 50 T were generated and the beam ellipse was matched with the solenoid machine ellipse corresponding to criteria (5.7) transverse sizes. The initial normalized transverse emittance of $\epsilon_{\perp,\text{N}} = 300\,\mu$m was chosen in these examples and the initial kinetic energy in beam direction started at 100 MeV. No additional longitudinal momentum spread was included for this studies.

It was decided to test a 1 m hard edge solenoid filled with liquid hydrogen and liquid deuterium. Tests with liquid helium were excluded, since the last section underlined its unusable properties. Simulating with lithium at 100 MeV kinetic energy, only a 60 cm solenoid can be used, because the muons would completely decelerate and further decay inside a longer absorber.

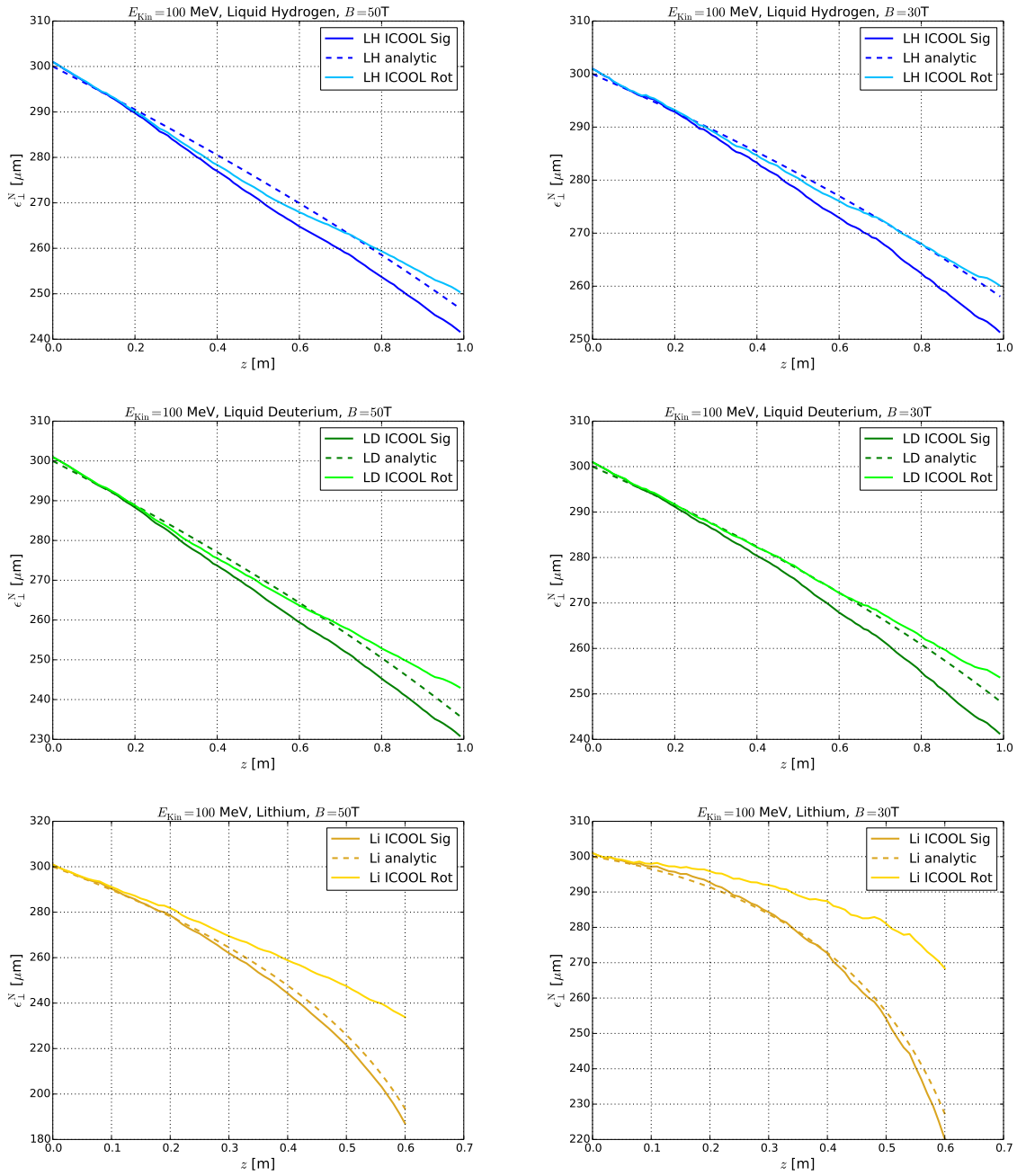

Figure 6.5: `ICOOL` simulations with liquid hydrogen, fluid deuterium and lithium inside a 50 T and 30 T hard edge field environment. The beam parameter analyzes were performed with `Ecalc9` and the rotating decoupling code described in section 5.3, which are compared with the theoretical prediction.

For beam parameter analyzes, two codes were applied and compared to each other. One

program is the decoupling technique with a rotating coordinate system described in section 5.3. The second code is included in the ICOOL download package and is called Ecalc9 programmed by G. Penn [101]. Both codes were executed after one ICOOL job and compared with the theoretical prediction from section 4.3. The results are summarized in Figure 6.5.

It is noticeable, that as well Ecalc9 as the rotation analysis code agrees at the first few cm with the cooling equation (4.21). However, the trend of Ecalc9 deviates downward the semi-analytical prediction, while the rotation technique behaves the other way round. In the cooling simulations with lithium, it is clear to see that only Ecalc9's analysis follows the shape of the cooling theory.

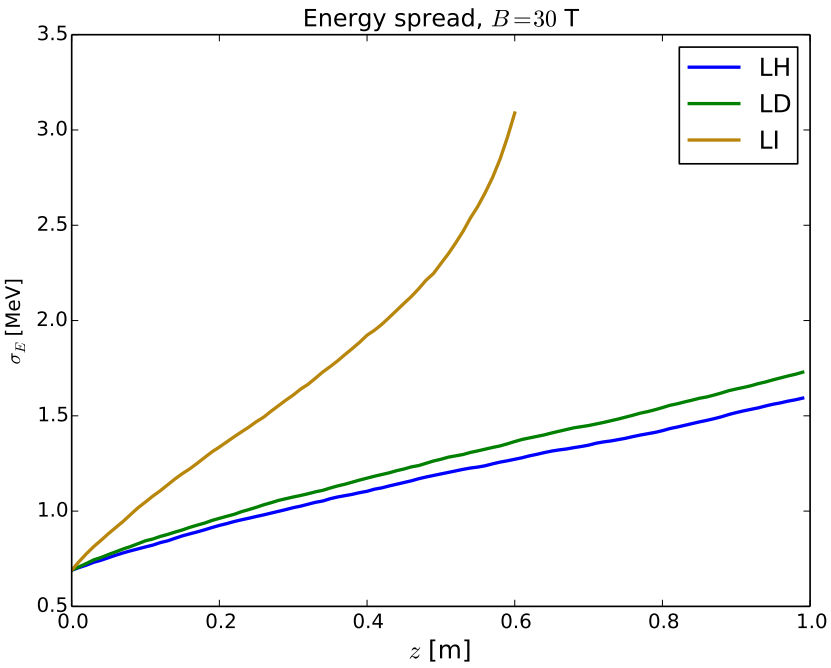

Figure 6.6: Energy spread increase using different materials. Higher densities resukts to higher stopping powers and therefore more statistical fluctuations in the energy distribution in a bunch of muons.

It is necessary to notice, that muons are decelerated differently due to straggling, which influences statistical fluctuations in the muons' energy of the bunch. This energy distribution can be expressed as the so called energy spread σ_E and Figure 6.6 shows that it is clearly observed to the density of the material, when muons penetrate with initial 100 MeV through the absorber.

It can be assumed that higher stopping power rates tends to higher spreads. This equally means, that an applied rotating coordinate system could not be matched anymore with high values of σ_E, which can be clearly identified by analyzing the results of the cooling using lithium. For future simulations it will be therefore recommended to analyze the beam parameters with `Ecalc9`, since it is more reliable concerning σ_E growth.

It can be recognized in Figure 6.5, that the emittance evaluation with `ECALC9` has also a weak offset compared to the cooling equation (4.21), which expands with growing σ_E. A possible explanation for this could be, that hard scattering events were not excluded in the description of the cooling equation (4.21), but it was still contained in the simulation by using the Fano model. If those wide angle events would not be included in the simulation, like it was done with 1 m long liquid hydrogen target inside a 50 T field, it can be seen in Figure 6.7, that the simulations indeed follow the semi-analytical model from chapter 4. It has to be mentioned, that this is the case only for the `Ecalc9` analyzes and deviations of the rotating technique comes out more clearly in this example. However, the inclusion of high scatter events is a more realistic assumption and therefore it will be used for future `ICOOL` simulations.

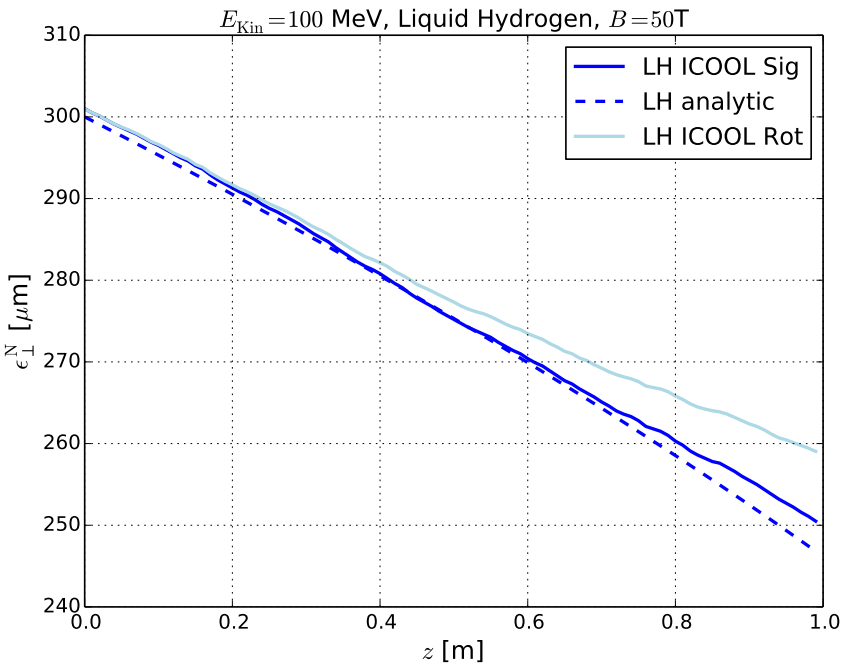

Figure 6.7: The `Ecalc9` routine agrees better with the theoretical model, if hard scatter events are be excluded.

6.3 Thin metallic window impact on emittances

After reaching the final target emittance of 25 μm in a liquid hydrogen or deuterium absorber, the effects of the beam after passing the confinement window are still not be understood. As it was mentioned in section 5.1, Be and Al has to be considered.

Let's assume a window thickness of a few hundreds of μm and choose several different initial beam momenta. The beam reaches a low energy, when it passes through the absorber, thus it has been decided to start simulations with the kinetic beam energy of [10, 8, 6, 4] MeV and an initial emittance of 25 μm. The simulations were done with 50 T strong hard edge solenoids and includes Be or Al as absorber. Since the range is small compared to the absorber thicknesses, the particle simulation step size was set to 1 μm. For evaluating the emittance change, `ECALC9` was applied and additionally the particle transmission was determined, which is in other words the particle survival rate. For all simulations 10^5 muons are generated.

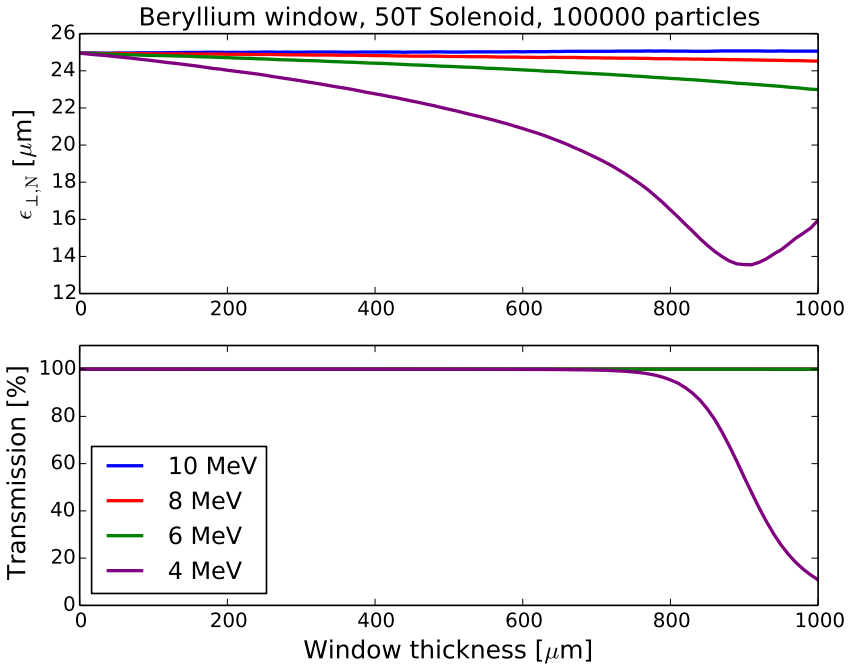

Figure 6.8: Results obtained with `ICOOL` demonstrate, that no influence on heating effects on the emittance and can still cool down the beam after served 100 μm of thickness. Care must be take at very low kinetic energy as in the case of 4 MeV/c, where the particles decay after around 700 μm.

Results with Be shown in Figure 6.8 demonstrate, that the emittance is almost constant

at 10 MeV and 8 MeV and no particle loss is observed. Comparing with Figure 6.10, the initial conditions are indeed above the equilibrium emittance, which consequently provides cooling. Even with 6 MeV initial kinetic energy the beam will be still cooled down to 23 μm, which is slightly an advantage. However, at 4 MeV initial E_{Kin} of the beam was also cooled, but at 700 μm of Be thickness the transmission breaks down. Simultaneous show it was experienced, that under a certain momentum the muons decay in `ICOOL`.

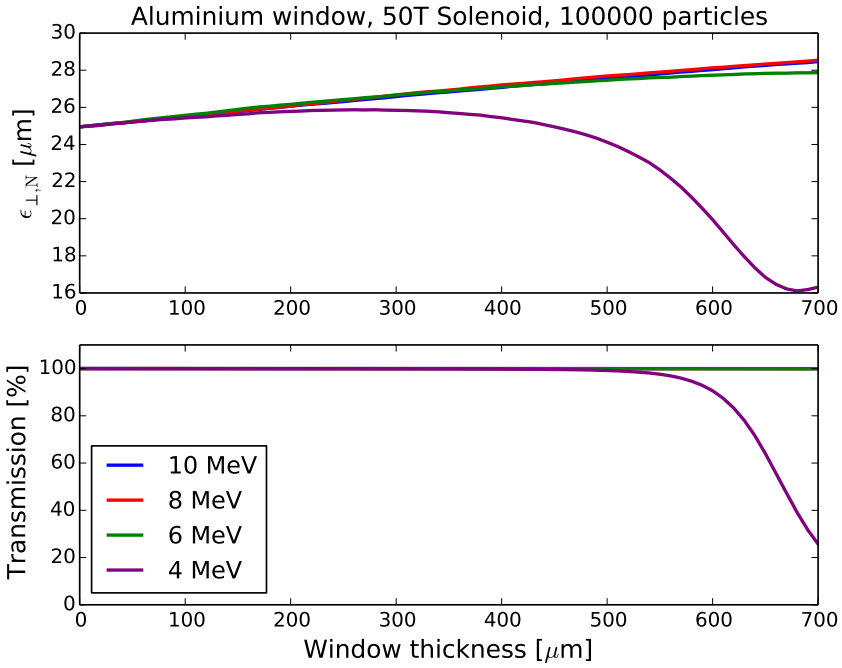

Figure 6.9: Simulated emittance change using Al window shows, that with an initial beam energy of 4 MeV/c the emittance is almost not influenced by any heating effects, if the thickness is lower than 500 μm.

Heating impacts are more obvious for Al windows, due to their higher density. Figure 6.10 proves this statement, because the initial emittance at the energy range 10-4 MeV are below the equilibrium. It can be observed in Figure 6.9, that the beam has to be cooled below the target value, due to a slight emittance increase caused by heatings.

For a range of kinetic energy decreases, after reaching the target emittance of 25 μm in liquid hydrogen, Al has more disadvantages compared to Be as a window. At higher energies, due to the reheating effects it will be hard to achieve the emittance below its target value once inside the window simultaneously (e.g. at $\sim$ 10 MeV). For lower energies, the target emittance can be reached more easily. However an Al window has

to be thin enough to avoid a complete stopping of the muon beam, in the low energy case. The usage of Be windows seem to be more promising since the stopping power is lower than for Al and the emittance does not increase. Even for kinetic energies below 8 MeV, the emittance can be still reduced. However, it is not sure how thin Be can be technically produced. An alternative to both elements would be Mylar [105], which is 6 μm thick. It has been used for liquid hydrogen confinements in the field of nuclear spallation experiments.

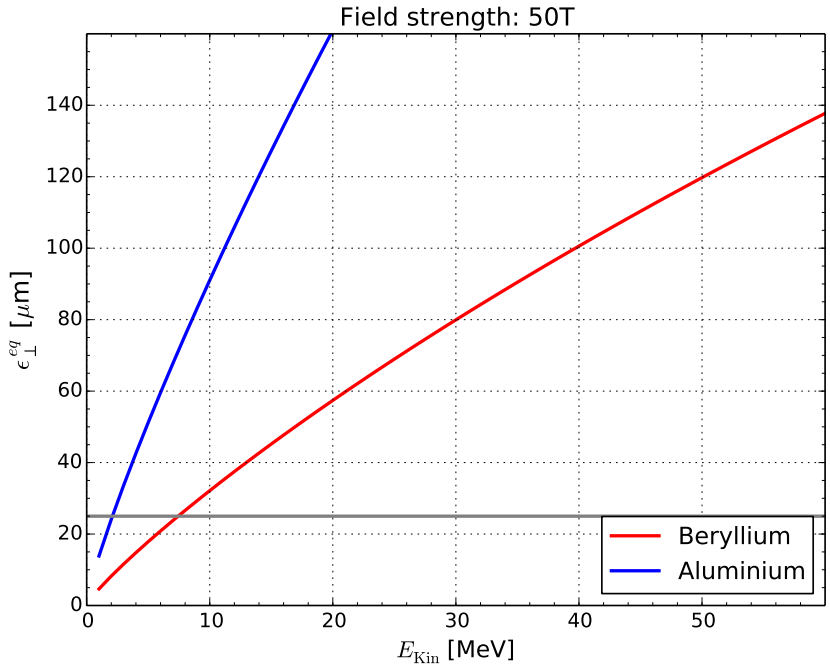

Figure 6.10: Equilibrium emittance curves of Al and Be at 50 T solenoid strength.

Chapter 7: Cooling in soft edge fields

So far, the cooling of a muon beam in simple hard edge solenoids was considered. As demonstrated on the simulations described in the last chapter, the results obtained with ICOOL agree with the theoretical model. However, in order to take into account the realistic case, solenoids with end field effects must be included in the simulation, which are also known as soft edge fields.

7.1 Field shape requirements

The HF solenoids, which are designed to achieve field strengths between 30 T and 50 T, are made of superconducting materials consisting of special atomic lattice structures. The first prototypes [111, 112] of those are composed of wrapped tapes inside as inner layers around such solenoids, which are made out of rare-erth barium copper oxide (ReBCO). ReBCO is a high temperature superconductor (HTS), providing very high upper critical field strengths B_{c_2} and would therefore be especially suitable for muon cooling. Other non-HTS material lose their super conductive properties due to very low B_{c_2} values.

However, if constructing HF solenoids pure HTS would drive up the costs of a future muon collider construction massively, because high costs of such super conductors. Hence, it is proposed to use Nb_3Sn additionally to wrapped around the ReBCO tapes for mitigating HTS materials. According to the current state of the art, it is already possible to produce solenoids with a strength of 28 T industrially [113].

The behavior of such magnetic field in the longitudinal direction can be described by means of equation (3.11) introduced in chapter 3. The field strength depends on the ratio between the length L of the solenoid and its radius R. As mentioned before, HF solenoids will be expensive and therefore they can not become arbitrarily long. It is proposed to set in this work L constant, thus the fringe field is a function of R.

According to the final cooling channel design, the field of a real solenoid must fulfill two important requirements. Firstly, it must reach its peak in the absorber area and

secondly, it has to be as constant as possible through that stopping material, since a constant field is required according to the derivation of the cooling equation (4.21). Lets assume a solenoid with a fixed length of 1 m and vary its radius arbitrarily by means of equation (3.11) analytically demonstrated in Figure 7.1. It can be determined, that these two criteria can be archived, when the ratio between the radius and the length of a solenoid will be small enough. Under this condition the range of the fringe fields will be decreased.

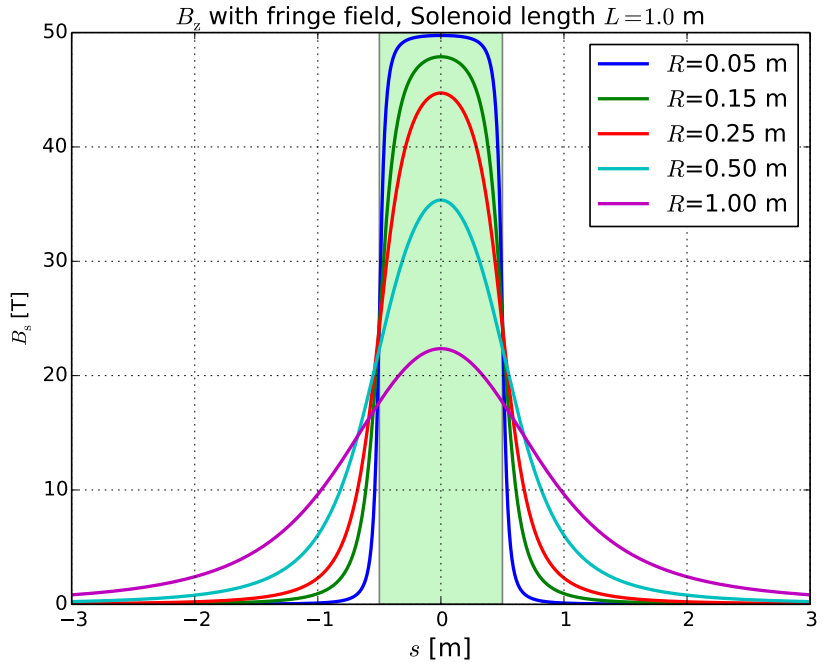

Figure 7.1: Final cooling requires high and almost constant field B_s. The physical range of the solenoid is illustrated as the light green area in the plot. The behavior of the fringe field can be studied by comparing different radii.

7.2 Analytical soft edge lattice design

Chapter 3 introduced a linear approximation of the transfer matrix (3.24) of a hard edge solenoid. A single transfer matrix for soft edge solenoids does not exist, but it can be expressed by a so called lattice matrix $\mathbf{M}$. It is a multiplication of several transfer matrices of the beam line and forecasts the particle coordinates at the end of this lattice by given initial coordinates.

A soft edge field can be sliced in multiple hard edge solenoids $\mathbf{M}_i$ in the linear approximation, which have an infinitesimal length Δs. The s depended field strength follows equation (3.11). Each optical element has therefore an individual field $B_s(s)$, which depends on the position s of the reference orbit, which is illustrated in Figure 7.2

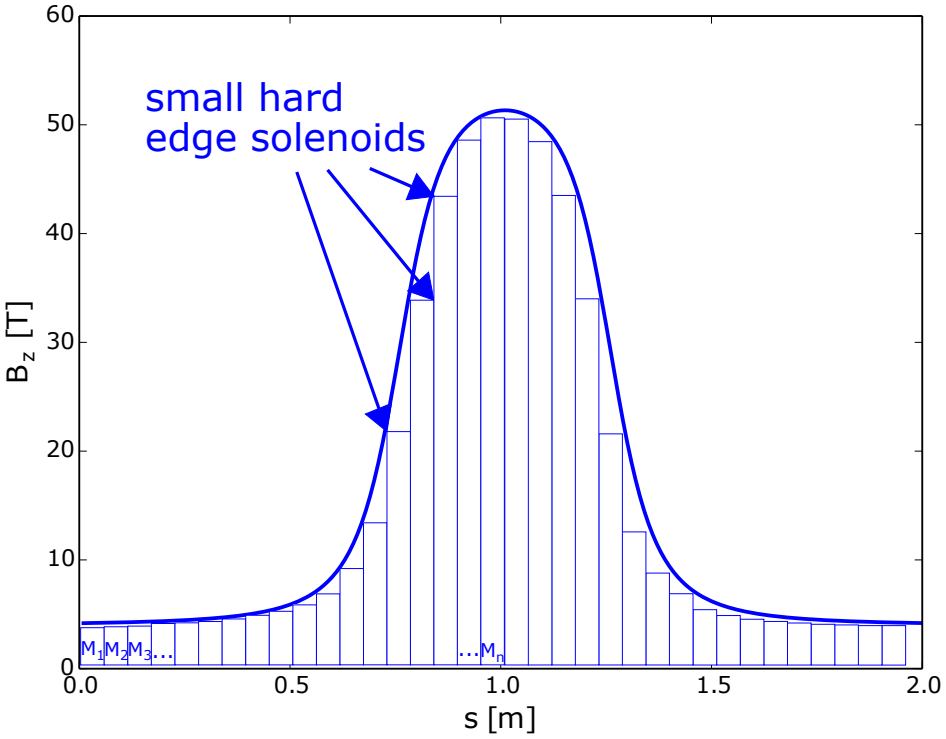

Figure 7.2: The particle transfer in a solenoid can be described by a lattice matrix contained by a numerous small hard edge matrices $\mathbf{M}_i$. Each infinitesimal optical element has a specific field strength, which depends on the longitudinal position s for ensuring the magnetic strength $B_s(s)$ and follows the soft edge typical shape.

In the next step, the series of hard edge elements are expressed as the lattice matrix of the soft edge solenoid

$$\mathbf{M}_{\text{Soft}} = \prod_{i=1}^{n} \mathbf{M}_{n-i}, \tag{7.1}$$

while the sequence of the multiplications follows the linear algebra of the beam dynamics matrix formalism [70]. For the final cooling however, the transfer from the beginning to the peak field area of the soft edge solenoid is in the main focus of interest. As it was demonstrated in 4, efficient ionization cooling requires a constant betatron function and zero correlation. Hence, the aim is to reach a minimum of correlation in the peak field

B_p of a soft edge solenoid. There, the Twiss parameters scale to

$$\begin{pmatrix}\beta_\mathrm{p}\\ \alpha_\mathrm{p}\\ \gamma_\mathrm{p}\end{pmatrix} = \begin{pmatrix}1/\kappa_\mathrm{p}\\ 0\\ \kappa_\mathrm{p}\end{pmatrix}, \tag{7.2}$$

where κ_p is the solenoids square rooted focusing strength at B_p. The value of the beta function in the central field is expressed by equation (4.22), while the divergence γ_init can be expressed by definition (3.34) by considering zero correlations. `ICOOL` generates in the beginning of each run an uncorrelated beam, which means that the initial Twiss parameters are

$$\begin{pmatrix}\beta_0\\ \alpha_0\\ \gamma_0\end{pmatrix} = \begin{pmatrix}1/\kappa_0\\ 0\\ \kappa_0\end{pmatrix}, \tag{7.3}$$

with κ_0 as the function of the initial focusing strength in the low field area. Hence, the next task is to find the lattice matrix, which transforms the parameters (7.3) into (7.2). In the linear approximation, a transformation matrix (3.37) was introduced in chapter 3, which components $T_{ij}(R)$ $(i,j=1,2,3)$ can be constructed by the lattice matrix (7.1) and the Twiss transformation follows to

$$\begin{pmatrix}\beta_\mathrm{p}\\ \alpha_\mathrm{p}\\ \gamma_\mathrm{p}\end{pmatrix} = \begin{pmatrix}T_{11} & T_{12} & T_{13}\\ T_{21} & T_{22} & T_{23}\\ T_{31} & T_{32} & T_{33}\end{pmatrix}\begin{pmatrix}\beta_0\\ \alpha_0\\ \gamma_0\end{pmatrix}. \tag{7.4}$$

This matrix depends on the radius of a solenoid and has to be optimized for satisfying condition (7.4). For instance this can be reached by calculating the Twiss transfer matrix with several radii. A radial scan from a starting value R_min to a limitation R_max in step size ΔR can be applied for evaluating the lattice matrix from $s=0$ to the peak field's position and makes it possible to compute $T_{ij}(R)$. Thus, the optimum radius can be found by defining three constrain functions

$$\begin{aligned} g_1 &= \beta_\mathrm{p} - \beta_0 T_{11} - \alpha_0 T_{12} - \gamma_0 T_{13} = 0,\\ g_2 &= \alpha_\mathrm{p} - \beta_0 T_{21} - \alpha_0 T_{22} - \gamma_0 T_{23} = 0,\\ g_3 &= \gamma_\mathrm{p} - \beta_0 T_{31} - \alpha_0 T_{32} - \gamma_0 T_{33} = 0, \end{aligned} \tag{7.5}$$

by searching the minimum value of $G = \sqrt{g_1^2 + g_2^2 + g_3^2}$.

A specific algorithm requires a given peak field of the solenoid and also an offset field B_Off, since the muons are generated in a low field environment. The computed values G will be saved to the corresponding radii in a list. At least, the optimized radius can be obtained by searching the minimum number in that list. Assuming a constant solenoid length L_Sol and knowing the position s_p of the peak field, the following method is proposed in algorithm 2.

Algorithm 2 optimizes the radius of a final cooling solenoid

Require: B_p, B_Off, R_min, R_max, ΔR, L_Sol, ΔL, s_p, p ▷ Initial conditions

function SOFT(B_p,L,R,s,B_Off) ▷ Solenoid field
    $f_1 = (s + 0.5L)/\sqrt{R^2 + (s + 0.5L)^2}$
    $f_2 = (s - 0.5L)/\sqrt{R^2 + (s - 0.5L)^2}$
    return $B_\mathrm{p} \times 0.5(f_1 - f_2) + B_\mathrm{Off}$
end function

function SOL(p,B, ΔL) ▷ Hard edge solenoid matrix
    $\kappa = 0.15 \times B/p$ ▷ Focusing strength
    $C = \cos(\kappa\,\Delta L)$
    $S = \sin(\kappa\,\Delta L)$
    return $[[C,\ S/\kappa], [-\kappa S,\ C]]$
end function

function TWISS($\mathbf{M}$) ▷ Twiss transformation matrix
    $c = M_{11}$, $s = M_{12}$
    $c' = M_{21}$, $s' = M_{22}$
    return $[[c^2,\ -2cs,\ s^2], [-cc',\ sc' + s'c,\ -ss'], [c'^2,\ -2c's',\ s'^2]]$
end function

$\beta_0 = p/(0.15 \times B_\mathrm{Off})$, $\gamma_0 = 1\beta_0$ ▷ Initial Twiss parameters
$\beta_\mathrm{p} = p/(0.15 \times B_\mathrm{p})$, $\gamma_\mathrm{p} = 1\beta_\mathrm{p}$ ▷ Twiss parameters at peak field
$R = R_\mathrm{min}$
repeat
    $\mathbf{M} = \mathbb{1}$ ▷ 2×2 Unitary matrix,
    $L = 0$
    repeat
        $B =$SOFT(B_p, L_Sol, R, L, B_Off)
        $\mathbf{M} =$ SOL(p,B,ΔL)$\times\mathbf{M}$
        $L = L + \Delta L$
    until $L > s_\mathrm{p}$ ▷ Stop at the peak field position
    $T =$ TWISS($\mathbf{M}$)
    $g_1 = \beta_\mathrm{p} - \beta_0 T_{11} - \gamma_0 T_{13}$
    $g_2 = \beta_0 T_{21} + \gamma_0 T_{23}$
    $g_3 = \beta_\mathrm{p} - \beta_0 T_{31} - \gamma_0 T_{33}$
    list.**append**$\left(\sqrt{g_1^2 + g_2^2 + g_3^2}\right)$ ▷ Save values into a list
    $R = R + \Delta R$
until $R > R_\mathrm{max}$
$R_\mathrm{opt} \leftarrow \min(\mathrm{list})$ ▷ Minimum value from list follows to optimum radius

As an example serves a beam with initial normalized transverse emittance of 55 μm generated in a low field environment of 4 T. The goal is to reach a peak field of 50 T in the solenoid's center. With the beam momentum of 80 MeV/c the initial Twiss parameters (7.3) can be calculated. Lets further assume a 0.5 m long solenoid and create multiple lattice matrices by a radial scan. Care must be taken to limit the radius in its size, due to the peak field's fall off. Each radius corresponds to defined peak beam parameters and a corresponding transformation matrix. The optimized radius finally results by using algorithm 2.

After performing the optimization of the fringe field, it is possible to illustrate the transverse beta function $\beta_\perp$ and the corresponding derivative of the betatron oscillation $\beta'_\perp$, which is function of the beam correlation $\alpha_\perp$. This can be performed by taking the parameters of the optimized lattice matrix and compute $\beta_\perp(s)$ and $\beta'_\perp(s)$ over the reference orbit s by means of the envelope equation (3.30) for proofing the final cooling conditions at the peak field region. Figure 7.3 shows the results from the previous example and indeed a very weak oscillating correlation and a constant beta function in the center is observed at around 1.0 m, which corresponds to the center of the solenoid.

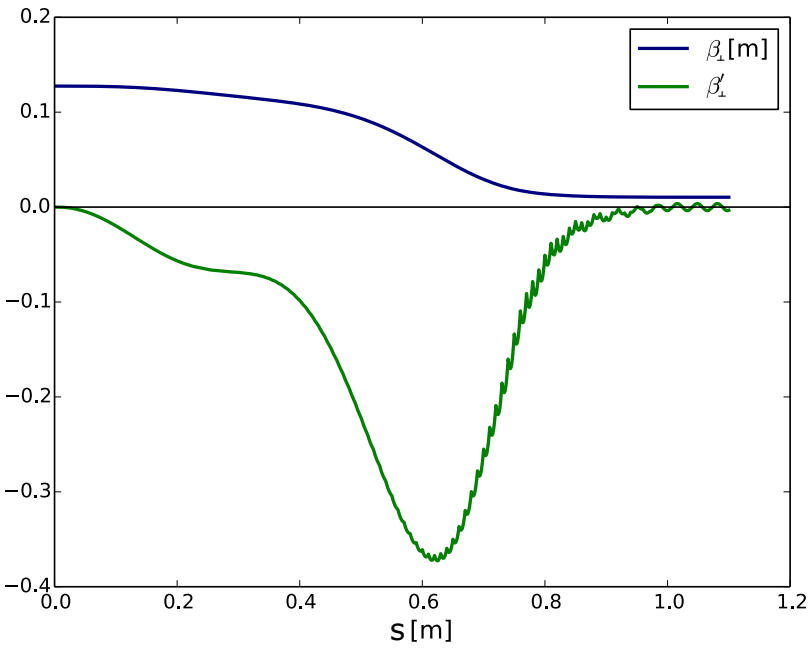

Figure 7.3: Along the solenoid's axis s, the fringe field has to be optimized by finding a suitable radius. For a 0.5 m solenoid and with its peak field at the position $s = 1.0$ m, minimum correlation expressed as a function of $\beta'_\perp$ can be found in the HF region with a constant betatron function $\beta_\perp$ inside.

7.3 ICOOL simulations in soft edge fields

Evaluating computational an optimized fringe field by given beam parameter, the next step is to create a corresponding solenoid map in ICOOL. It was suggested to use the solenoid model 2 of this program [101], which describes the soft edge field by tanh-approximation

$$B_s(s) = \frac{B_c}{2}\left[\tanh\left(\frac{s - L_{End}}{L_A}\right) - \tanh\left(\frac{s - L_c - L_{End}}{L_A}\right)\right] + B_{Off}. \tag{7.6}$$

This approach includes the central field strength B_c and an additional offset field B_{Off}, because the particles will be generated already in a low field environment before they propagate through the solenoid. The length L_{End} describes the orbit before entering and after the leaving of the solenoid. The parameter L_c stands for the physical length of the solenoid. The so called attenuation width L_A is a parameter, which defines the slope of the fringe field and rises with decreasing L_A.

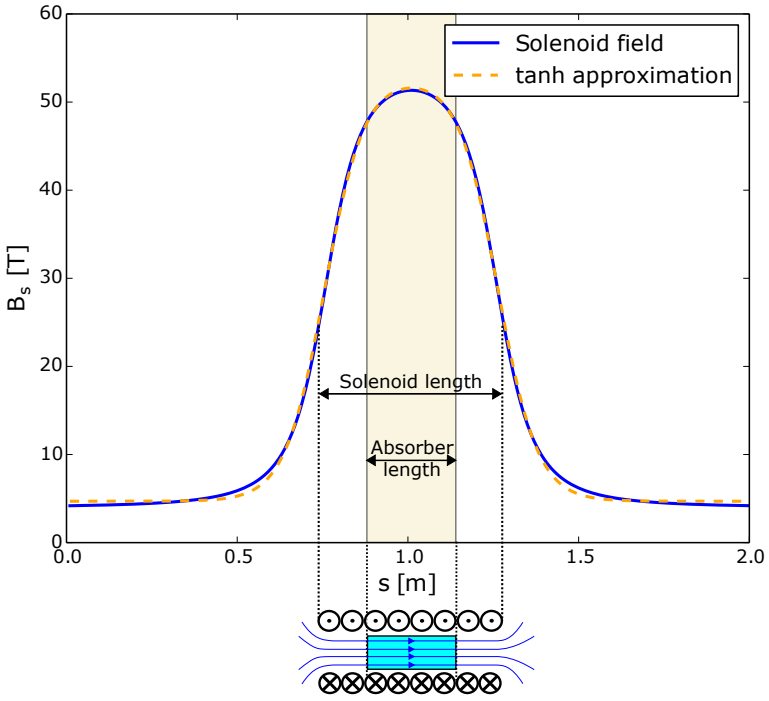

Figure 7.4: After evaluating the optimized soft edge solenoid, a tanh depended function will be fitted on that for creating an appropriate lattice with a certain ICOOL solenoid model. Inside the optic, an absorber with a pre-calculated length will be integrated symmetrically around the peak field area.

While a optimized field shape of $B_s(s)$ was found in the section 7.2 by means of equation (3.11), the next task is to find an equal field in ICOOL with equation (7.6). Therefore a fitting algorithm called curve_fit from scipy [114] was used, which is an optimization package of python. Evaluating the field parameters, the tanh-function (dashed line) can be compared with the equation (3.11) in Figure 7.4, which are in a good agreement with the analytical optimization of the soft edge field described in section 7.2 before.

Further, an absorber has to be placed inside the solenoid for cooling the beam. With the knowledge of the initial beam momentum p_s of about 80 MeV/c, it is possible to estimate the absorber thickness by means of the cooling equation (4.21). By using liquid hydrogen as stopping material and assuming a beam cooling until a mean momentum of around 33 MeV/c ($E_{\mathrm{Kin}} \approx 5$ MeV) will be reached, the absorber width is around 26 cm. Thus, the absorber will be set symmetrically around the peak field area of the solenoid in the ICOOL code, like it is illustrated as the creme colored surface in Figure 7.4.

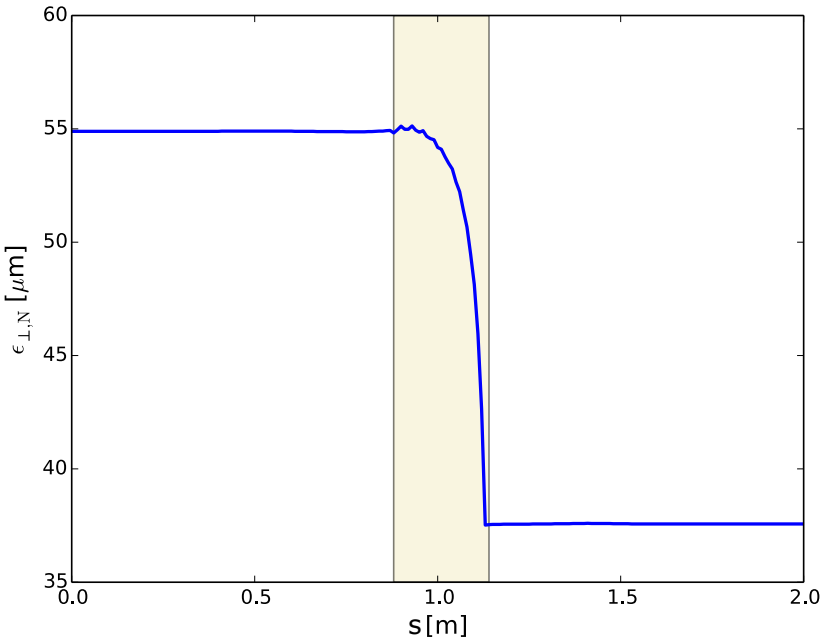

Figure 7.5: A muon beam with an initial momentum of 80 MeV/c and a normalized transverse emittance of 55 μm enters in a soft edge field of a 0.5 m long physical solenoid. A 26 cm long liquid hydrogen absorber is placed symmetrically around the $\sim$ 50 T HF marked as the creme colored surface. The beam will be cooled down until it reaches a mean momentum of 33 MeV/c, while the beam's emittance was reduced to 37 μm

For the simulation, a beam with 10^5 particle was created and matched with the optimized machine parameters with the matching criteria (5.7). The simulation step size was set at 1 mm and the transverse normalized emittance was evaluated with `Ecalc9` after running the job.

As it can be observed in Figure 7.5, it is indeed possible to cool a muon beam below 55 μm with a field of around 50 T. Nevertheless, it is also clear to see that the emittance is after entering the absorber in the first 10 cm nearly constant. This means that there exist still heating effects caused by correlation terms.

For optimizing the soft edge field, further studies has to be taken into account. The next step is to focus on more realistic solenoid models in `ICOOL` and try to use other optimization techniques in performing ionization cooling more efficient. Nevertheless, further simulations would be beyond the scope of this master thesis and therefore this work finally comes to its end. However, this chapter gave a lot of motivation to continue the task for investigating the field around ionization cooling advanced for a muon collider.

Chapter 8: Conclusions

8.1 Summary

A multi TeV muon collider opens the door to new physics discoveries, including unknown particle creation and a deeper understanding of the Higgs potential. At a cm. energy of 125 GeV, assuming a small energy spread of accelerated beams, a muon collider would be a possible option for a Higgs factory. This could be a demonstrator of the future TeV discovery machine and would test the novel accelerator technology especially designed for the muon collider.

This thesis specifically considers on simulation studies for the final cooling system, which is one of the key components required for reaching high luminosities in the collider by means of transverse emittance reduction. Multiple scattering tests of muons inside matter were performed with ICOOL. The scattering is an essential process in ionization cooling and had to be investigated before starting the studies on emittance reductions.

Using thin Be and Al windows (10-1000 μm) as absorber confinements, the rms scattering angels of these high-Z materials agree statistically with the theoretical prediction. Due to a small initial kinetic energy (10 MeV) of the muon beam, high angle deflections are more probable.

Low emittances and weak energies are realistic after-final cooling conditions, where the beam has to pass through a window at least. This thesis demonstrates, that Al brings more disadvantages than Be windows. The target emittance will be reheated, when the beam penetrates the Al window with a too high energy, or the beam stops completely inside the window at a too low energy. Windows made out of Be can be an option, but it is not clear how thin they can be technically produced. It is therefore worth to take mylar for future studies into account for the replacement of Al and Be windows.

To obtain the average scattering angles of liquid hydrogen absorbers, the interaction of muons with liquid deuterium as an absorber was implemented in the existing code of ICOOL. In both low-Z materials the resulting average angles differ slightly from to the analytical model. It was assumed that this difference is due to simulating with high

initial kinetic energies (∼100 MeV) and long absorber lengths (10-100 cm), which are baseline parameters of the final cooling system developed in the previous studies.

A rotating coordinate system was used for analysis of the beam parameters, as a solenoid couples the transverse particle coordinates. The beam and machine dependent coordinate transformation leads to a decoupling and makes it possible to evaluate the beam parameters in the transverse planes separately.

Ionization cooling is described by a specific non-analytical formula, which was solved numerically using the Runge-Kutta method. This made it possible to compare the predicted emittance with the simulations. The equilibriums emittance of previous studies strongly differs from calculations performed in this work. The beam parameter analyzes of the tracked muons in hard edge fields with different absorbers inside were performed using the rotating frame technique and an analyzes routine from ICOOL. By comparing the beam parameters evaluated from the these two codes with the theoretical prediction, it can be concluded, that this rotation method is sensitive to energy spread changes.

From the simulations it can be observed that lithium is a good candidate for cooling a beam with high energies and high emittances. However, liquid deuterium and liquid hydrogen are the only possible absorbers for reaching target emittance of 25 μm within a low beam energy range.

The fringe fields of real solenoids were previously calculated analytically for optimizing the initial parameter settings in the ICOOL simulation. Compared to previous studies, it was proven that it is possible to cool down a muon beam with a normalized transverse emittance of 55 μm by means of liquid hydrogen and a higher solenoid field (∼50 T). However, correlation effects are still present and other solenoidal models included in ICOOL and optimization techniques have to be used for providing an efficient final cooling scheme.

8.2 Outlook

The achievement of constant betatron functions or zero correlations in an absorber-solenoid system is the target goal in final cooling simulations performed in this thesis. Additionally, the non avoidable longitudinal emittance growth has to be studied and controlled in future final cooling investigations, together with the optimization of emittance increase, energy spread control and muon transmission rate.

Apart from high field solenoids and absorbers, the re-acceleration by means of a RF system has to be taken into account. The rising energy spread after passing through the absorber has to be controlled by means of phase focusing. During the acceleration the muons have to be kept focused transversely, otherwise losses occur. Hence, the RF

system must be surrounded by low field solenoids, imposing challenges on the cavity developments for the muon collider studies.

The next task is to match the fringe field of a muon beam in the field-flipped solenoid with an absorber inside. A more efficient emittance reduction by including a field-flipped solenoid has to be proven. The optimization routines of a high field solenoid, RF system and a field flipped solenoid unify the simulation of a whole final cooling cell. This makes it possible to study an entire final cooling lattice by simulating several final cooling cells in a row.

Besides investigating into computational calculations, engineering integration issues has to be taken into account as well, which are for example the absorber design, windows and hydrogen cryogenics inside a magnet system. Further, studying high field solenoid and its fabrications is a key technology for ionization coolings. Especially the feasibility studies of producing 50 T magnets and beyond is one of the main efforts of the muon collider collaboration.

Building a muon collider requires developments in research and technology, in order to extend our knowledge of universe's nature. Whether a muon collider will be built in future, its environmental friendly construction will for sure enter a new area of accelerator technology. The invention of novel technologies in the field of superconductors and radiation protection will be used for industrial and medical purposes.

Abbreviations

ATLAS A Toroidal LHC ApparatuS

BEH Brout-Englert-Higgs

BSM Beyond the Standard Model

CERN European Organization for Nuclear Research

CLIC Compact Linear Collider

cm. centre of mass

CMS Compact Muon Solenoid

GSW Glashow-Salam-Weinberg

HF high field

HTS high temperature superconductor

ILC International Linear Collider

IMCC internationl Muon Collider Collaboration

LEP Large Electron Positron Collider

LHC Large Hardron Collider

MAP U.S. Muon Accelerator Program

MICE international Muon Ionization Cooling Experiment

NC normal conducting

QCD Quantum Chromodynamic

QED Quantum Electrodynamic

PDG Particle Data Group

RCS Rapid Cycling Synchrotron

ReBCO rare-erth barium copper oxide

RF Radio frequency

RK4 four-stage Runge Kutta

RLA Recirculation Linear Accelerator

rms root mean square

SM Standard Model

SPS Super Proton Synchrotron

SRF super conducting radio frequency

Bibliography

[1] G. I. Budker, "An effective method of damping particle oscillations in proton and antiproton storage rings," *Soviet Atomic Energy*, vol. 22, pp. 438–440, May 1967.

[2] G. I. Budker, "Proceedings of the 7th internationalconference on high-energy accelerators," Academy of Sciences of Armenia, Yerevan,1970, 1969.

[3] N. Skrinsky and V. V. Parkhomchuk, "Sov. j. part. nucl.12, 223," 1981.

[4] K. Wille, *The physics of particle accelerators: an introduction.* Oxford: Oxford Univ. Press, 2000.

[5] M. Koch, E. P. Rubenstein, and S. Ebashi, *Handbook on synchrotron radiation.* Amsterdam: North-Holland, 1991.

[6] "Search for the standard model higgs boson at LEP," *Physics Letters B*, vol. 565, pp. 61–75, July 2003.

[7] T. A. Collaboration, "Observation of a new particle in the search for the standard model higgs boson with the ATLAS detector at the LHC," *Physics Letters B*, vol. 716, pp. 1–29, Sept. 2012.

[8] T. C. Collaboration, "Observation of a new boson at a mass of 125 GeV with the CMS experiment at the LHC," *Physics Letters B*, vol. 716, pp. 30–61, Sept. 2012.

[9] G. Aad, T. Abajyan, B. Abbott, J. Abdallah, S. Abdel Khalek, O. Abdinov, R. Aben, B. Abi, M. Abolins, O. AbouZeid, and et al., "Evidence for the spin-0 nature of the higgs boson using atlas data," *Physics Letters B*, vol. 726, p. 120–144, Oct 2013.

[10] T. L. collaboration, "Test of lepton universality in beauty-quark decays," tech. rep., CERN, Geneva, Mar 2021. All figures and tables, along with any supplementary material and additional information, are available at https://cern.ch/lhcbproject/Publications/p/LHCb-PAPER-2021-004.html (LHCb public pages).

[11] R. Dermisek, K. Hermanek, and N. McGinnis, "Highly enhanced contributions of heavy higgs bosons and new leptons to muon g-2 and prospects at future colliders," *Physical Review Letters*, vol. 126, May 2021.

[12] A. Einstein, "Zur elektrodynamik bewegter körper," *Annalen der Physik*, vol. 322, no. 10, pp. 891–921, 1905.

[13] W. Herr and B. Muratori, "Concept of luminosity," 2006.

[14] M. A. Palmer, "The us muon accelerator program," 2015.

[15] J.-P. Delahaye, C. Ankenbrandt, A. Bogacz, S. Brice, A. Bross, D. Denisov, E. Eichten, P. Huber, D. M. Kaplan, H. Kirk, R. Lipton, D. Neuffer, M. A. Palmer, R. Palmer, R. Ryne, and P. Snopok, "Enabling intensity and energy frontier science with a muon accelerator facility in the u.s.: A white paper submitted to the 2013 u.s. community summer study of the division of particles and fields of the american physical society," 2014.

[16] N. Mokhov, "Particle production for a muon storage ring i. targetry and mu+ muyield," *Nuclear Instruments and Methods in Physics Research Section A: Accelerators, Spectrometers, Detectors and Associated Equipment*, vol. 472, pp. 546–551, Oct. 2001.

[17] N. V. Mokhov, "Recent MARS15 Developments: Nuclide Inventory, DPA and Gas Production," *46th ICFA Advanced Beam Dynamics Workshop on High-Intensity and High-Brightness Hadron Beams*, 12 2010.

[18] K. T. McDonald, P. U., H. G. Kirk, H. Park, T. Tsang, /Brookhaven, I. Efthymiopoulos, A. Fabich, F. Haug, J. Lettry, M. Palm, H. Pereira, /CERN, N. Mokhov, and F. O. R. /Rutherford, "The merit high-power target experiment at the cern ps,"

[19] C. T. Rogers, D. Stratakis, G. Prior, S. Gilardoni, D. Neuffer, P. Snopok, A. Alekou, and J. Pasternak, "Muon front end for the neutrino factory," *Physical Review Special Topics - Accelerators and Beams*, vol. 16, Apr. 2013.

[20] H. K. Sayed, "High intensity muon beam source for neutrino beam experiments," *Nuclear Instruments and Methods in Physics Research Section A: Accelerators, Spectrometers, Detectors and Associated Equipment*, vol. 794, pp. 193–199, Sept. 2015.

[21] M. Palmer, "Muon collider and neutrino factory overview," *Beam Dynamics Newsletter*, vol. 55, 8 2011.

[22] R. B. Palmer, Fernow, and R. C, "Charge separation for muon collider cooling,"

[23] R. Palmer, V. Balbekov, J. S. Berg, S. Bracker, L. Cremaldi, R. C. Fernow, J. C. Gallardo, R. Godang, G. Hanson, A. Klier, and D. Summers, "Ionization cooling ring for muons," *Physical Review Special Topics - Accelerators and Beams*, vol. 8, June 2005.

[24] D. Stratakis and R. B. Palmer, "Rectilinear six-dimensional ionization cooling channel for a muon collider: A theoretical and numerical study," *Physical Review Special Topics - Accelerators and Beams*, vol. 18, Mar. 2015.

[25] Y. Derbenev and R. P. Johnson, "Six-dimensional muon beam cooling using a homogeneous absorber: Concepts, beam dynamics, cooling decrements, and equilibrium emittances in a helical dipole channel," *Physical Review Special Topics - Accelerators and Beams*, vol. 8, Apr. 2005.

[26] K. Yonehara, R. P. Johnson, and Y. S. Derbenev, "A helical cooling channel system for muon colliders," 2012.

[27] Y. Alexahin and /Fermilab, "Circularly inclined solenoid channel for 6d ionization cooling of muons,"

[28] Y. Bao, G. Hanson, R. B. Palmer, and D. Stratakis, "Conceptual design and modeling of a six-dimensional bunch merging scheme for a muon collider," *Physical Review Accelerators and Beams*, vol. 19, Mar. 2016.

[29] P. R. B and R. Fernow, "Six-dimensional bunch merging for muon collider cooling,"

[30] G. Flanagan, R. Abrams, C. Ankenbrandt, M. A. C. Cummings, R. P. Johnson, M. Popovic, and A. Moreti, "Using Project X as a Proton Driver for Muon Colliders and Neutrino Factories," *Conf. Proc. C*, vol. 100523, pp. 4452–4454, 2010.

[31] S. Bogacz, "Low energy stages - 'dogbone' muon RLA," *Nuclear Physics B - Proceedings Supplements*, vol. 149, pp. 309–312, Dec. 2005.

[32] D. Summers, L. Cremaldi, R. Godang, B. Kipapa, H. Rice, and R. Palmer, "Muon acceleration to 750 GeV in the tevatron tunnel for a 1.5 tev muon collider," in *2007 IEEE Particle Accelerator Conference (PAC)*, IEEE, June 2007.

[33] B. King, "Potential hazards from neutrino radiation at muon colliders," in *Proceedings of the 1999 Particle Accelerator Conference (Cat. No.99CH36366)*, IEEE.

[34] N. Mokhov and A. V. Ginneken, "Neutrino radiation at muon colliders and storage rings," *Journal of Nuclear Science and Technology*, vol. 37, pp. 172–179, Mar. 2000.

[35] D. Schulte, "Muon Collider Collaboration. 107th Plenary ECFA meeting - ZOOM," Nov 2020.

[36] D. Schulte, "The International Muon Collider Collaboration," in *Proc. IPAC'21*, no. 12 in International Particle Accelerator Conference, pp. 3792–3795, JACoW Publishing, Geneva, Switzerland, 08 2021. https://doi.org/10.18429/JACoW-IPAC2021-THPAB017.

[37] H. K. Sayed, R. B. Palmer, and D. Neuffer, "High field – low energy muon ionization cooling channel," *Physical Review Special Topics - Accelerators and Beams*, vol. 18, Sept. 2015.

[38] H. Euler and B. Kockel, "Ueber die streuung von licht an licht nach der diracschen theorie," *Die Naturwissenschaften*, vol. 23, pp. 246–247, Apr. 1935.

[39] W. K. Heisenberg and H. Euler, "Folgerungen aus der Diracschen Theorie des Positrons," *Z. Phys.*, vol. 98, pp. 714–732, 1936.

[40] L. D. Broglie, "Recherches sur la théorie des quanta," *Annales de Physique*, vol. 10, no. 3, pp. 22–128, 1925.

[41] "The quantum theory of the emission and absorption of radiation," *Proceedings of the Royal Society of London. Series A, Containing Papers of a Mathematical and Physical Character*, vol. 114, pp. 243–265, Mar. 1927.

[42] M. Gell-Mann, "A schematic model of baryons and mesons," *Physics Letters*, vol. 8, pp. 214–215, Feb. 1964.

[43] E. Fermi, "Versuch einer theorie der beta-strahlen. i," *Zeitschrift fuer Physik*, vol. 88, pp. 161–177, Mar. 1934.

[44] C. S. Wu, E. Ambler, R. W. Hayward, D. D. Hoppes, and R. P. Hudson, "Experimental test of parity conservation in beta decay," *Physical Review*, vol. 105, pp. 1413–1415, Feb. 1957.

[45] T. D. Lee and C. N. Yang, "Question of parity conservation in weak interactions," *Physical Review*, vol. 104, pp. 254–258, Oct. 1956.

[46] C. Rubbia, "Experimental observation of the intermediate vector w+, w-, z0," *Reviews of Modern Physics*, vol. 57, pp. 699–722, July 1985.

[47] M. B. et. al. *Physics Letters B*, vol. 122, pp. 476–485, Mar. 1983.

[48] D. Möhl, G. Petrucci, L. Thorndahl, and S. van der Meer, "Physics and technique of stochastic cooling," *Physics Reports*, vol. 58, pp. 73–102, Feb. 1980.

[49] S. L. Glashow, "The renormalizability of vector meson interactions," *Nuclear Physics*, vol. 10, pp. 107–117, Feb. 1959.

[50] A. Salam and J. C. Ward, "Weak and electromagnetic interactions," *Il Nuovo Cimento*, vol. 11, pp. 568–577, Feb. 1959.

[51] S. Weinberg, "A model of leptons," *Physical Review Letters*, vol. 19, pp. 1264–1266, Nov. 1967.

[52] P. W. Higgs, "Broken symmetries and the masses of gauge bosons," *Physical Review Letters*, vol. 13, pp. 508–509, Oct. 1964.

[53] F. Englert and R. Brout, "Broken symmetry and the mass of gauge vector mesons," *Physical Review Letters*, vol. 13, pp. 321–323, Aug. 1964.

[54] "Mark Thomson presents the book "Modern Particle Physics". Mark Thomson presents the book "Modern Particle Physics"," Oct 2013.

[55] H. YUKAWA, "On the interaction of elementary particles. i," *Proceedings of the Physico-Mathematical Society of Japan. 3rd Series*, vol. 17, pp. 48–57, 1935.

[56] Y. Fukuda, "Evidence for oscillation of atmospheric neutrinos," *Physical Review Letters*, vol. 81, pp. 1562–1567, Aug. 1998.

[57] D. d'Enterria, "Higgs physics at the future circular collider," 2017.

[58] A. DJOUADI, "The anatomy of electroweak symmetry breaking tome II: The higgs bosons in the minimal supersymmetric model," *Physics Reports*, vol. 459, pp. 1–241, Apr. 2008.

[59] FCC-Colaboration, "FCC physics opportunities," *The European Physical Journal C*, vol. 79, June 2019.

[60] A. Papaefstathiou and K. Sakurai, "Triple higgs boson production at a 100 TeV proton-proton collider," *Journal of High Energy Physics*, vol. 2016, Feb. 2016.

[61] M. Chiesa, F. Maltoni, L. Mantani, B. Mele, F. Piccinini, and X. Zhao, "Measuring the quartic higgs self-coupling at a multi-TeV muon collider," *Journal of High Energy Physics*, vol. 2020, Sept. 2020.

[62] A. Djouadi, A. Falkowski, Y. Mambrini, and J. Quevillon, "Direct detection of higgs–portal dark matter at the LHC," *The European Physical Journal C*, vol. 73, June 2013.

[63] P. data groupe, "Review of particle physics," *Progress of Theoretical and Experimental Physics*, vol. 2020, Aug. 2020.

[64] A. Robson and P. Roloff, "Updated clic luminosity staging baseline and higgs coupling prospects," 2018.

[65] P. Roloff, U. Schnoor, R. Simoniello, and B. Xu, "Double higgs boson production and higgs self-coupling extraction at CLIC," *The European Physical Journal C*, vol. 80, Nov. 2020.

[66] V. BARGER and T. HAN, "DOUBLE HIGGS BOSON PRODUCTION VIA WW FUSION IN TeV e+e- COLLISIONS," *Modern Physics Letters A*, vol. 05, pp. 667–674, Apr. 1990.

[67] W. Kilian, S. Sun, Q.-S. Yan, X. Zhao, and Z. Zhao, "Multi-higgs boson production and unitarity in vector-boson fusion at future hadron colliders," *Physical Review D*, vol. 101, Apr. 2020.

[68] M. Palmer, "Technology: from 125 GeV to multi-TeV Muon Collider." https://snowmass21.org/energy/muon_forum, 2021. [Online; accessed 20-September-2021].

[69] F. Hinterberger, *Physik der Teilchenbeschleuniger und Ionenoptik*. Berlin Heidelberg: Springer-Verlag, 2 ed., 2008.

[70] B. Holzer, "Transverse Beam Dynamics," *CERN Yellow Rep. School Proc.*, vol. 5, p. 1. 30 p, 2018.

[71] W. Demtröder, *Experimentalphysik 2*. Springer Berlin Heidelberg, 2013.

[72] G. W. Hill, "On the part of the motion of the lunar perigee which is a function of the mean motions of the sun and moon," *Acta Mathematica*, vol. 8, no. 0, pp. 1–36, 1886.

[73] E. Courant and H. Snyder, "Theory of the alternating-gradient synchrotron," *Annals of Physics*, vol. 3, pp. 1–48, Jan. 1958.

[74] K. Floettmann, "Some basic features of the beam emittance," *Physical Review Special Topics - Accelerators and Beams*, vol. 6, Mar. 2003.

[75] P. J. Channell, "Laser cooling of heavy-ion beams," *Journal of Applied Physics*, vol. 52, pp. 3791–3793, June 1981.

[76] S. P. Moller, "Cooling techniques," *Conf. Proc. C*, vol. 9209071, pp. 601–617, 1992.

[77] D. Möhl, G. Petrucci, L. Thorndahl, and S. van der Meer, "Physics and technique of stochastic cooling," *Physics Reports*, vol. 58, pp. 73–102, Feb. 1980.

[78] D. Moehl, "Phase space cooling in storage rings," *Physica Scripta*, vol. T22, pp. 21–27, jan 1988.

[79] "Status of muon collider research and development and future plans," *Physical Review Special Topics - Accelerators and Beams*, vol. 2, Aug. 1999.

[80] D. V. Neuffer, "Muon Cooling and Applications," Oct 1993.

[81] "XXII. the penetration of atomic particles through matter," in *Niels Bohr Collected Works*, pp. 423–568, Elsevier, 1987.

[82] N. Bohr, "II. on the theory of the decrease of velocity of moving electrified particles on passing through matter," *The London, Edinburgh, and Dublin Philosophical Magazine and Journal of Science*, vol. 25, pp. 10–31, Jan. 1913.

[83] W. Demtroeder, *Experimentalphysik 1: Mechanik und Waerme; 6th ed.* Springer-Lehrbuch, Berlin: Springer Spektrum, 2013.

[84] D. E. Groom and S. R. Klein, "Passage of particles through matter," *The European Physical Journal C*, vol. 15, pp. 163–173, Mar. 2000.

[85] M. Tanabashi, "Review of particle physics," *Physical Review D*, vol. 98, Aug. 2018.

[86] P. Gruber, "Material Constants for Muon Cooling Simulations," Tech. Rep. CERN-OPEN-2000-314. CERN-NEUTRINO-FACTORY-NOTE-23. CERN-NUFACT-NOTE-23, CERN, Geneva, Oct 2000.

[87] P. D. G., "https://pdg.lbl.gov/2020/AtomicNuclearProperties/,"

[88] F. Bloch, "Zur bremsung rasch bewegter teilchen beim durchgang durch materie," *Annalen der Physik*, vol. 408, no. 3, pp. 285–320, 1933.

[89] H. Bethe, "Zur theorie des durchgangs schneller korpuskularstrahlen durch materie," *Annalen der Physik*, vol. 397, no. 3, pp. 325–400, 1930.

[90] P. Sigmund, *Particle Penetration and Radiation Effects*. Springer Berlin Heidelberg, 2006.

[91] M. Mühlbauer, H. Daniel, F. Hartmann, P. Hauser, F. Kottmann, C. Petitjean, W. Schott, D. Taqqu, and P. Wojciechowski *Hyperfine Interactions*, vol. 119, no. 1/4, pp. 305–310, 1999.

[92] R. C. Fernow and J. C. Gallardo, "Validity of the differential equations for ionization cooling," in *AIP Conference Proceedings*, AIP, 1996.

[93] R. C. Fernow and J. C. Gallardo, "Muon transverse ionization cooling: Stochastic approach," *Physical Review E*, vol. 52, pp. 1039–1042, July 1995.

[94] H. A. Bethe, "Molieres theory of multiple scattering," *Physical Review*, vol. 89, pp. 1256–1266, Mar. 1953.

[95] B. Rossi and K. Greisen, "Cosmic-ray theory," *Rev. Mod. Phys.*, vol. 13, pp. 240–309, Oct 1941.

[96] G. R. Lynch and O. I. Dahl, "Approximations to multiple coulomb scattering," *Nuclear Instruments and Methods in Physics Research Section B: Beam Interactions with Materials and Atoms*, vol. 58, pp. 6–10, May 1991.

[97] M. J. Berger, M. Inokuti, H. H. Andersen, H. Bichsel, D. Powers, S. . M. Seltzer, D. . Thwaites, and D. E. Watt, "6. energy-loss straggling," *Journal of the International Commission on Radiation Units and Measurements*, vol. os25, pp. 61–68, May 1993.

[98] U. Fano, "Penetration of protons, alpha particles, and mesons," *Annual Review of Nuclear Science*, vol. 13, no. 1, pp. 1–66, 1963.

[99] Geant4-Collaboration, "Geant4—a simulation toolkit," *Nuclear Instruments and Methods in Physics Research Section A: Accelerators, Spectrometers, Detectors and Associated Equipment*, vol. 506, pp. 250–303, July 2003.

[100] R. Fernow, "ICOOL: a simulation code for ionization cooling of muon beams," in *Proceedings of the 1999 Particle Accelerator Conference (Cat. No.99CH36366)*, IEEE.

[101] R. C. Fernow, "Icool reference manual," 8 2012.

[102] V. Bayliss, J. Boehm, T. Bradshaw, M. Courthold, S. Harrison, M. Hills, P. Hodgson, S. Ishimoto, A. Kurup, W. Lau, K. Long, A. Nichols, D. Summers, M. Tucker, P. Warburton, S. Watson, and C. Whyte, "The liquid-hydrogen absorber for MICE," *Journal of Instrumentation*, vol. 13, pp. T09008–T09008, Sept. 2018.

[103] M. A. Green, E. L. Black, M. A. Cummings, D. M. Kaplan, S. Ishimoto, J. H. Cobb, W. Lau, S. Yang, and R. B. Palmer, "The intergration of liquid and solid muon absorbers into afocusing magnet of a muon cooling channel,"

[104] J. C. N. Hartman, D. Li, "Thin beryllium windows - analysis and design status,"

[105] CEA, "The Spaladin hydrogen target." http://irfu.cea.fr/dacm/en/Phocea/Vie_des_labos/Ast/ast_visu.php?id_ast=2425, 2008. [Online; accessed 18-August-2021].

[106] D. Neuffer, "Introduction to muon cooling," *Nuclear Instruments and Methods in Physics Research Section A: Accelerators, Spectrometers, Detectors and Associated Equipment*, vol. 532, pp. 26–31, Oct. 2004.

[107] W. Kutta, "Beitrag zur näherungsweisen Integration totaler Differentialgleichungen," *Zeit. Math. Phys.*, vol. 46, pp. 435–53, 1901.

[108] C. Runge, "über die numerische auflösung von differentialgleichungen," *Math. Ann.*, vol. 46, p. 167–178, 1895.

[109] A. Grüneis, "Lecture to numerical methodes, university of technolgy vienna," May 2018.

[110] K. Heun, "Neue methoden zur approximativen integration der differentialgleichungen einer unabhügigen verüderlichen," *Z. Math. Phys. I*, vol. 45, p. 23–38, 1900.

[111] W. D. Markiewicz, D. C. Larbalestier, H. W. Weijers, A. J. Voran, K. W. Pickard, W. R. Sheppard, J. Jaroszynski, A. Xu, R. P. Walsh, J. Lu, A. V. Gavrilin, and P. D. Noyes, "Design of a superconducting 32 t magnet with REBCO high field coils," *IEEE Transactions on Applied Superconductivity*, vol. 22, pp. 4300704–4300704, June 2012.

[112] S. Hahn, K. Kim, K. Kim, X. Hu, T. Painter, I. Dixon, S. Kim, K. R. Bhattarai, S. Noguchi, J. Jaroszynski, and D. C. Larbalestier, "45.5-tesla direct-current magnetic field generated with a high-temperature superconducting magnet," *Nature*, vol. 570, pp. 496–499, June 2019.

[113] Brucker, "Bruker's novel UHF NMR magnet technology." https://www.bruker.com/en/products-and-solutions/mr/nmr/ascend-ghz-class.html, 2021. [Online; accessed 17-September-2021].

[114] P. Virtanen, R. Gommers, T. E. Oliphant, M. Haberland, T. Reddy, D. Cournapeau, E. Burovski, P. Peterson, W. Weckesser, J. Bright, S. J. van der Walt, M. Brett, J. Wilson, K. J. Millman, N. Mayorov, A. R. J. Nelson, E. Jones, R. Kern, E. Larson, C. J. Carey, İ. Polat, Y. Feng, E. W. Moore, J. VanderPlas, D. Laxalde, J. Perktold, R. Cimrman, I. Henriksen, E. A. Quintero, C. R. Harris, A. M. Archibald, A. H. Ribeiro, F. Pedregosa, P. van Mulbregt, and SciPy 1.0 Contributors, "SciPy 1.0: Fundamental Algorithms for Scientific Computing in Python," *Nature Methods*, vol. 17, pp. 261–272, 2020.